

HU ISSN 1785-6892 in print
HU ISSN 2064-7522 online

DESIGN OF MACHINES AND STRUCTURES

A Publication of the University of Miskolc

Volume 13, Number 1 (2023)



Miskolc University Press
2023

EDITORIAL BOARD

- Á. DÖBRÖCZÖNI
Editor in Chief
Institute of Machine and Product Design
University of Miskolc
H-3515 Miskolc-Egyetemváros, Hungary
machda@uni-miskolc.hu
- Á. TAKÁCS
Assistant Editor
Institute of Machine and Product Design
University of Miskolc
H-3515 Miskolc-Egyetemváros, Hungary
takacs.agnes@uni-miskolc.hu
- R. CERMAK
Department of Machine Design
University of West Bohemia
Univerzitní 8, 30614 Plzen Czech Republic
rcermak@kks.zcu.cz
- B. M. SHCHOKIN
Consultant at Magna International Toronto
borys.shchokin@sympatico.ca
- W. EICHLSEDER
Institut für Allgemeinen Maschinenbau
Montanuniversität Leoben,
Franz-Josef Str. 18, 8700 Leoben, Österreich
wilfrid.eichlseder@notes.unileoben.ac.at
- S. VAJNA
Institut für Maschinenkonstruktion,
Otto-von-Guericke-Universität Magdeburg,
Universität Platz 2, 39106 MAGDEBURG, Deutschland
vajna@mb.uni-magdeburg.de
- P. HORÁK
Department of Machine and Product Design
Budapest University of Technology and Economics
H-1111 Budapest, Műegyetem rkp. 9.
MG. ép. I. em. 5.
horak.peter@gt3.bme.hu
- K. JÁRMAI
Institute of Materials Handling and Logistics
University of Miskolc
H-3515 Miskolc-Egyetemváros, Hungary
altjar@uni-miskolc.hu
- L. KAMONDI
Institute of Machine and Product Design
University of Miskolc
H-3515 Miskolc-Egyetemváros, Hungary
machkl@uni-miskolc.hu
- GY. PATKÓ
Department of Machine Tools
University of Miskolc
H-3515 Miskolc-Egyetemváros, Hungary
patko@uni-miskolc.hu
- J. PÉTER
Institute of Machine and Product Design
University of Miskolc
H-3515 Miskolc-Egyetemváros, Hungary
machpj@uni-miskolc.hu

CONTENTS

<i>Aghakhani, Alireza–Takács, Ágnes:</i> The meaning of concept in design methodology	5
<i>Aljawabrah, Ayham–Lovas, László:</i> Study the effect of the tooth chamfer angle on the dog clutch shiftability	12
<i>Dakhel, Ahmad Yasser–Lukács, János:</i> Full-scale tests of transporting pipeline sections – a review and consequences to our investigations	28
<i>Dömötör, Csaba:</i> Vehicle emblems from nature.....	52
<i>Ficzere, Péter:</i> The role of artificial intelligence in the development of railway transportation.....	67
<i>Meknassi, Raid Fekreddine–Béres, Gábor–Lukács, Zsolt:</i> Prediction of strain distribution during the plane strain tensile test based on artificial neural networks	74
<i>Olukayode, Olakunle–Adedeji, Wasiu–Oyewole, Kehinde–Idris, Musibaudeen:</i> Design and development of a table mounted manual seed cracking machine for a hard seed (Deocla Reflexa Hook F).....	84
<i>Pintér, Ádám Sándor–Sarka, Ferenc:</i> Investigation of the involute spur gears with different pressure angles.....	103
<i>Sarka, Ferenc:</i> Modelling possibilities of bolt connections with finite element method	112
<i>Sesztakov, Viktor:</i> Possibility of use of artificial intelligence in the whole claim settlement process on insurance companies' vehicle claims	124
<i>Várkuli, Miklós–Bognár, Gabriella–Szente, József:</i> Determination of tooth surface points on bevel gears for checking on a coordinate measuring machine.....	131

THE MEANING OF CONCEPT IN DESIGN METHODOLOGY

ALIREZA AGHAKHANI¹ – ÁGNES TAKÁCS²

*University of Miskolc, Institute of Machine and Product Design
H-3515, Miskolc-Egyetemváros*

*¹alirezaaghakhani90@gmail.com, ²takacs.agnes@uni-miskolc.hu
¹<https://orcid.org/0009-0003-5280-9485>, ²<https://orcid.org/0000-0002-3210-6964>*

Abstract: On the field of design methodology concept and conceptual design do not sound unfamiliar. However, if we try to deepen into the topic, we may encounter polemics in some cases, one of which even the word concept itself. The aim of the paper is to present a kind of order in connection with designing a concept.

Keywords: *design methodology, design process, conceptual design, concept, mock-up*

1. INTRODUCTION

We can come across the word concept not only in the field of design methodology, but also in everyday life. Even within this field of science, the word concept and conceptual design are not clear. Authors do not always mean the same thing by conceptual design, which in many cases leads to polemics. The typical reason for this is the different languages researchers use. For an example Hungarian literature is based on German-language publications, the vocabulary of which is not easy to adopt. (Feldhusen & Grote, 2013) (Ulrich & Eppinger, 2012) The purpose of the publication is to reveal what can be called a concept and to point out the nuances of the word concept by systematizing the properties of these concepts.

When the designer begins to design a new equipment, considering the methodological recommendations, he or she usually finds functions from which he or she generates solution variants. These principal solutions are the concepts. During their evaluation, one, or in some cases a few, are selected and further developments are made on them.

Major car manufacturers present their concept cars at car shows (e.g., the famous Geneva Motor Show). In many cases, these vehicles are working models, which are made so that the manufacturers can see the reactions of visitors and critics of the exhibition in relation to one of their innovations. It is like a poll. If the response

is good, the manufacturers will continue to deal with the given concept. But is that really all what the concept means?

2. THE PROCESS OF THE DESIGN

The steps of the design process based on VDI 2221 are shown in Figure 1 (VDI, 1986). It can be seen in the flowchart that during the design process, every single step affects all the steps before and after it. There is continuous iteration, while the plan is constantly moving forward in the direction of product documentation.

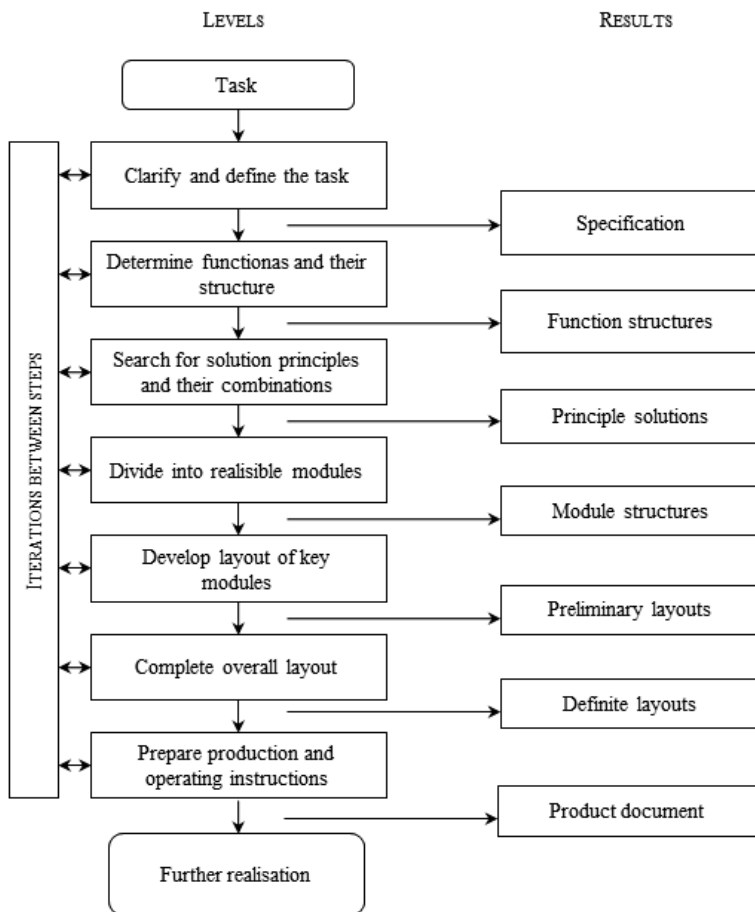


Figure 1 The process of the design (VDI, 1986)

According to the classic design methodology, conceptual design is the early phase of the entire design process, when the functions and form of the product are outlined after assessing the previous experiences, results, and user needs. Looking at the work phases in Figure 1, this lasts until step 4 ‘Divide into realisable modules’, the result of which are ‘Module structures’.

This can be called a principle solution or a study plan. However, the concept or study cars of the Geneva Motor Show mean more than that, they are obviously at a higher level of design. The concept according to classical design methodology only exists on paper, it has no real spatial extent, it is not tangible, even if the designer makes a sketch of it. On the contrary, a concept car is already a life-size model, some parts of which may even be functional units. Such models are theoretical models. During the evaluation of these theoretical models (e.g. critics' comments, or specific measurements, wind tunnel tests, etc.), mistakes and weak points are revealed, so they can be improved and developed. The result of this development is a working model. Every part of it fulfils its task, even though it is not perfect. If the errors of the working model can be corrected, a prototype is made, which is already an almost perfect model, and is also called a concept. Table 1 clearly summarizes the difference between the various concept levels.

Table 1
Concepts in the different phases of the design – comparison

	principle solution	theoretical model	working model	prototype
model	no tangible	tangible	tangible	tangible
operation	principle	theoretical and real	real	real
pieces	one/a few	one	more	more/one
embodiment design	no	partly	totally	totally
size	-	not always 1:1	not always 1:1	usually 1:1

After all, the concept types summarized in Table 1 are built on each other: there is no prototype without a principal solution. Examining the design phases of technical creations, examples can be found of each of the concept types presented.

3. CONCEPT LEVELS

Designing a vehicle is a very long process. It often takes years to fully design a type, and during these years it is essential that engineers create different models in each phase of the design. So as to be able to show examples of the various levels of concepts described above in relation to a specific product, let's take the car body as an example.

Due to the complex nature of the car as a system, the path that the engineers take together consists of countless phases, each of which measurements, calculations, and simulations should be done. In order to carry out these tasks, different models should be defined.

4.1. Principle solution – hand drawn sketch as an example

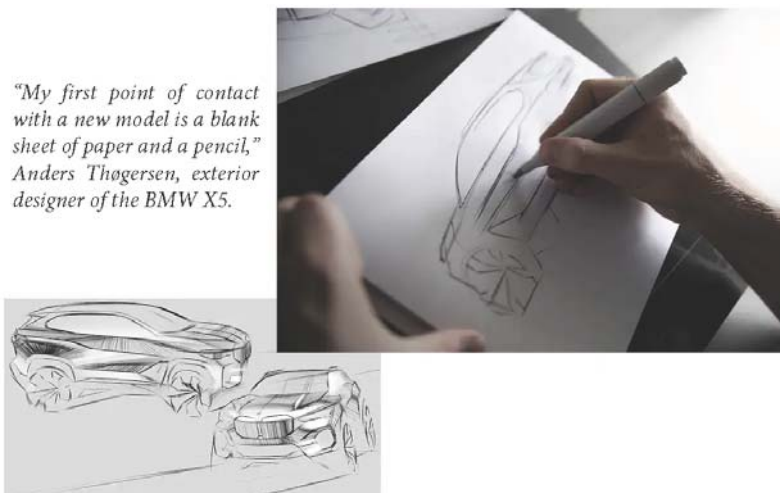


Figure 2 Hand drawn sketch from the shape [F2]

Freehand drawing is very important in any field of design. Technological development is continuous, thanks to which more and more advanced versions of digitizing tools are available for professionals, so freehand drawing is also changing, but its importance cannot be neglected, even if it is done on a digital board.

4.2. Theoretical model/Mock-up – clay model as an example

Study models or mock-ups serve the purpose of carrying out various tests and measurements on them. Figure 3 shows the creation of a car body clay model. It is apparently a detailed work, but with its help designers can collect a lot of important information about the 1:1 scale model of the dreamed form. The importance of the procedure developed by GM chief engineer Harley Earl is so much unquestionable as it is still used today. For example, on a 1:1 sized clay model of a car body we can make aerodynamical experiments in a wind tunnel. From this point of view, we are now talking about the clay model as a mock-up.



Figure 3 Creating a car body clay model [F3]



Figure 4 Renault Morphose [F4]

4.3. Working model – Concept Car

Working models allow designers to examine certain parts of the design in action. In terms of cars, concept cars are of great importance. These are the models that are exhibited at various car showrooms, and those that can be taken for a test drive

by interested possible customers, or which the main character of a movie races with on a cinema screen. These are the models with which car manufacturers can test the reactions of potential users or on which they can test certain experimental technologies. Figure 4 shows the Renault Morphose concept car. With the help of the QR code that can be seen in the figure a video introducing the concept can be watched. Figure 5 shows the Toyota Concept-i series concept.



Figure 5 Toyota Concept-i series [F5]

4.4. Prototype – Car crash cars

In some cases, prototypes are only almost fully functional versions, however, in many cases, e.g. in the case shown in Figure 6, functional, finished models are examined. The crash test shown in the figure serves precisely the purpose of allowing manufacturers to see how they comply the safety regulations of various agencies. For such tests, a preliminary series of 4-6 pieces is produced.



Figure 6 Side impact test [F6]

4. SUMMARY

Above it was presented at what levels the concept can be realized during the design process. It was introduced how different the concepts are in the meaning of how deep they are carried out through the examples of the automotive vehicle industry. It can be stated that a designer needs models and concepts in each step of the design process.

REFERENCES

Feldhusen, J. & Grote, K.-H., 2013. *Pahl/Beitz Konstruktionslehre*. 8. ed. Berlin: Springer.

Ulrich, K. T. & Eppinger, S. D., 2012. *Product Design and Development*. 5. ed. New York: McGraw-Hill.

VDI, 1986. *VDI 2221: Methodik zum Entwickeln und Konstruieren technischer Produkte*. Berlin: VDI.

SOURCE OF FIGURES

[F2] <https://www.bmw.com/en/design/car-design-in-7-steps.html> (last open: 29. April 2023)

[F3] <https://axleaddict.com/auto-industry/Sculptural-car-design> (last open: 29. April 2023)

[F4] <https://www.renault.co.uk/concept-cars/morphoz-concept.html> (last open: 29. April 2023)

[F5] <https://mag.toyota.co.uk/toyota-defines-the-future-of-mobility-with-concept-i-series/> (last open: 29. April 2023)

[F6] <https://www.carscoops.com/2022/08/only-one-mid-size-car-got-a-good-score-in-new-iihs-t-bone-test-simulating-crash-with-suv/> (last open: 29. April 2023)

STUDY THE EFFECT OF THE TOOTH CHAMFER ANGLE ON THE DOG CLUTCH SHIFTABILITY

AYHAM ALJAWABRAH¹, LÁSZLÓ LOVAS²

*Budapest University of Technology and Economics,
Department of Railway Vehicles and Vehicle System Analysis
1111. Műegyetem rkp. 3, Budapest*

¹aaljawabrah@edu.bme.hu, ²lovas.laszlo@kjk.bme.hu

¹<https://orcid.org/0000-0002-7537-6358>, ²<https://orcid.org/0000-0001-6710-9084>

Abstract: This paper studies the shiftability of the face dog clutch with chamfered teeth. The effect of the chamfer angle on the shiftability map and the probability are studied. In contrast to previous studies, a generalized mathematical model is developed based on the shiftability condition. The analysis considered two sets of cases: the overlap distance cases, and the chamfer side cases. The overlap distance cases locate the successful engagement position. The chamfer side cases investigate the effect of the system geometry and consider two cases. The results show that the chamfer angle has a negative effect on the dog clutch shiftability. Some geometric parameters show a different effect on the engagement probability for the rectangular tooth and chamfered tooth cases, and this behaviour is also analysed.

Keywords: *dog clutch, shiftability condition, shiftability map, engagement probability, chamfer angle*

1. INTRODUCTION

All vehicle systems receive great attention to improve its performance (Alzyod & Ficzer, 2021), (Alsardia, Lovas, & Ficzer, 2021), (Nguyen, Moghaddam, Pirouzfard, Fayyazbakhsh, & Su, 2021) and the vehicle gearbox is one of these systems. Conventional vehicle gearboxes utilize the synchronizer as a gearshift element to guarantee successful gearshift (Lovas, Play, Márialigeti, & Rigal, 2006). However, dog teeth clutch has been replacing the synchromesh because it has quicker shifting time, simpler structure, larger power transmitting capacity, and lower cost (Shiotsu, et al., 2019). The dog clutch is being applied in automated manual transmissions (Bóka, Márialigeti, Lovas, & Trencsényi, 2009), automatic

transmissions (Duan, 2014), and clutchless automated manual transmissions (Walker, Fang, & Zhang, 2017).

As dog teeth clutch is only a clutch and not a synchronizer, the problems of synchronization and shiftability have to be resolved. Boka et al. (Bóka, Márialigeti, Lovas, & Trencsényi, 2010) used the notion of engagement probability to find a certain successful region depending on the initial mismatch speed of the clutch halves. However, they focused on the low mismatch speed zone in their research and did not investigate the large mismatch speeds.

In a previous paper (Aljawabrah & Lovas, 2023), we have studied the dog teeth clutch shiftability from a kinematic point of view and determined the shiftability condition that identifies the successful engagement regions. We showed the parameters affecting the shiftability and determined the shiftability map based on an analytical method. In another previous paper (Aljawabrah & Lovas, 2022) we developed a method to calculate the shifting probability and studied the engagement probability's sensitivity to the system parameters. We showed that the number of teeth, and the amount of the tangential backlash affect positively the engagement probability, while the initial mismatch speed and the overlap distance, being the required tooth overlap for successful engagement, have a negative effect. All the aforementioned studies considered the dog tooth to be rectangular, not chamfered. The effect of the chamfer angle for the tooth edge on the dog teeth clutch shiftability is rarely discussed in the literature.

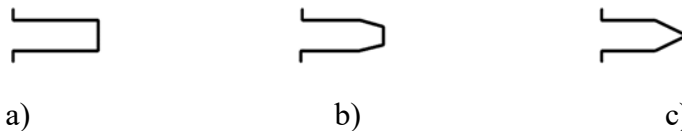


Figure 1 Tooth geometry for a) rectangular (no chamfer) tooth, b) partially chamfered tooth, and c) fully chamfered tooth

Among these rare cases, (Duan, 2014) developed a mathematical dynamic model for the dog teeth clutch used in an automatic transmission, and the model considered chamfered tooth. Eriksson (Mehari, Eriksson, & Kuttikal, 2013) performed a multibody dynamic parametric study for the dog clutch used in a truck gearbox transfer case. He studied three different tooth designs to study the effect of the chamfer distance, chamfer angles, and tooth side edge's angle. and the number of teeth. He developed eight sets of parameter combinations for simulation. Andersson (Andersson & Goetz, 2010) performed dynamic FEA using Abaqus on the dog clutch to investigate the effect of the chamfer angle, chamfer distance, and tooth angle. The aim was to find the maximum relative rotational speed that the system can handle to have a successful gearshift for each geometry and to

determine the best geometry among eleven alternatives. The author claimed that engagement is easier if the chamfer angle is smaller. Moreover, a fully chamfered tooth, Figure 1 c, is more effective than a partially chamfered tooth, Figure 1 b, for the same chamfer angle. These studies have considered the effect of the tooth chamfer angle using either dynamic modelling, multibody or FEA. These approaches require complicated models and are slow to compute. Moreover, the number of studied cases is limited.

This work aims to develop a method to investigate the effect of the tooth chamfer angle on the dog clutch shiftability. A generalized shiftability condition is developed based on (Aljawabrah & Lovas, 2023), where the chamfered tooth geometry is added to the previously developed model. A mathematical model taking into account the effect of the chamfer to the shiftability condition is presented. The shiftability map is created for different chamfer angle values, based on the method described in (Aljawabrah & Lovas, 2022), and different cases for the overlap distance and the chamfer angle parameters are examined. Finally, the effect of geometric parameters on the engagement probability for chamfered and rectangular tooth cases is compared.

2. METHODOLOGY

In a previous paper (Aljawabrah & Lovas, 2023), we have presented the dog clutch geometry, and the main geometric and kinematic parameters. Further on, we introduced a kinematical shiftability condition that guarantees side impact-free gearshift. Here, the considered tooth geometry had no chamfers.

The dog teeth clutch geometry is presented in detailed in Figure 2. The dog clutch (Figure 2 a) is a coupling used to transmit power. It consists of two parts having complementary geometry. These complementary shapes are referred to as dog teeth.

The parameters of the clutch geometry are presented in Table 1. The tooth dog geometry is discussed along two directions. Figure 2 b shows a linear (tangential) representation and Figure 2 c shows a radial representation. At the beginning of the shifting, an axial gap x_0 exists between the sliding sleeve and the shifted gear, and there is an initial relative angular position ξ between the marked teeth. Here the sliding dog can slide axially with a speed v_0 , while it has relative angular rotation with respect to the target gear. The relative angular rotation is called the mismatch speed $\Delta\omega_0$. The engagement of the complementary geometries is eased with an angular backlash.

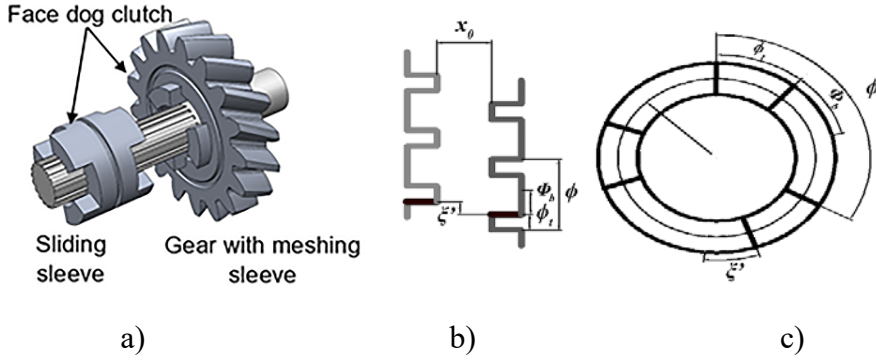


Figure 2 Face dog clutch: a) 3D model, and geometry as b) linear, and c) radial representation (Aljawabrah & Lovas, *Kinematical Model of the Dog Clutch Shifting*, 2023)

The axial dog clutch has an angular pitch ϕ given by (1), and an angular backlash given according to (2), where ϕ_t is the tooth thickness angle.

$$\phi = \frac{2\pi}{z} \quad (1)$$

$$\Phi_b = \phi - 2\phi_t \quad (2)$$

Table 1
Dog clutch shiftability parameters

Parameter	Range	Fixed Value	Parameter	Range	Fixed Value
Initial relative position ξ_0 [°]	$0-\phi$	0	Axial gap x_0 [mm]	1-6	7
Mismatch speed $\Delta\omega_0$ [rad] ([min-1])	0-500 (0 4775)	20 (190)	Overlap distance x_{fed} [mm]	0.5-3	0.5
Axial Speed v_0 [mm/s]	0-500	250	Number of teeth Z [-]	2-10	10
Mean radius r [mm]	5-60	40	Angular backlash Φ_b [°]	2-30	25

In (Aljawabrah & Lovas, 2023) we have studied the dog clutch shiftability for rectangular tooth dog clutch. We suppose that a successful engagement happens when an overlap x_{fed} is reached in the axial direction, where the a tooth on the sliding sleeve overlap a tooth on the gear with a distance x_{fed} , and based on this, we developed the shiftability condition shown in (3). This condition combines all

kinematic and geometric parameters and determines if there is a possibility of successful shifting for a given set of parameters. This condition was the base to develop the shiftability map and calculate the shifting probability as described in (Aljawabrah & Lovas, 2022).

$$0 \leq \text{mod} \left(\xi_0 + \Delta\omega_0 \frac{x_0}{v_0}, \frac{2\pi}{z} \right) \leq \Phi_b - \Delta\omega_0 \frac{x_{fed}}{v_0} \quad (3)$$

The shiftability condition was developed for teeth with no chamfer. The application for chamfered teeth requires the modification of some parameters. Figure 3a shows the geometry for the tooth chamfer with a chamfer angle (β). The chamfer length (x_{ch}) can be connected to the tooth thickness by (4). Solving (2) for ϕ_t and substituting into (4), (5) can be obtained.

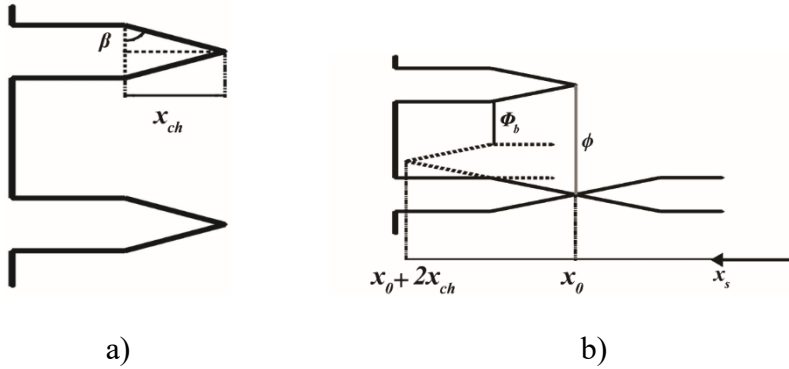


Figure 3 a) Geometry of chamfered dog tooth, b) Backlash variation

$$x_{ch} = \frac{\phi_t r}{2} \tan(\beta) \quad (4)$$

$$x_{ch} = \frac{\left(\frac{2\pi}{z} - \Phi_b\right) r}{4} \tan(\beta) \quad (5)$$

In the case of a not chamfered tooth, the angular backlash (Φ_b) is constant as the sliding dog moves axially. The introduction of the chamfer causes the backlash to decrease while the sliding dog moves axially towards the gear wheel (Figure 3 b). A generalized equation can be formulated for the backlash in function of the axial position. According to Figure 3 b, the backlash equals ϕ at $x = x_0$ and equals Φ_b at $x = x_0 + 2x_{ch}$. So, a linear relationship can be derived as shown in (6). Substituting (1) and (5) into (6), (7) can be formed.

$$\Phi_b(x) = \phi - \frac{x - x_0}{2x_{ch}}(\phi - \Phi_b) \quad x_0 \leq x \leq x_0 + 2x_{ch} \quad (6)$$

$$\Phi_b(x) = \frac{2\pi}{z} - 2 \frac{x - x_0}{r \tan(\beta)} \quad (7)$$

In what follows, we consider chamfer angle values only within the interval $[0^\circ; 45^\circ]$. The analysis of the effect of the chamfer angles considers two distinct sets of cases: the chamfer sides cases, and the successful connection position (required overlap distance).

Firstly, let us consider the chamfer sides cases set. Here, two cases are considered: firstly, just one tooth with side chamfer and the another without, and both teeth having chamfer (Figure 4). The successful engagement position is considered at full overlap distance for both cases, as illustrated in (8). The backlash at full overlap distance is Φ_b .

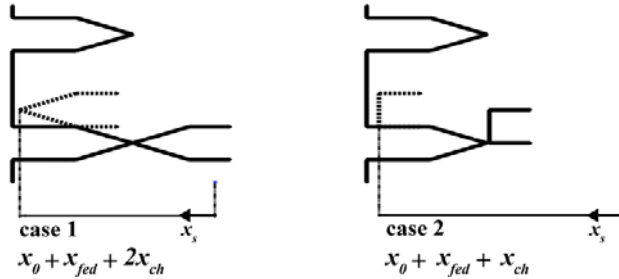


Figure 4 Chamfer side cases

$$x_{fed}' = \begin{cases} x_{fed} + 2x_{ch} & \text{case 1} \\ x_{fed} + x_{ch} & \text{case 2} \end{cases} \quad (8)$$

Secondly, let us consider the successful connection position cases. Figure 5 shows the successive steps to reach the successful connection position. In the case of not chamfered (rectangle) tooth case, the overlap distance has a clear definition, as it depends on the wear of the tooth vertices, and it can be identified experimentally. A successful gearshift process is guaranteed if the sliding sleeve can pass the overlap distance without teeth face impact, and this distance is what we refer to as the 'successful connection position'. Knowing the successful connection position and other system parameters, successful gearshift process can be distinguished based on (3). However, in case of chamfered tooth geometry, the face impact can happen at different places, and it is unknown at which location the face impact will no

longer affect the gearshift process. In other words, it is not clearly defined at which connection position the sliding sleeve will not bounce back and engage with the gear sleeve even though a face impact occurs after this position. To understand the system, three successful connection position cases are considered, where these cases aim to identify possible successful connection positions. These positions are directly connected to the chamfer angle, so they can assist to study the effect of the chamfer angle both on the shiftability map and the engagement probability.

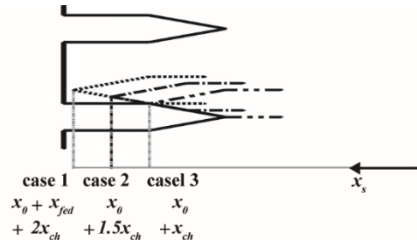


Figure 5 Successful connection position cases

The three cases for the overlap distance, shown in (9), are the following: full overlap distance (case 1), the overlap distance is 1.5 times the chamfer length (case 2), and the overlap distance equals the chamfer length (case 3). As the backlash changes with the axial position, the backlash values at the successful engagement position are used as illustrated in (10). This equation shows that an expression for the backlash can be derived without depending on the chamfer angle. This is expected, since from the backlash equation derivation (6) we see that the equation is based on the chamfer length (x_{ch}), and the overlap distance (x_{fed}') is also described in terms of chamfer length (x_{ch}). Substituting all in (6), the x_{ch} terms can be eliminated.

$$x_{fed}' = \begin{cases} x_{fed} + 2x_{ch} & \text{case 1} \\ 1.5x_{ch} & \text{case 2} \\ x_{ch} & \text{case 3} \end{cases} \quad (9)$$

$$\Phi_b' = \begin{cases} \Phi_b & \text{case 1} \\ \frac{2\pi}{z} - \frac{1.5}{2} \left(\frac{2\pi}{z} - \Phi_b \right) & \text{case 2} \\ \frac{2\pi}{z} - \frac{1}{2} \left(\frac{2\pi}{z} - \Phi_b \right) & \text{case 3} \end{cases} \quad (10)$$

From (8), (9), (10) it is clear that the modified parameters are the overlap distance for the two case sets, as well as the backlash for the second case set, but the backlash does not depend on the chamfer angle. So, in the following discussion, the focus will be on the overlap distance (x_{fed}').

3. RESULTS

The chamfer angle has a great effect on the overlap distance. Figure 6 shows x_{fed}' response to the chamfer angle. For chamfer sides' cases, Figure 6 a shows higher overlap distance for two sides chamfer case compared to one side chamfer. According to (5), x_{ch} increases with higher β , which in term increases the required tooth overlap distance, as (8) shows. Also, considering Figure 6 b, case 1 (full x_{fed}) has higher sensitivity to β , compared with case 2 (x_{fed}' is $1.5x_{ch}$) and case 3 (x_{fed}' is x_{ch}) which agrees with (9). Below 15° chamfer angle, case 2 and case 3 have lower x_{fed}' compared to no chamfer case.

It has been shown that the chamfer angle affects the overlap distance, which in term will affect the shiftability map and the engagement probability. So, it is worth to briefly explaining how this distance affects the dog clutch shiftability.

Figure 8 shows the so-called shiftability map where the blue zone expresses the successful gearshift region where (3) is evaluated at each point in a given domain, knowing all the parameters appearing in this equation. In (Aljawabrah & Lovas, 2022) we showed that higher overlap distance narrows the successful engagement area, and this behaviour is clear in Figure 7 a, where the successful region portion from a given domain decays rapidly with x_{fed} .

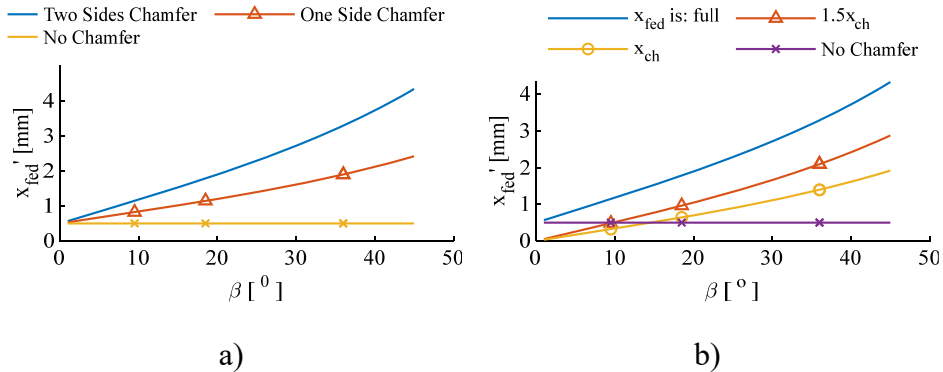


Figure 6 Chamfer angle effect on the overlap distance for a) chamfer sides cases, and b) for overlap distance cases

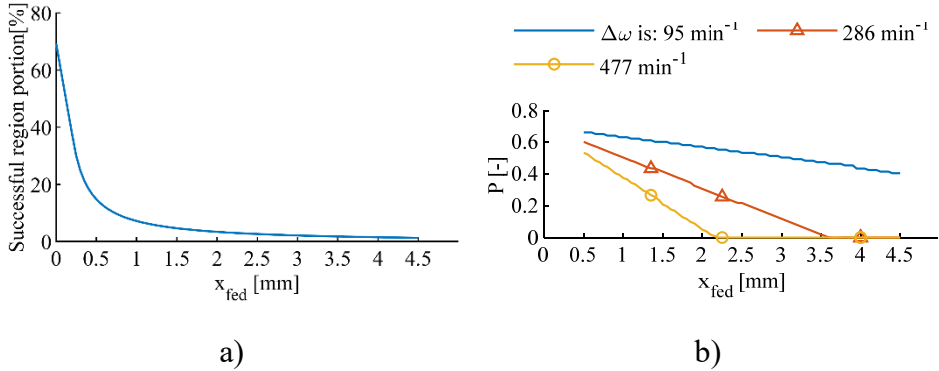


Figure 7 Overlap distance effect on a) successful engagement area, and b) engagement probability

On the other hand, in many cases, the initial relative position cannot be measured. So, the initial relative position is considered to be a random variable in the interval $[0, \phi]$, or one tooth pitch period, and in contrast to the shiftability condition in (3), the successful gearshift process is described by engagement probability. Figure 7 b shows the probability sensitivity to x_{fed} change. Here the probability decreases with a higher overlap distance, and theoretically, there is no possible connection above a certain value, as the required time to cover x_{fed} becomes larger than the available time before the gear's and sliding sleeve's teeth impact.

3. 1. Chamfer sides' cases

Let us consider the cases when chamfers exist or not on the mating teeth (Figure 4). In Figure 8, the horizontal axis shows ξ and $\Delta\omega_0$ is on the vertical axis. The maps represent chamfer existence cases 1, and 2 for different chamfer angle β . The third column of the subfigures in Figure 8 shows the no chamfer case for reference. Here, with the increase of β , the zone of successful shifting (blue zones) decreases. Referring to Figure 6 a, x_{fed}' increases with higher chamfer angle values, which increases the required overlap distance x_{fed}' .

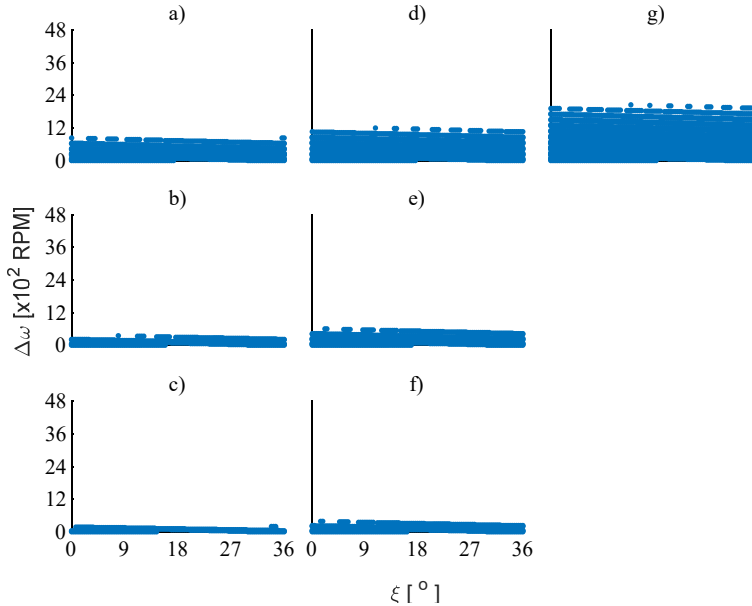


Figure 8 The shiftability map for ξ_0 and $\Delta\omega$ at different chamfer side cases: one side chamfer case for β of a) 10° b) 30° c) 45° and two sides chamfer case for β of d) 10° e) 30° f) 45° , and e) no chamfer case

When comparing case 1 to case 2, it can be seen that the latter has larger successful engagement regions at a fixed chamfer angle, since case 2 has a shorter overlap distance (Figure 8). Moreover, the difference in the shiftability map between case 1 and case 2 decreases at higher β . Figure 6 a shows that x_{fed}' increases rapidly with increasing β . Note also, that with increasing x_{fed}' , the system approaches the no shiftability point, as the size of the blue zone decreases on the shiftability map, Figure 7 a.

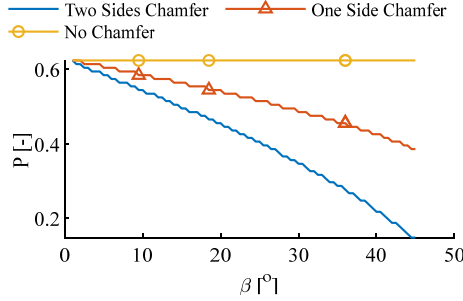


Figure 9 Engagement probability for chamfer side cases, ξ_0 is random in the interval $[0, \phi]$

Figure 9 shows that the engagement probability decreases for both two and one chamfer cases as the overlap distance increases. Note also, that the probability has higher sensitivity at higher β . Figure 6 a shows the x_{fed} ' is more sensitive β at higher values which gives higher probability sensitivity at higher chamfer angles.

3. 2. Successful connection position cases

Figure 10 shows shiftability maps. The horizontal axis shows ξ_0 and $\Delta\omega_0$ is on the vertical axis. The maps represent x_{fed} ' cases 1, 2, and 3 for different chamfer angles β . Case 3 has the largest successful engagement region at fixed β ; case 3 has the shortest overlap distance compared with case 2 and case 1 as Figure 10 shows. It can also be seen that the successful engagement regions (blue zones) decrease with higher chamfer angles.

The shiftability maps are more sensitive to the change in the chamfer angle (β) in case 3 and have less effect on case 2 shiftability maps, but the lowest effect on case 1. Figure 6 b shows that case 3 has shorter x_{fed} ' compared to the other two cases and as Figure 7 a shows that the successful region portion is more sensitive to the change in x_{fed} at lower values. The phenomenon is similar to that seen in Figure 8, since mainly the chamfer angle affects the overlap distance in both cases set.

Figure 11 illustrates the engagement probability for the overlap distance cases, when the mismatch speed increases. The probability decreases with the β as expected. Case 1 has the lowest probability since it has the highest x_{fed} '. Case 3 probability curves' decrease is the quickest, then comes case 2, then the case 1. This means that having a chamfer limits the possibility of successful shifting at higher mismatch speed domain. This is justified with Figure 11: x_{fed} ' increases with β increase, which causes the shifting probability to decrease. Moreover, the

probability curve trends are similar to those in Figure 9 since the chamfer angle mainly affects the overlap distance.

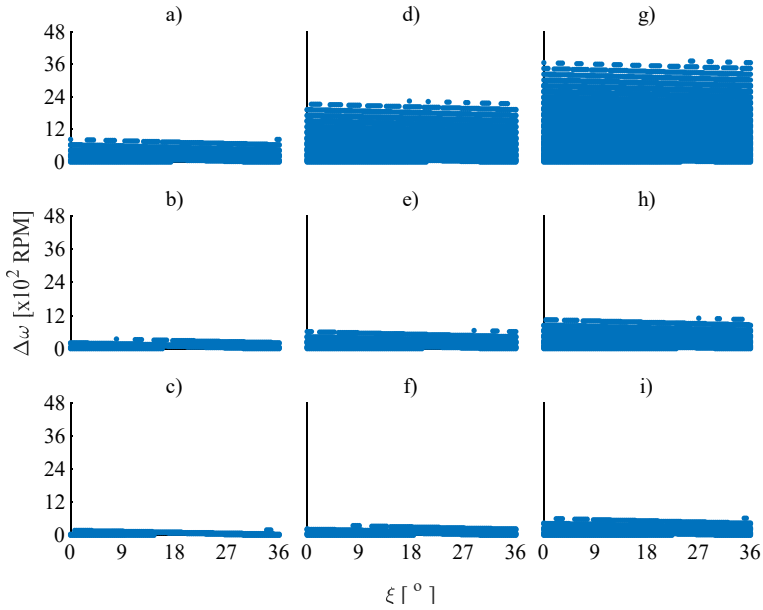


Figure 10 The shiftability map for ζ_0 and $\Delta\omega$ at different overlap distance cases: Full x_{fed} ' (case 1) for β of a) 10° b) 30° c) 45° , x_{fed} ' is $1.5x_{ch}$ (case 2) for β of d) 20° e) 30° f) 45° , x_{fed} ' is x_{ch} (case 3) for β of g) 20° h) 30° i) 45°

Figure 11 a also shows that case 3 always has a higher probability compared to no chamfer case at given low mismatch speed. However, this advantage vanishes with the mismatch speed increase. Thus, the developed model allows to check whether it is worth to have a chamfer at given tooth geometry and mismatch speed conditions.

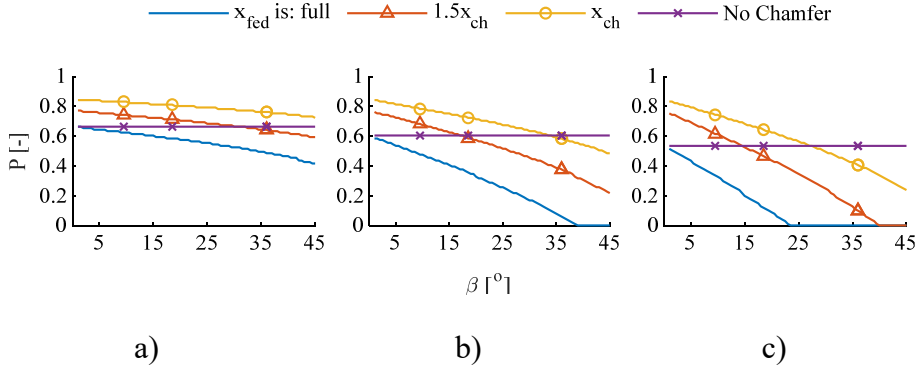


Figure 11 Probability plot for overlap distance cases when $\Delta\omega_0$ is a) 95 min^{-1} b) 286 min^{-1} and c) 477 min^{-1} , ζ_0 is random in the interval $[0, \phi]$

3. 3. System Parameters effect

(5) describing the chamfer length contains geometric parameters: the mean tooth radius r , the number of teeth z , and the angular backlash Φ_b . In what follows, the effect of these parameters on the engagement probability in the case of a rectangular and chamfered tooth are compared.

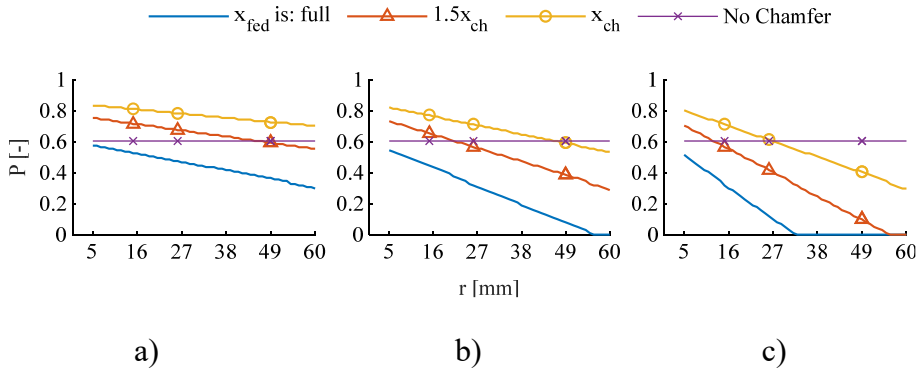


Figure 12 Probability sensitivity to the men radius change for β of a) 15° b) 30° and c) 45° , ζ_0 is free in the interval $[0, \phi]$

a) b) c)
Figure 12 shows that the radius has no effect on the connection probability in case there is no chamfer, but has a negative linear effect if the dog teeth are chamfered even at fixed β . According to (5), the chamfer length increases with the mean radius, as well as the tooth thickness. Comparison of Figure 12 a, b, and c, show

that the slope of the curves is increasing, which means probability sensitivity for the mean radius increases as the β increases.

Figure 13 illustrates the effect of the number of teeth z on the connection probability. The trends of the curves in Figure 13 a, b, and c show that teeth number has a direct linear relationship with probability.

On the other hand, increasing β increases the minimum required number of teeth to have a possible gearshift.

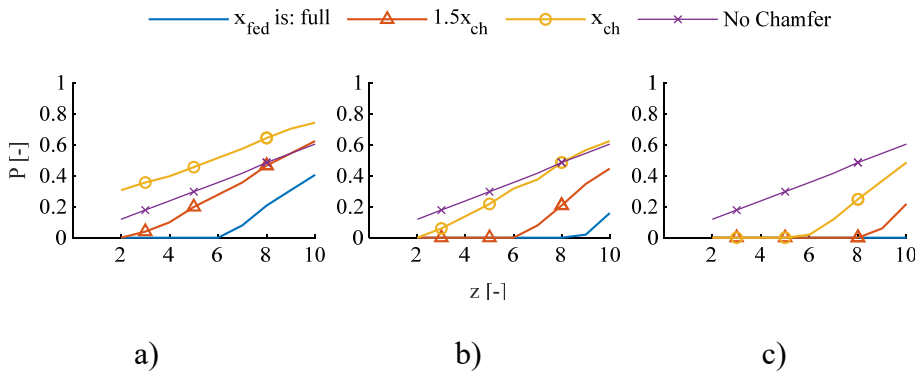


Figure 13 Probability sensitivity to the number of teeth change for β of a) 15° b) 30° and c) 45°

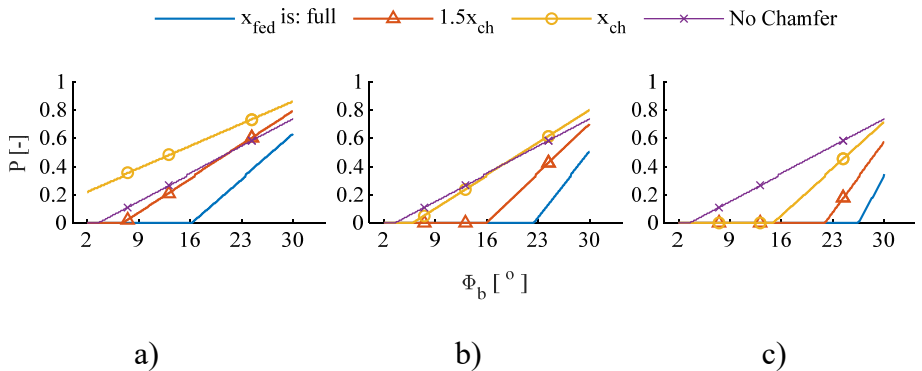


Figure 14 Probability sensitivity to backlash change for β of a) 15° b) 30° and c) 45°

Figure 14a) b) c)
Figure 14 illustrates the change in the connection probability depending on the angular backlash. The probability curve trends are similar to those in Figure 13, and similar conclusions can be drawn. On the other hand, the tooth thickness has

a major effect on the chamfer length as shown in (4): the chamfer length increases with the tooth thickness. So, reducing the tooth thickness within the angular pitch has a positive effect on the engagement probability by reducing the chamfer length from one side, and allowing for higher backlash from another side.

4. Summary

In this paper, the effect of the chamfer angle on the shiftability map and the engagement probability was investigated. The analysis is based on the kinematical shiftability condition. The inclusion of the chamfer angle modified the expression of the overlap distance and the backlash in the condition. The analysis considered two sets of cases: the overlap distance cases, and the chamfer side cases. The overlap distance cases try to locate the successful engagement position since the location is not clear compared to the rectangular tooth case while the chamfer side distance investigates the effect of the system geometry. Regarding the considered cases, the results showed a globally negative effect for the chamfer angle presence on the engagement probability, at fixed other parameters.

In case of low mismatch speeds, there may be some advantage in the application of chamfered teeth, but this zone is limited. At higher mismatch speeds, higher actuator axial speed must be present to overcome the overlap distance increase due to the chamfers.

REFERENCES

- Aljawabrah, A., & Lovas, L. (2022). Shiftability Study of a Dog Clutch., *VII. Gépészeti Szakmakultúra Konferencia*. Budapest. Retrieved from https://gteportal.eu/content/uploads/2022/09/1A_2_Lovas-Aljawabrah_Study_CIKK.pdf
- Aljawabrah, A., & Lovas, L. (2023). Kinematical Model of the Dog Clutch Shifting. *GÉP*, 74(1), 9-12.
- Alsardia, T., Lovas, L., & Ficzer, P. (2021). Prototype for fit investigations. *Design of Machines and Structures*, 11(1), 5-15. doi:<https://doi.org/10.32972/dms.2021.001>
- Alzyod, H., & Ficzer, P. (2021). Potential applications of additive manufacturing technologies in the vehicle industry. *Design of Machines and Structures*, 11(2), 5-13. doi:<http://doi.org/10.32972/dms.2021.009>

Andersson, M., & Goetz, K. (2010). FE analysis of a dog clutch for trucks with all-wheel-drive. *Master thesis*. Växjö, Sweden: Linnaeus University.

Bóka, G., Márialigeti, J., Lovas, L., & Trencsényi, B. (2009). External synchronization strategies for automated mechanical transmissions with face dog clutch and countershaft brake. *Scientific Bulletin Series C: Fascicle Mechanics, Tribology, Machine Manufacturing Technology*, 224(9), 75-80. doi:<https://doi.org/10.1243/09544070JAUTO1435>

Bóka, G., Márialigeti, J., Lovas, L., & Trencsényi, B. (2010). Face dog clutch engagement at low mismatch speed. *Periodica Polytechnica Transportation Engineering*, 38(1), 29-35. doi:<https://doi.org/10.3311/pp.tr.2010-1.06>

Duan, C. (2014). Analytical study of a dog clutch in automatic transmission application. *SAE International Journal of Passenger Cars-Mechanical Systems*, 7(3), 1155-1162. doi:<https://doi.org/10.4271/2014-01-1775>

Lovas, L., Play, D., Márialigeti, J., & Rigal, J.-F. (2006). Modeling of gear changing behaviour. *Periodica Polytechnica Transportation Engineering*, 34(1-2), 35-58.

Mehari, A., Eriksson, F., & Kuttikal, J. L. (2013). Parametric study of a dog clutch used in a transfer case for trucks. *Master thesis*. Växjö, Sweden: Linnaeus University.

Nguyen, D. D., Moghaddam, H., Pirouzfard, V., Fayyazbakhsh, A., & Su, C.-H. (2021). Improving the gasoline properties by blending butanol-Al₂O₃ to optimize the engine performance and reduce air pollution. *Energy*, 218. doi:<https://doi.org/10.1016/j.energy.2020.119442>

Shiotsu, I., Tani, H., Kimura, M., Nozawa, Y., Honda, A., Tabuchi, M., . . . Kanzaki, K. (2019). Development of High Efficiency Dog Clutch with One-Way Mechanism for Stepped Automatic Transmissions. *International Journal of Automotive Engineering*, 10(2), 156-161.

Walker, P. D., Fang, Y., & Zhang, N. (2017). Dynamics and control of clutchless automated manual transmissions for electric vehicles. *Journal of Vibration and Acoustics*, 139(6), 061005 (13 pages). doi:<https://doi.org/10.1115/1.4036928>

FULL-SCALE TESTS OF TRANSPORTING PIPELINE SECTIONS – A REVIEW AND CONSEQUENCES TO OUR INVESTIGATIONS

AHMAD YASSER DAKHEL¹ – JÁNOS LUKÁCS²

University of Miskolc, Institute of Materials Science and Technology,

3515, Miskolc-Egyetemváros

¹yaser.dakhel@gmail.com, ²janos.lukacs@uni-miskolc.hu

Abstract: Hydrocarbon transport pipelines' safe operation is an economic and environmental interest. These pipelines are typically designed for static loads, but during their long-time operation - due to pressure changes and environmental impacts - they are also subject to cyclical loads. The individual pipe sections are connected by girth welds, which represent potential sources of hazards in terms of damage. In order to assess the reliability of girth welds, full-scale tests are carried out under simple and complex loads. The purpose of this article is twofold. On the one hand, summarize the full-scale tests on transmission pipelines, with special attention to the tests on girth welds; on the other hand, based on this, draw conclusions for the design and implementation of our own full-scale tests.

Keywords: *transporting pipeline, full-scale test, girth weld, complex loading condition*

1. INTRODUCTION

A lot of efforts have been made to estimate the mechanical performance of pipes subjected to longitudinal plastic stresses as a result of the progress of strain-based design (SBD) for pipelines. Ductile ripping from a girth weld flaw is a common failure condition that defines tensile strain capacity (TSC). Because of factors like welding bevel angles and high-low misalignment (MA), this condition is difficult to predict. Table 1 shows the characteristics of incidents on transporting pipeline girth welds investigated by the Institute of Materials Science and Technology at the University of Miskolc.

The fundamental failure mechanics, which involve localized plastic deformation and material shredding, is equally challenging to model. Stationary crack modelling and the damage mechanics technique are two typical finite element analysis (FEA) techniques. Both strategies have disadvantages. It has been noted that stationary crack modelling can underestimate TSC because it is unable to account for all of the plasticity that happens in the area of a tearing fracture and does not

explicitly simulate tearing (Fairchild, Crapps, Cheng, Tang, & Shafrova, 2016), (Fairchild, Shafrova, Tang, Crapps, & Cheng, 2014). When it comes to the damage mechanics technique for modelling the tearing process, there is a lot of discussion on how to tune/calibrate the micro-mechanical parameters that the model relies on.

Table 1
Main data of selected catastrophic girth weld damages on gas transporting pipelines

ID	DN, mm	PN, bar	Material ID (API 5L) (API, 2018)	Operation years	Cause(s) of the failure
No1	400	63	Grade B and X52	54	crack in a repaired girth weld
No2	600	60	X52 and X60	45	crack in a repaired girth weld caused by the repair and the cyclic loads
No3	800	64	X65	33	crack initiated in the meeting point of a girth weld and the spiral weld, caused by geometrical irregularities and cyclic loads

The question is, what should an engineer do when the failure scenario is complex, and modelling approaches are limited? There are often two solutions to this puzzle, one of which is significantly more critical. The first step is to execute many modelling runs and sensitivity analyses covering all of the variable ranges in depth. This entails hundreds of modelling runs for models with a half-dozen variables (as is the case for TSC prediction). While such exercises can help with recognizing patterns (for example, as MA grows, TSC decreases), they are insufficient to build a credible model on their own (Li, Gong, Lacidogna, Deng, & Wang, 2021). The second and far more critical solution is that model results must be compared to full-scale experiments (FSTs). In applied mechanics, this has always been the authoritative answer and the answer for TSC prediction. In addition, both theoretical and practical approaches to structural integrity require the investigations of both structural elements and complete structures (FSTs) (Lukács, Nagy, Harmati, Koritárné, & Kuzsella, 2012), (Koncsik, A szerkezetintegritás helye és szerepe az oktatásban és a kutatásban, 2019), (Koncsik, Szerkezetintegritási kutatások az Innovatív Anyagtechnológiák Tudományos Műhelyben, 2021).

The purpose of this article is twofold. On the one hand, we summarize the full-scale tests on transmission pipelines, with particular attention to the tests on girth

welds; on the other hand, based on this, we draw conclusions for the design and implementation of our own full-scale tests.

2. THE RELEVANCE OF THE FULL-SCALE TESTING

2. 1. Short overview of full-scale pipeline testing

Full-scale pipe strain tests involve stretching and bending a section of pipe to failure. The fundamental metric is strain capacity, which refers to how much longitudinal strain the specimen can withstand before failing, which is commonly referred to as maximum load. It is possible that the specimen is a parent pipe or that it has one or even more girth welds. Artificial flaws (from a practical point of view notches) are common in girth welds; thus, including different degrees of welding joint MA might be beneficial. When there are girth weld faults, the failure scenario frequently involves ductile ripping from the defect till the remaining ligament fails. To reflect service conditions, the specimens might be compressed (Zhang & Maddox, 2014).

A schematic of a characteristic FST pipeline section with girth welds is shown in Figure 1 (Fairchild, Crapps, Cheng, Tang, & Shafrova, 2016), (Fairchild, Shafrova, Tang, Crapps, & Cheng, 2014). The cost of specimen design and manufacture, followed by testing and analysis, may go into the tens of thousands of USDs (millions of HUF) for each test. A single test might take weeks or months to complete. The preparation of a specimen with known and high qualities is the most significant component of test specimen design and production.

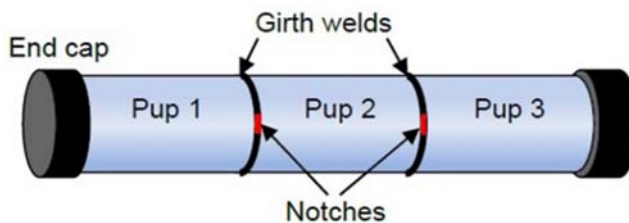


Figure 1 Schematic structure of a full-scale pipeline section (specimen) (Fairchild, Crapps, Cheng, Tang, & Shafrova, 2016), (Fairchild, Shafrova, Tang, Crapps, & Cheng, 2014)

The true qualities of the specimen cannot be determined since it was damaged during testing. To create data indicative of the specimen, small-scale experiments on additional material are required, and the results of these tests are crucial inputs for TSC model predictions. The design in Figure 1 is created by the layout in

Figure 2 (Fairchild, Crapps, Cheng, Tang, & Shafrova, 2016), (Fairchild, Shafrova, Tang, Crapps, & Cheng, 2014).

Full-scale testing also necessitates the use of specimen instrumentation. Longitudinal strain and notch opening are monitored using instrumentation. Linear variable displacement transducers (LVDTs) are commonly employed to monitor strain, while clip gages are utilized to measure crack mouth opening displacement (CMOD). Figure 3 (Fairchild, Crapps, Cheng, Tang, & Shafrova, 2016), (Fairchild, Shafrova, Tang, Crapps, & Cheng, 2014) is an example of an effective instrumentation layout. A possible unrolling of the pipe specimen is depicted in the diagram. To detect global strain over the specimen length, three massive LVDTs are employed. The anchor points are as practicable as near the end cap confluence with the pipe specimen. The FST's strain capacity is defined as the average of these LVDTs at maximum load (Yang, et al., 2022). Additionally, shorter LVDTs are placed on each pup, and these LVDTs are used to detect possible non-uniform straining. The application of scribe lines (ultimately scribed mesh) is the least technical (but most beneficial) of all strain monitoring methods (Figure 3 (Fairchild, Crapps, Cheng, Tang, & Shafrova, 2016), (Fairchild, Shafrova, Tang, Crapps, & Cheng, 2014)).

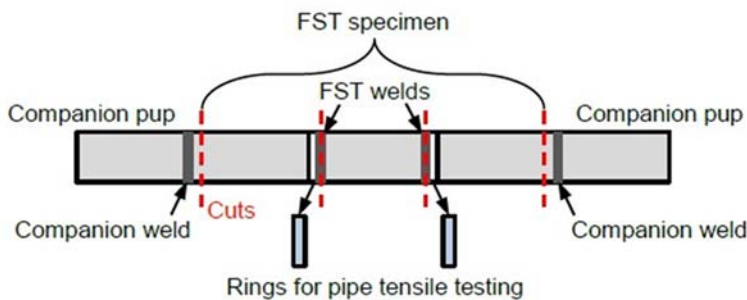


Figure 2 Preparation strategy for FST sections and associated materials (Fairchild, Crapps, Cheng, Tang, & Shafrova, 2016), (Fairchild, Shafrova, Tang, Crapps, & Cheng, 2014)

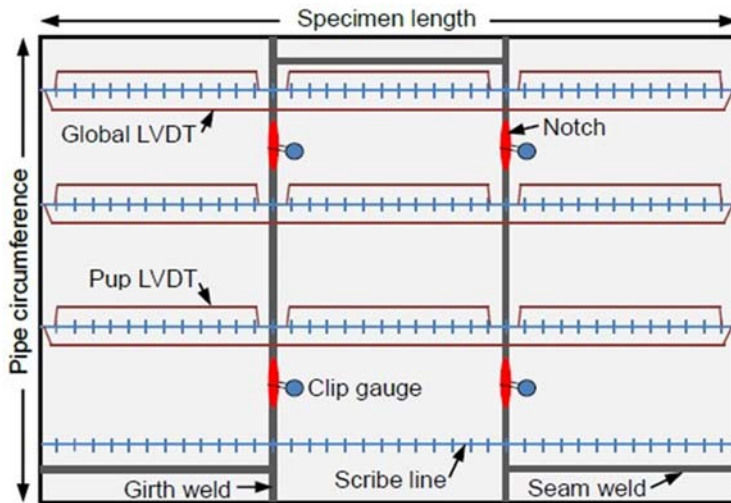


Figure 3 Instrumentation for FST (unrolled pipe view)
 (Fairchild, Crapps, Cheng, Tang, & Shafrova, 2016), (Fairchild, Shafrova,
 Tang, Crapps, & Cheng, 2014)

The structure shown in Figures 1-3 can, of course, be differed from, and in some cases should be. In the case where the FST tests are performed on replaced pipe sections, there is only one tested girth weld on the pipe section, and no notches are applied. The purpose of the tests is to analyse the damage that has occurred and to draw conclusions about the remaining lifetime (Lukács, Koncsik, & Chován, 2022).

Regular (100-150 mm) crosshairs on scribe lines can be placed along the same linear routes as the LVDTs. To quantify strain, the distance between the marks and the thickness of the wall at the markings are measured before and after the test. Data from scribe lines may be utilized to double-check LVDTs and track non-uniform strains. The process of assessing the data post-test to gain a complete picture of specimen performance is just as vital as test preparation. This necessitates a cross-validation of LVDT and scribe line data. Non-uniform straining should be looked for during the activity. If this is suspected, further ultrasonic wall thickness measurements may be beneficial. The CMOD data should be compared to the results of the other notch assessment methods (fractography, sectioning). One of the main objectives is to see if any notches were "active" throughout the test, indicating that ductile tearing has started. The CMOD data is typically easy if the specimen does not fracture. If the specimen cracks, the first step is to pinpoint the location of the fracture, which is usually the notch with the highest

CMOD at the conclusion of the test. It should be highlighted that brittle fractures have been recorded farther from the notch with the biggest CMOD (see Figure 4 (Igi, Muraoka, & Masamura, 2013)).

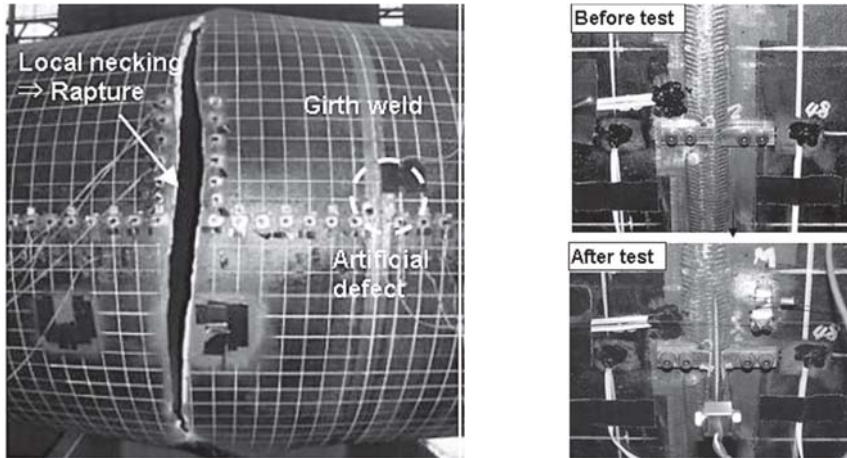


Figure 4 Fracture appearance of a girth weld after FST on meshed pipeline (Igi, Muraoka, & Masamura, 2013)

Fractured specimens might be difficult to interpret; fractography is a valuable tool for gaining a better understanding of the failure event and, in many cases, assessing the importance of the FST. Fractography is used to detect the location of quick fracture initiation, whether crack propagation was ductile, brittle, or mixed, and the crack propagation direction. The texture, geometry, and varied shades of grey revealed on the fracture surface frequently allow the failure event to be recreated.

2. 2. The importance of high-quality full-scale testing data

Full-scale testing is a large-scale representation of experimental fracture mechanics. FST specimen preparation is more complex than, for instance, Charpy impact or crack tip opening displacement (CTOD) tests due to several variables. However, the toughness and crack propagation resistance curves of the material were related to the geometry of the specimen; the fracture toughness decreases with the increase of the constraint level of the specimen (Yang, et al., 2022), (Thaulow, Østby, Nyhus, Zhang, & Skallerud, 2004) (see Figure 5 (Yang, et al., 2022)).

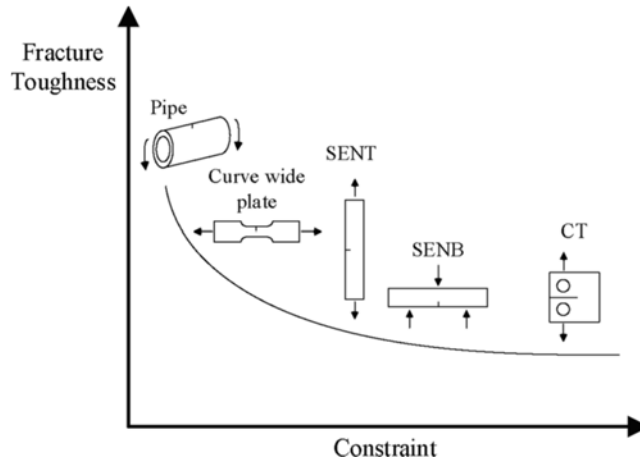


Figure 5 Schematic diagram of specimen geometry effect on fracture toughness (Yang, et al., 2022)

During the preparation of the full-scale pipeline test, the amount of material is substantial, and specimen manufacturing necessitates extensive welding. As a result, the likelihood of material property variation and the occurrence of unintentional flaws is enhanced. Furthermore, notch insertion in the heat-affected zone (HAZ), which must be done "blind" into the specimen surface, is extremely challenging (Igi, Muraoka, & Masamura, 2013), (Elyasi, et al., 2021), (Wei, Jin, Pei, & Wang, 2021), (Xuan, et al., 2016).

One overarching concept and two hypothetical examples may be used to demonstrate the necessity for high-quality FST data. The guiding assumption is that developing predictive TSC models is a difficult applied mechanics task and rigorous model validation using FSTs is essential because present models are relatively new and broad SBD pipeline service experience is lacking. Consider the following scenario: a forecast from a relatively recent TSC model does not match the result of an FST, and no evident testing abnormalities are discovered. Is the model incorrect, or is there an issue with the test? If the model is defective, the next step is to upgrade. If the test fails, failure analysis is necessary to uncover the root reason. The defect geometry may not have been as expected, or a brittle fracture may have happened, in which case the test should be disregarded. In view of the time/cost required to conduct these tests, there will certainly be opposition to abandoning an FST, but it is occasionally essential. Consider a second scenario in which an FST is performed as a final proof test of project materials, and the model forecast differs from the outcome. A similar dilemma arises: is it better to solve a model problem or a test problem? If the pipeline project is on a tight schedule, this

scenario might be challenging, especially if the test falls short of the goal TSC. Concluding that project materials do not fulfil design goals is a risk that may be avoided by paying close attention to all FST aspects. Late project adjustments are limited, and they frequently include more stringent defect acceptance criteria, which can be expensive. Unless addressed through failure analysis (see, e.g. (EPRG, 2014)), problematic FSTs constitute roadblocks to advancement because they raise unresolved issues about whether bad predictions were generated by an erroneous model, a flawed FST, or a mix of both.

2. 3. Model development vs. project work

The aim to isolate the influence of particular factors on strain capacity is a fundamental difference between FSTs for model development and FSTs for project work.

A sequence of FSTs for model building, for example, might be developed with steadily rising defect sizes while keeping all other factors constant. The aim will be risky if variables other than defect size alter accidentally. It can be challenging to maintain consistency in crucial aspects such as weld strength, which affects mismatch, given the volume of test specimen manufacture.

As a result, because 1G-rolled, automated welding techniques are exceedingly consistent, they are excellent for FSTs connected to model making. Because of the size of the specimens, the importance of test variable control cannot be overstated. Engineers have been battling welding-induced fracture differences in specimens (Charpy V-notch, CTOD) orders of magnitude less than full-scale pipe strain tests for decades. Because of the amount of girth weld material in an FST and the possibility for fluctuation along the circumference, all elements of specimen fabrication, especially those impacting strength or toughness, must be closely monitored.

When the FST is employed for project work, however, the welding technology will be determined by the pipeline fabrication processes. The 5G position is usual for field welding; however, semi-automatic or manual methods may also be employed. With project processes, a larger degree of girth welding variation is unavoidable; nonetheless, this variation is allowed because the purpose of project work is to proof test any variances that may occur within the authorized techniques (Bolton, Semiga, Tiku, Dinovitzer, & Zhou, 2011), (Chapetti, Otegui, Manfredi, & Martins, 2001) (Bastola, et al., 2016).

3. DESIGN AND PREPARATION OF THE SPECIMEN

3. 1. Bending vs. tensile loading:

For actual pipes, strain-based loading will nearly always result in bending; nonetheless, tensile loading is recommended for full-scale testing for various reasons. If the goal of the test is to develop a model, sample statistics are critical, and it is best to include as many notches as feasible without risking other objectives (see Figures 1 and 3). For example, two endplates and two loading tongues are included in a pipe model; each is represented by reference nodes with eccentricity from the pipe's longitudinal axis. To replicate properly welded connections, the tie constraint was applied to link the endplates to the shell pieces. Finally, the experimentally applied eccentric loading was modelled using a tie constraint connecting the loading tongues to the endplates with eccentricity. The CMOD values for tests and models were compared (Elyasi, et al., 2021) (see Figure 6).

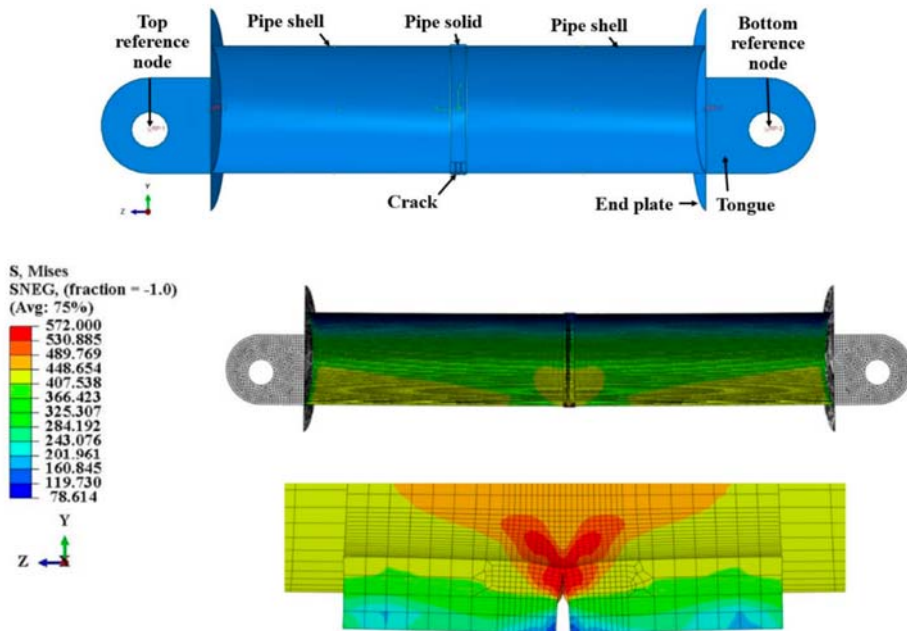


Figure 6 Assembled components of pipeline model and CMOD at the failure (Elyasi, et al., 2021)

In bending FSTs, stresses are spread non-uniformly throughout the circle, and it is typical to notch at the greatest strain site, which is the outer fibres on the tensile side (Darcis P. P., et al., 2009), (Darcis P. , et al., 2010), (Demofonti, Mannucci, Hillenbrand, & Harris, 2004). Bending tests are limited to one or two notches since there usually are only one or two welds per specimen with just one notch per weld. Four-point testing setup and an example of a silicon replica used to measure CMOD, CTOD, and Δa (crack extension) can be seen in Figure 7 (Bastola, et al., 2016).

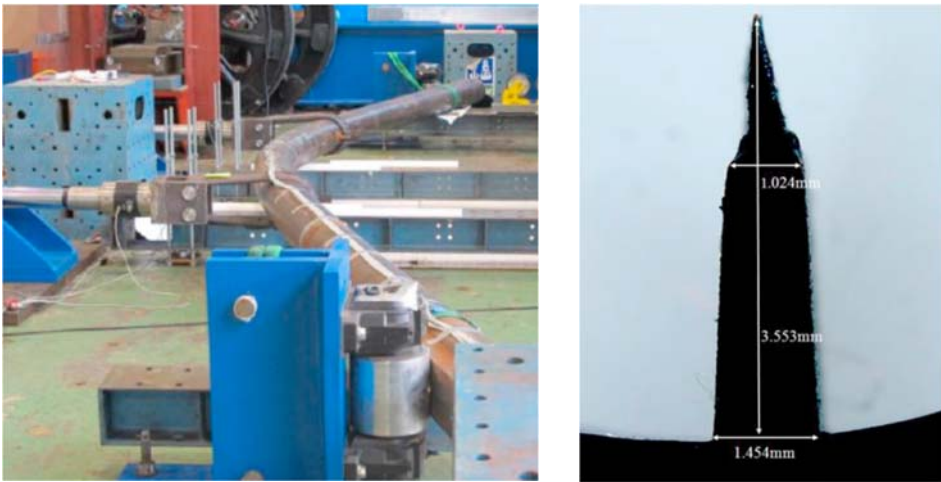


Figure 7 Four-point testing setup and an example of measured notch dimensions [19]

For project-related FSTs, sampling statistics might also be a source of worry. The advantage of many notches is significant insurance against the obstacles of full-scale testing, given the difficulty of notch placement, equipment dependability, and material variability. The potential of buckling is another reason why bending tests might be troublesome. The strain capacity of the notched region cannot be evaluated if a buckle (wrinkle) arises on the compression side of the specimen (a rather typical occurrence). When the specimen wrinkles, constant straining is no longer possible. Wrinkling can jeopardize FST goals if the goal is to evaluate the full strain capacity of the materials involved.

3. 2. Pup selection and basic design

Preparation is much simpler if the FST is on the base pipe; tests using girth welds are more complex. Figure 1 shows a schematic of an FST specimen. This design

consists of two girth welds that connect three pipe segments known as pups. To develop dependable techniques to accomplish the intended weld joint MA, weld strength overmatch, fault size, and flaw locations, design considerations, and quality controls are required (Bajcar, Cimerman, Širok, & Ameršek, 2012), (Demofonti, Mannucci, Spinelly, Barsanti, & Hillenbrand, 2002), (Di Vito, et al., 2012), (Haagensen, Maddox, & Macdonald, 2003).

In FSTs with girth welds, the number of girth welds (and hence pups) to include must be decided. The Authors have worked with various welds ranging from one to four (which means two to five pups). More girth welds provide the benefit of improving testing statistics. It permits additional artificial faults (basically notches) to be included, thereby turning a single FST into as many fracture tests as there are notches. More welds and notches have the disadvantage of increasing specimen complexity, preparation time, and the chance for mistakes, not to mention limiting the capacity of test machines. The Authors prefer the configuration depicted in Figure 1 (two welds, three pups) based on their experience since it appears to maximize the conflicting elements.

Another factor to consider is the length of the pup. Pups must be long enough to avoid interfering with neighbouring welds and/or end caps. The authors recommend a minimum pup length of 1.5 to 2 outside diameters (OD) since this provides a total specimen length (many diameters) that more closely resembles an actual strain event in a pipeline. Pipe-soil interactions are beyond the scope of this work; suffice it to state that the length of a real pipeline exposed to the whole target demand is expected to be no less than a few diameters. As a result, FST specimens of at least a few diameters appear to be acceptable (Hertelé, Cosham, & Roovers, 2016), (Kristoffersen, Haagensen, & Rørvik, 2008), (Horn, Lotsberg, & Orjaseater, 2018), (Hertelé, de Waele, Denys, Verstraete, & van Wittenberghe, 2012).

It is possible that a decision on the pups' origins will be required. If there is just one pipe available to construct the specimen, the choice is clear. If numerous pipelines are present, however, the upstream source may change. If the test aims to make a model, the pups for each specimen should be cut immediately adjacent to each other and then welded back together in their original arrangement. This reduces variance in strain capacity across pups while maintaining the purpose of evaluating only one variable. If the FST is tied to a project, the original source is less important. The aim can be achieved as long as the puppy reflects the project material.

There have been instances where pups from different pipes were utilized, and test interpretation was challenging owing to differences in pipe qualities. In general, if combining puppies from separate pipes serves no benefit, this procedure should be avoided.

3.3. Prior material knowledge

Materials with which the designers have existing expertise should be used in the design and production of specimens for model building aims. This involves understanding the pipe longitudinal characteristics, weld strength, and weld toughness, at a minimum. Pre-testing can be quite beneficial; FST design and production should be guided by base metal tensile testing, welding trials, and measurement of weld characteristics. It is vital to remember that the FST specimen will have different material than any pre-tests, and there is a chance that there may be unanticipated alterations in the specimen (Lukács, Koncsik, & Chován, 2021), (Lei, et al., 2015), (Maddox, Speck, & Razmjoo, 2008), (Maddox & Zhang, 2008). Obtaining the correct degree of weld strength mismatch is one of the most essential parts of test specimen design and manufacturing. One of the most important factors affecting girth weld strain capacity is overmatch. Unexpected test findings have been linked to unintended overmatch variation, notably lower than desired overmatch.

Longitudinal tensile samples can be collected from rings cut right near to the pipe edges that will be bevelled for welding to assess pipe tensile qualities. If this is not possible, samples should at the very least be collected from the pipe that will supply the FST pups. Trial welding and all-weld metal testing are required without prior knowledge of weld metal qualities. Measuring weld tensile characteristics (which are used to calculate mismatch) may be difficult, thus planning ahead of time for pipe/weld geometry and tensile specimen shape is recommended.

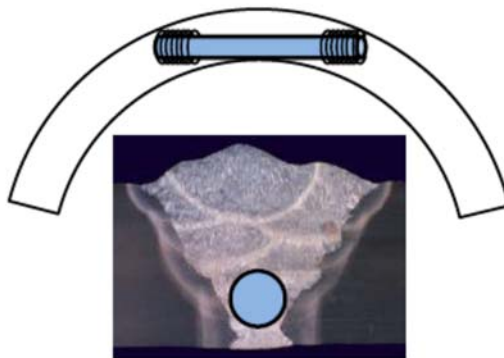


Figure 8 Four-point testing setup and an example of measured notch dimensions (Fairchild, Shafrova, Tang, Crapps, & Cheng, 2014)

The sample region must be weighed against the location of the FST notch. A round bar sample for small diameter pipe will be skewed toward the weld root (see Figure 8 (Fairchild, Shafrova, Tang, Crapps, & Cheng, 2014)), which may not reflect overall weld strength or be consistent with an FST notched from the OD.

If the pipe wall thickness approaches 25 mm, two round bar specimen sites in the weld cross section should be considered, one higher and one lower. A rectangular cross section specimen is an alternative to the round bar geometry. This specimen has been recommended for narrow groove welds, but because the design samples a larger quantity of weld metal than round bars, it has merit regardless of bevel form (Mahdavi, Kenny, Phillips, & Popescu, 2013), (Spinelli & Prandi, 2012), (Netto, Botto, & Lourenço, 2008).

3. 4. Notches

3. 4. 1. Internal vs. external notches

FST notches can be cut into the pipe's inside diameter (ID) or outside diameter (OD). A variety of factors influence this decision. Because of access issues, ID notches are impracticable for pipes with a diameter of less than DN450-DN500 (18-20"). It is technically viable to apply ID notches if the FST is significant enough for access, but the test will be pressured; nevertheless, the inside environment (water) considerably increases test complexity and restricts the durability of notch instrumentation. The chance of losing ID signals during the test is high.

Several authors have shown that real pipeline failures occur more frequently at the root than at the cap, owing to the higher risk of root faults. FSTs from the ID are more likely to be notched because of this reality (Lukács, Nagy, Harmati, Koritárné, & Kuzsella, 2012), (da Costa Mattos, et al., 2016), (Örjasæter, Hauge, Bårs, & Kvaale, 2004), (Meiwes, Höhler, Erdelen-Peppler, & Brauer, 2014), (Örjasæter, Knagenhjelm, & Haagenzen, 2008). However, in the presence of superimposed bending and the resulting bending stresses, external notches on the tensioned side can significantly reduce the lifetime of a real pipeline session. Such stresses can be caused by several factors, such as construction, ground movements (Kristoffersen, Haagenzen, & Rørvik, 2008), (Rofooei, Jalali, Attari, & Alavi, 2012), and climatic changes.

3. 4. 2. Cracks vs. notches

Large-scale fracture mechanics tests are essentially what FSTs are. Because of the influence of defect tip acuity and the possibility for brittle fracture in structural steels and their welded joints, fracture tests have traditionally been done with fatigue precracks (ISO 12135, 2021), (ISO 15653, 2018), (ASTM E647-15e1,

2015). Precracks, on the other hand, are extremely difficult to implement in full-scale pipe specimens.

FSTs for SBD are currently done with notches. SBD circumstances necessitate careful consideration of design elements and material integrity. Both the pipe and the weld materials must be ductile, and a comprehensive materials testing procedure must show this. Other tests (Charpy impact, CTOD) can be used to confirm ductile behaviour in more traditional methods. After that, FSTs can be performed using sharp notches rather than precracks because both will operate similarly in a ductile material. The results of SENT testing have corroborated this. The breadth of the notch should be kept to roughly 0.2 mm.

Low-temperature testing may be relevant because of the brittle fracture worry; nevertheless, for model construction FSTs, room-temperature testing can be justified. This is because SBD models are only applicable to ductile behaviour by definition. If the test materials are suspected of not being ductile at room temperature, Charpy and/or CTOD testing should be conducted to guarantee that the test will not be hampered by brittle behaviour. If the testing is for a project, the test temperature may be determined by the application's severity. If the service temperature is expected to be very low (below -10°C), it could be careful to execute at least some investigations at that temperature.

3. 4. 3. The quantity of notches

Because it enhances test statistics (number of investigated notches), it is preferable to include as many notches as feasible in an FST. Too many notches, on the other hand, may produce interaction between neighbouring notches, jeopardizing the test findings (unless flaw interaction is the goal (Lukács, Kocsik, & Chován, 2022)). To investigate interaction effects and improve notch spacing, FEA can be employed. For pipe diameters smaller than roughly DN700 (30"), two notches spaced 180° apart are usually utilized. For pipes ranging from DN700 (30") to DN1150 (42"), three evenly spaced notches can be utilized. Four notches might be considered for bigger pipes. The flexibility to adjust notches in the last phases of specimen preparation and/or to obtain the desired level of MA must be balanced with an aggressive notch number strategy. After the weld MA and non-destructive examination (NDE) results are known, the notch placements may be finalized. The target MA may be only found in a few places. To reach the right MA or prevent weld defects, it may be required to shift notches a substantial distance from the initial plan.

3. 4. 4. Misalignment in welded joints

One of the most critical factors influencing strain capacity is weld joint MA. By raising MA from zero to a few millimetres, strain capacity can be greatly decreasing (Lotsberg, 2009), (Hobbacher, 2008), (Qingshan, Yi-han, Bin, & Hanchen, 2010), (Chaudhari & Belkar, 2014), (Weeks, McColskey, Richards, Wang, & Quintana, 2014). It has been established that the pipe offset approach may be utilized to construct MA in an FST. Once the weld joint has been constructed, it is recommended that MA be measured at regular intervals around the perimeter and that this information be utilized to guide final notch placement, together with weld NDT data.

MA makes determining fault depth difficult. A schematic of probable HAZ notch placements in relation to a misaligned weld is shown in Figure 9. Despite the fact that these notches all enter the material to the same depth, the FST notch depth must be defined differently. The notch location should be consistent with the model if the FST's objective is to construct models. In the case of HAZ notches, the notch is often placed on the "lower" side of the weld, whether for model construction or project work. When compared to the "higher" HAZ position, this position is more cautious since it generates a smaller cross section between the notch tip and the weld root.

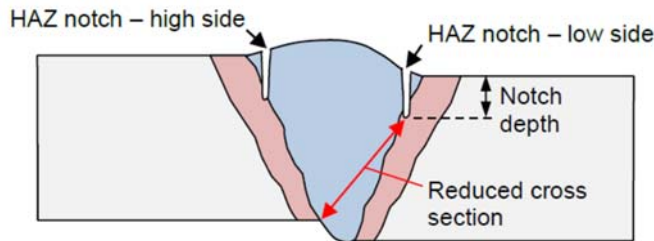


Figure 9 Possible HAZ notch positions when MA is present
(Fairchild, Crapps, Cheng, Tang, & Shafrova, 2016)

Calculation changes will be required if the notch position is at the weld centreline and the notch depth is referred to the low side of the weld (see Figure 10). The notch penetration depth is derived by multiplying the notch depth by the height of the notch entrance point X. The cap is frequently ground to assist clip gage installation, thus the weld cap in Figure 10 is rather flat to approximate this. The height of the entrance point X in this example is roughly half of the MA. The actual cap

height may differ from that depicted in Figure 10, requiring the designers to make the required changes.

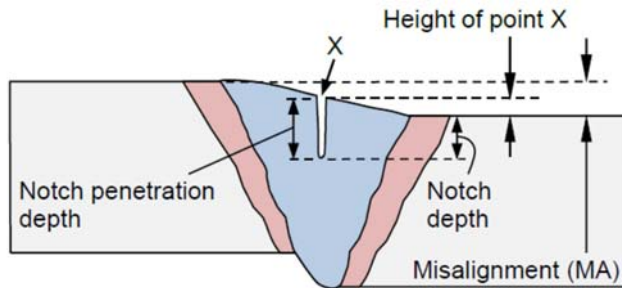


Figure 10 Weld centreline notch position showing additional considerations when MA is present (Fairchild, Crapps, Cheng, Tang, & Shafrova, 2016)

4. CONCLUSIONS

From the detailed review and processing of the references, the following main conclusions can be drawn.

- Model construction and project work are the two most common motivations for FSTs. Depending on the FST's goal, the specimen design and manufacturing, test process, and data analysis may change.
- Performing a single FST is very expensive and can be taken months. The investment necessitates meticulous pipe and weld selection, specimen construction, instrumentation, and analysis of the findings. Material variances should be kept to a bare minimum since they can jeopardize an FST.
- Misalignment makes notch insertion more complex, therefore prior planning and precise measurement are all essential. In addition, to find the notches near a (hidden) fusion line, HAZ notching necessitates using registry lines and companion cross sections.
- In an FST, the material qualities are represented by companion pipe/welds. Variations in companion materials and the FST should be avoided at all costs since they can skew the findings.
- Pipes that are utilized for SBD-related FSTs should be aged.
- Well-defined test shutdown criteria are required to get the most out of an FST.
- A comprehensive metallurgical inspection should be complemented with a rigorous assessment of all instrumentation data to obtain a complete

knowledge of specimen performance. Fractography becomes an essential part of the post-test assessment if the FST breaks. To assess the relevance of cleavage on an FST fracture surface, it should be evaluated. The presence of cleavage does not always imply that the materials are inappropriate for SBD.

- FSTs are a must-have tool for ensuring the safety of SBD pipelines. FSTs should be deemed necessary until the industry has gained considerable expertise with these pipelines and/or improved modelling (prediction) accuracy.

5. CONSEQUENCES OF DESIGNING AND EXECUTING OWN INVESTIGATIONS

The following conclusions can be drawn for designing and implementing our own full-scale investigations.

- When designing the tests, all available information and data on the pipeline sections to be tested, the actual operating conditions, the test possibilities, and the limitations should be used.
- If necessary, additional mechanical tests and microstructural investigations shall be carried out to ensure high reliability and reproducibility of the test pipeline sections. Furthermore, non-destructive examinations of girth welds are practical and necessary in connection with the essential phases of the full-scale tests (e.g. before the tests, after the fatigue tests).
- The tested pipeline sections should be constructed from the same material quality. In cases where this is not possible, special attention should be paid to differences in the properties of the pipe sections and their effects on the tested girth welds.
- The longitudinal size of the individual pipe sections used for the assembly of the tested pipeline sections should preferably exceed twice the outer diameter.
- The use of three-segment tested pipeline sections with two tested girth welds is appropriate for four-point bending tests. A three-point bending test is preferable if only one girth weld is to be tested.
- In order to model actual operating conditions as accurately as possible, applying an external (bending) load in addition to the internal (cyclic) pressure is desirable. In such cases, placing the tested girth weld in the middle of the investigated pipeline section is advisable. This will result in the highest bending stress (three-point bending) and eliminate errors due to asymmetry (four-point bending).
- Before complex load tests, it is also advisable to investigate a pipeline section that has not been subjected to cyclic loading (burst test),

furthermore a pipeline section that has not been subjected to additional loading (fatigue test followed by burst test). These investigations provide a basis for comparison with the complex loaded investigations.

- In order to model the defects of the girth welds, it is advisable to use notches. In the case of simple loads, the location of the notches along the circumference is indifferent, but in the case of complex loads, the locations with the highest stress should be prioritized.

REFERENCES

API. (2018). API Specification 5L. *Line Pipe*. American Petroleum Institute.

ASTM E647-15e1. (2015). Standard Test Method for Measurement of Fatigue Crack Growth Rates. ASTM International.

Bajcar, T., Cimerman, F., Širok, B., & Ameršek, M. (2012). Impact assessment of traffic-induced vibration on natural gas transmission pipeline. *Journal of Loss Prevention in the Process Industries*, 25(6), 1055-1068. doi:<https://doi.org/10.1016/j.jlp.2012.07.021>

Bastola, A., Wang, J., Shitamoto, H., Mirzaee-Sisan, A., Hamada, M., & Hisamune, N. (2016). Full- and small-scale tests on strain capacity of X80 seamless pipes. *Procedia Structural Integrity*, 2, 1894-1903. doi:<https://doi.org/10.1016/j.prostr.2016.06.238>

Bolton, B., Semiga, V., Tiku, S., Dinovitzer, A., & Zhou, J. (2011). Full Scale Cyclic Fatigue Testing of Dented Pipelines and Development of a Validated Dented Pipe Finite Element Model. *ASME, Proceedings of the 2010 8th International Pipeline Conference*, pp. 863-872. Calgary, Alberta, Canada. doi:<https://doi.org/10.1115/IPC2010-31579>

Chapetti, M., Otegui, J., Manfredi, C., & Martins, C. (2001). Full scale experimental analysis of stress states in sleeve repairs of gas pipelines. *International Journal of Pressure Vessels and Piping*, 78(5), 379-387. doi:[https://doi.org/10.1016/S0308-0161\(00\)00063-6](https://doi.org/10.1016/S0308-0161(00)00063-6)

Chaudhari, S. B., & Belkar, S. B. (2014). Experimental and Analytical Investigation in Circumferential Joint. *International Journal of Mechanical Engineering and Information Technology*, 2(6), 453-465.

da Costa Mattos, H. S., Reis, J. M., Paim, L. M., da Silva, M. L., Lopes Junior, L., & Perrut, V. A. (2016). Failure analysis of corroded pipelines reinforced with composite repair systems. *Engineering Failure Analysis*, 59, 229-236. doi:<https://doi.org/10.1016/j.engfailanal.2015.10.007>

Darcis, P. P., Marines-Garcia, I., Di Vito, L., Richard, G., Ruiz, E. A., de Souza, M., . . . Quintanilla, H. (2009). Fatigue Performance of SMLS SCR Girth Welds: Comparison of Prefabrication-Type WPS. *ASME, Proceedings of the ASME 2009 28th International Conference on Ocean, Offshore and Arctic Engineering*, pp. 683-692. Honolulu, Hawaii, USA. doi:<https://doi.org/10.1115/OMAE2009-79811>

Darcis, P., Marines-Garcia, I., Ruiz, E., Marques, E., Armengol, M., & Quintanilla, H. (2010). Full Scale Fatigue Performance of Pre-Strained SCR Girth Welds: Comparison of Different Reeling Frames. *ASME, Proceedings of the ASME 2010 29th International Conference on Ocean, Offshore and Arctic Engineering*, pp. 1039-1049. Shanghai, China. doi:<https://doi.org/10.1115/OMAE2010-21025>

Demofonti, G., Mannucci, G., Hillenbrand, H.-G., & Harris, D. (2004). Evaluation of the Suitability of X100 Steel Pipes for High Pressure Gas Transportation Pipelines by Full Scale Tests. *ASME, Proceedings of the 2004 International Pipeline Conference*, pp. 1685-1692. Calgary, Alberta, Canada. doi:<https://doi.org/10.1115/IPC2004-0145>

Demofonti, G., Mannucci, G., Spinelly, C., Barsanti, L., & Hillenbrand, H. (2002). *Large-diameter X 100 gas line pipes: Fracture propagation evaluation by full-scale burst test*. EUROPIPE GmbH. Retrieved October 15, 2022, from https://www.academia.edu/7397114/Large_diameter_X_100_gas_line_pipes_Fracture_propagation_evaluation_by_full_scale_burst_test

Di Vito, L., Lucci, A., Amato, S., Mannucci, G., Tintori, F., Crippa, S., . . . Quintanilla, H. (2012). Ultra Heavy Wall Linepipe X65: Full Scale Severe Straining Sequences of Pipeline Strings. *ASME, Proceedings of the ASME 2012 31st International Conference on Ocean, Offshore and Arctic Engineering*, pp. 695-705. Rio de Janeiro. doi:<https://doi.org/10.1115/OMAE2012-83835>

Elyasi, N., Shahzamanian, M., Lin, M., Westover, L., Li, Y., Kainat, M., . . . Adeb, S. (2021). Prediction of Tensile Strain Capacity for X52 Steel Pipeline

Materials Using the Extended Finite Element Method. *Applied Mechanics*, 2(2), 209-225. doi:<https://doi.org/10.3390/applmech2020013>

EPRG. (2014). EPRG Guidelines on the Assessment of defects in transmission pipeline girth welds - Revision 2014. European Pipeline Research Group e. V. Retrieved October 15, 2022, from https://www.eprg.net/fileadmin/EPRG_public/eprg-docs/guidelines/EPRG_Weld_Defect_guidelines.pdf

Fairchild, D. P., Crapps, J. M., Cheng, W., Tang, H., & Shafrova, S. (2016). Full-Scale Pipe Strain Test Quality and Safety Factor Determination for Strain-Based Engineering Critical Assessment. *ASME, Proceedings of the 2016 11th International Pipeline Conference Pipeline Safety Management Systems; Project Management, Design, Construction and Environmental Issues; Strain Based Design; Risk and Reliability*, p. 12 pages. Alberta, Canada. doi:<https://doi.org/10.1115/IPC2016-64191>

Fairchild, D. P., Shafrova, S., Tang, H., Crapps, J. M., & Cheng, W. (2014). Full-Scale Testing for Strain-Based Design Pipelines: Lessons Learned and Recommendations. *ASME, Proceedings of the 2014 10th international Pipeline Conference Production Pipelines and Flowlines; Project Management; Facilities Integrity Management; Operations and Maintenance; Pipelining in Northern and Offshore Environments; Strain-Based Design*, p. 12 pages. Alberta, Canada. doi:<https://doi.org/10.1115/IPC2014-33748>

Haagensen, P., Maddox, S., & Macdonald, K. (2003). Guidance for Fatigue Design and Assessment of Pipeline Girth Welds. *ASME, Proceedings of the ASME 2003 22nd International Conference on Offshore Mechanics and Arctic Engineering*, pp. 377-395. Cancun, Mexico. doi:<https://doi.org/10.1115/OMAE2003-37496>

Hertelé, S., Cosham, A., & Roovers, P. (2016). Structural integrity of corroded girth welds in vintage steel pipelines. *Engineering Structures*, 124, 429-441. doi:<https://doi.org/10.1016/j.engstruct.2016.06.045>

Hertelé, S., de Waele, W., Denys, R., Verstraete, M., & van Wittenberghe, J. (2012). Parametric finite element model for large scale tension tests on flawed pipeline girth welds. *Advances in Engineering Software*, 47(1), 24-34. doi:<https://doi.org/10.1016/j.advengsoft.2011.12.007>

Hobbacher, A. (2008). Recommendations for Fatigue Design of Welded Joints and Components. International Institute of Welding.

Horn, A., Lotsberg, I., & Orjaseater, O. (2018). The Rationale for Update of S-N Curves for Single Sided Girth Welds for Risers and Pipelines in DNV GL RP C-203 íbased on Fatigue Performance of More than 1700 Full Scale Fatigue Test Results. *ASME, Proceedings of the ASME 2018 37th International Conference on Ocean, Offshore and Arctic Engineering*, p. V004T03A024; 10 pages. Madrid, Spain. doi:<https://doi.org/10.1115/OMAE2018-78408>

Igi, S., Muraoka, R., & Masamura, K. (2013). *Safety and Integrity Assessment Technology for Linepipe*. JFE. Retrieved October 15, 2022, from <https://www.jfe-steel.co.jp/en/research/report/018/pdf/018-06.pdf>

ISO 12135. (2021). Metallic materials. *Unified method of test for the determination of quasistatic fracture toughness*. International Organization for Standardization.

ISO 15653. (2018). Metallic materials. *Method of test for the determination of quasistatic fracture toughness of welds*. International Organization for Standardization.

Koncsik, Z. (2019). A szerkezetintegritás helye és szerepe az oktatásban és a kutatásban. *Multidiszciplináris Tudományok*, 9(4), 63-71. doi:<https://doi.org/10.35925/j.multi.2019.4.5>

Koncsik, Z. (2021). Szerkezetintegritási kutatások az Innovatív Anyagtechnológiák Tudományos Műhelyben. *Multidiszciplináris Tudományok*, 11(2), 372-379. doi:<https://doi.org/10.35925/j.multi.2021.2.49>

Kristoffersen, S., Haagenen, P., & Rørvik, G. (2008). Full Scale Fatigue Testing of Fatigue Enhanced Girth Welds in Clad Pipe for SCRs Installed by Reeling. *ASME, Proceedings of the ASME 2008 27th International Conference on Offshore Mechanics and Arctic Engineering*, pp. 169-177. Estoril, Portugal. doi:<https://doi.org/10.1115/OMAE2008-57309>

Lei, Z., Chen, J., Wang, F., Xuan, W., Wang, T., & Yang, H. (2015). Full-scale Burst Test and Finite Element Simulation of 32 Inch Oil Pipe with Girth Weld Defects. *Procedia Engineering*, 130, 911-917. doi:<https://doi.org/10.1016/j.proeng.2015.12.240>

Li, Z., Gong, B., Lacidogna, G., Deng, C., & Wang, D. (2021). Strain-based fracture response of X80 steel pipe welded girth based on constraint-modified J-R curves: from SENT specimen to full-scale pipe. *Engineering Fracture Mechanics*, 258. doi:<https://doi.org/10.1016/j.engfracmech.2021.108114>

Lotsberg, I. (2009). Stress Concentrations due to misalignment at butt welds in plated structures and at girth welds in tubulars. *International Journal of Fatigue*, 31, 1337-1345. doi:<https://doi.org/10.1016/j.ijfatigue.2009.03.005>

Lukács, J., Koncsik, Z., & Chován, P. (2021). Integrity reconstruction of damaged transporting pipelines applying fiber reinforced polymer composite wraps. *Procedia Structural Integrity*, 31, 51-57. doi:<https://doi.org/10.1016/j.prostr.2021.03.009>

Lukács, J., Koncsik, Z., & Chován, P. (2022). Integrity increasing of damaged transporting pipelines using fiber reinforced polymer composite wrap systems. *Engineering Failure Analysis*, 137, 106284. doi:<http://doi.org/10.1016/j.engfailanal.2022.106284>

Lukács, J., Nagy, G., Harmati, I., Koritárné, F. R., & Kuzsella, L. K. (2012). *Szemelvények a mérnöki szerkezetek integritása témaköréből*. Miskolc: Miskolci Egyetem.

Maddox, S. J., & Zhang, Y. H. (2008). Comparison of fatigue of girth-welds in full-scale pipes and small-scale strip specimens., *Proceedings of the International Conference on Offshore Mechanics and Arctic Engineering* , pp. 75-85. doi:<https://doi.org/10.1115/OMAE2008-57103>

Maddox, S. J., Speck, J. B., & Razmjoo, G. R. (2008). An investigation of the fatigue performance of riser girth welds. *Journal of Offshore Mechanics and Arctic Engineering* , 130(1), 011007, 11 pages. doi:<https://doi.org/10.1115/1.2827956>

Mahdavi, H., Kenny, S., Phillips, R., & Popescu, R. (2013). Significance of geotechnical loads on local buckling response of buried pipelines with respect to conventional practice. *Canadian Geotechnical Journal*, 50(1), 68-80. doi:<https://doi.org/10.1139/cgj-2011-0423>

Meiwes, K. C., Höhler, S., Erdelen-Peppler, M., & Brauer, H. (2014). Full-Scale Reeling Tests of HFI Welded Line Pipe for Offshore Reel-Laying Installation.

ASME, Proceedings of the 2014 10th International Pipeline Conference, p. V004T10A004. Calgary, Alberta, Canada. doi:<https://doi.org/10.1115/IPC2014-33163>

Netto, T. A., Botto, A., & Lourenço, M. I. (2008). Fatigue performance of pre-strained pipes with girth weld defects: Local deformation mechanisms under bending. *International Journal of Fatigue*, 30(6), 1080-1091. doi:<https://doi.org/10.1016/j.ijfatigue.2007.08.001>

Ørjasæter, O. L., Knagenhjelm, H. O., & Haagensen, P. J. (2008). Scale Effects: Correlation of Fatigue Capacity for Full-Scale Pipes and Small-Scale Specimens. *ASME, Proceedings of the ASME 2008 27th International Conference on Offshore Mechanics and Arctic Engineering*, pp. 485-496. Estoril, Portugal. doi:<https://doi.org/10.1115/OMAE2008-57997>

Ørjasaeter, O., Hauge, O. J., Børs, G., & Kvaale, P. E. (2004). Crack Growth During Full Scale Reeling Simulation of Pipes With Girth Welds. *ASME, Proceedings of the ASME 2004 23rd International Conference on Offshore Mechanics and Arctic Engineering*, pp. 193-199. Vancouver, British Columbia, Canada. doi:<https://doi.org/10.1115/OMAE2004-51365>

Qingshan, F., Yi-han, L., Bin, L., & Hanchen, S. (2010). Failure Assessment for Girth Weld Defects of Pipeline., *Proceedings of the 8th International Pipeline Conference*, p. 7 pages. Calgary, Alberta, Canada.

Rofooei, F. R., Jalali, H. H., Attari, N. K., & Alavi, M. (2012). Full-Scale Laboratory Testing of Buried Pipelines Subjected to Permanent Ground Displacement Caused by Reverse Faulting. *SPES Sociedade Portuguesa de Engenharia Sísmica, Proceedings of the 15th World Conference on Earthquake Engineering 2012*, pp. 24508-24518. Lisbon, Portugal.

Spinelli, C. M., & Prandi, L. (2012). High Grade Steel Pipeline for Long Distance Projects at Intermediate Pressure., *7th Pipeline Technology Conference*, p. 9 pages.

Thaulow, C., Østby, E., Nyhus, B., Zhang, Z., & Skallerud, B. (2004). Constraint correction of high strength steel: Selection of test specimens and application of direct calculations. *Engineering Fracture Mechanics*, 71(16-17), 2417-2433. doi:<https://doi.org/10.1016/j.engfracmech.2004.01.003>

Weeks, T. S., McColskey, J. D., Richards, M. D., Wang, Y., & Quintana, M. (2014). Curved-Wide Plate Testing of X100 Girth Welds. *Proceedings of the 2014 10th International Pipeline Conference*, pp. V004T11A020, 19 pages. Calgary, Alberta, Canada: ASME. doi:<https://doi.org/10.1115/IPC2014-33690>

Wei, Z., Jin, H., Pei, X., & Wang, L. (2021). A simplified approach to estimate the fatigue life of full-scale welded cast steel thin-walled tubular structures. *Thin-Walled Structures*, 160, 107348. doi:<https://doi.org/10.1016/j.tws.2020.107348>

Xuan, W., Wang, F., Zhou, L., Wang, T., Chen, J., Lei, Z., & Yang, H. (2016). Reserach on Full-Scale Hydrostatic Burst Testing of Different Pipeline Girth Weld Defects. *Applied Mechanics and Materials*, 853, 351-355. doi:<https://doi.org/10.4028/www.scientific.net/AMM.853.351>

Yang, Y., Liu, X., Wu, K., Sui, Y., Feng, Q., Wang, D., & Zhang, H. (2022). Full-scale experimental investigation of the fracture behaviours of welding joints of APL X80 wide plate based on DIC technology. *Engineering Failure Analysis*, 131, 105832. doi:<https://doi.org/10.1016/j.engfailanal.2021.105832>

Zhang, Y., & Maddox, S. (2014). Fatigue testing of full scale girth welded pipes under variable amplitude loading. *Journal of Offshore Mechanics and Arctic Engineering*, 136(2), 021401. doi:<http://doi.org:10.1115/1.4026025>

VEHICLE EMBLEMS FROM NATURE

DÖMÖTÖR, CSABA

*University of Miskolc, Department of Machine and Product Design,
H-3515, Miskolc-Egyetemváros
csaba.domotor@uni-miskolc.hu
<https://orcid.org/0000-0002-6406-3460>*

Abstract: Copying principles and functions from nature, or even a particular shape, construction, colouration, or pattern is most often a rewarding business. By using shapes that have long been known and thus rooted in human subconsciousness, users can design products that show durability, create confidence or simply be usable and appealing in shape or colour. This is true even if the natural analogy found is not due to the product itself, but to the graphic element of the logo of the company. This article systematizes the natural motifs found in the emblems of the automotive industry and illustrates their effects in branding.

Keywords: *natural analogies, automotive, logo, emblem, branding*

1. INTRODUCTION

It is of paramount importance for the market position of a company or brand that it can be easily recognized by customers and distinguished from competitors in the market. One of the excellent tools for this is a unique sign that can obviously identify the brand and that can be clearly recognized and remembered. This sign can be the basic element of the brand's image. A good choice of these marketing-frontline emblem is often crucial to establishing a market position. Further we will consider what messages manufacturers are trying to convey with motifs adapted from nature.

1. 1. Design close-to-nature

Looking at the history of human development, it can be concluded that man spent much more time near nature than away from it. Despite new impulses, social influences or altered behaviours, therefore, the experiences previously acquired by our ancestors instinctively come to the surface. This is also to justify the fact that,

for example, one of the most suitable choices for general attention is the yellow-black pairing. The main reason for this is that due to its outstanding colour contrast, it is also often used by wildlife as a visual cue, thus becoming one of the most artificially created objects or spaces its most effective means of raising awareness (Dömötör & Péter, 2012).

Similarly, following natural principles or processes, it is possible to suggest different properties either through a design or through a well-designed emblem. A good designer generally strives for consistency between content and form, it's common to think that it's not enough to be streamlined/fast/reliable/durable to be, it must be seen. Logos are a good tool for such indirect communication. The message they convey nonverbally can reach the customer as if it were their own self-recognition, so it is likely to be unquestionable in them it will condense as information.

1. 2. Grouping close-to-nature car logos

Most car manufacturers operate as part of a long-standing group of companies, so in many cases the logo of a brand reflects ownership, market, fashion or even user needs it has undergone several changes to this day. In most cases, these changes keep the main motifs, but in some cases, they bring a radically new design. This article deals with the current car emblems of our time, but in some cases –especially related to Hungary– it also looks back at the memories of past times. There are several options for grouping emblems adapted from nature, but in our case the main formal element as a defining motif is the classification criterion.

The basic topic of this article is car emblems using motifs found in nature. Taking a closer look at these, the categories described in detail in Chapter 2 can be created. Among them, we can typically find analogies from the animal world, but in the history of car manufacturing, there was also a recurring motif from the plant known for its characteristic, massive, shiny leaves, a wreath made of laurel branches. Common examples from the animal kingdom include flight-related wings and birds, but horses that are well-established in transport also play a prominent role. Predators are often used by manufacturers, but there are also several examples of mythological creatures. Among the herbivorous animals, motifs referring to ruminants form an even larger set, while the category of creepers closes the line.

2. NATURAL SYMBOLS

Before we examine the listed groups in more detail, it is worth considering the Hungarian aspects of the topic as well. Our country never achieved a world market role in the field of self-developed and mass-produced passenger car production,

but we achieved outstanding economic results in the segment of truck and bus production, where the most important players in the domestic industry were Ganz, Rába and Ikarus.



Figure 1 The Hungarian Puli small car (a) and Komondor military vehicle (b)

In connection with this topic, it is possible to mention the Puli two-seater plastic body urban small car (Figure 1.a), which was produced between 1986 and 1998 by Hódgép in Hódmezővásárhely (Négyesi, 2011). In the same way, the Komondor, presented in 2012, which is a military chemical reconnaissance vehicle of Gamma Műszaki Zrt. with light armour protection (Figure 1.b), was developed and manufactured in Hungary (MTI, 2015). The fact that an ancient Hungarian dog breed was chosen as the name for both vehicles, while the dog is particularly rarely mentioned in other manufacturers' emblems, brand, or model names, even though these animals are symbols of loyalty, devotion, strength and endurance.

2. 1. Plants

In the field of car emblems, the flora provides far fewer examples in proportion, but there is a motif that several manufacturers have preferred to use in their badges. And this is the laurel, which, however, does not carry a message for us in its natural state, but in a man-made object symbolizing victory and glory. This wreath braided from an evergreen plant has been a reward for withering merits since the ancient Greeks. It is interesting that such headdresses were also made of almond pine, celery or olive branch depending on the geographical conditions.



Figure 2 Branding with wreaths of glory

Due to the outstanding advertising value of victories in car races, the use of a victory wreath was much more popular at the beginning of motoring, and then slowly faded from use. Accordingly, none of the brandings shown in Figure 2 are current logos of the given manufacturer. Among them, the Cadillac emblem, which appears first in the reverse order of their disappearance, is the youngest, and by the way, the laurel wreath disappeared from it in 2014.

2. 2. Wings, birds

The most frequently used symbols of all time are the wings, which show the manufacturer's aspiration towards heights. Sometimes they just frame a central inscription or shape, but other times they themselves are the main motif. The Figure 3 shows that occasionally the emblem follows the shape of the wing with almost anatomical accuracy, but in most cases it is only displayed in a stylized way.

In Figure 3, from left to right and top to bottom, the first detail of the winged letter "B" of the British Bentley is that, uniquely, the tail feathers of birds are also appear. According to the manufacturer's communications, by the way, bird wings are intended to symbolize speed and independence. Much more symbolic is the Mazda logo (Figure 3b), which features the letter "M" of the brand name, but the "V" shape on the inside evokes the silhouette of a bird flying in the distance, which symbolizes the unfolding of the company's wings in the direction of the future. The logo is also meant to display the creativity, sense of mission and vitality of the brand. The soaring rim motif of the next Mini in line is itself a telling automotive reference that originally appeared in the Morris emblems but is still used today. Figures 3 d-e are unique identification plaques for each Hyundai model. The first emblem depicting a pair of wings and a soaring bird in a rounded trapezoid appears exclusively on the manufacturer's luxury cars under the name Equus, as in the Genesis the Korean company also has a unique mark on its premium brand. Figures 3.f-h show the logos of two British car manufacturers. The legendary and successful Aston Martin has wings on its logo in the same way as Morgan, which builds unique old-style cars that use modern technical solutions within. In the middle, Figure 3.g shows the old logo of the Hungarian Ikarus buses, with a wing motif at the bottom, which evokes the eponymous Ikarus, since according to Greek mythology he was the first person to fly. He embodied an openness to novelty, a desire for human ambition, overcoming fear, and the idea that human ingenuity can work wonders. But at the same time, Icarus has also become synonymous with rebellion, wordlessness and curiosity, qualities that often drive an innovative manufacturer forward.



Figure 3. Using wing motif on car emblems

In the third line of Figure 3 we find the emblems of Chinese manufacturers. The soaring bird silhouette, shaped from five red diamonds, is the symbol of SAIC Wuling Automobile, which specializes mainly in the production of minivans, and is now part of the General Motors group. The asymmetrical winged “1” logo denotes the products of China's largest truck manufacturer, the Jiefang – FAW Group, founded in 1953. Finally, one of the most successful Chinese manufacturers is the winged emblem surrounding the horse head of Geely-owned LEVC (London Electric Vehicle Company), which is not clearly Pegasus, but rather soaring and he wishes to combine nobility into himself. The company has been negotiating with the British government to produce electric taxis in London, although the proliferation of these vehicles is yet to come. However, given the parent company's wide-ranging ambitions – they are also competing successfully in the WTCR – it cannot be ruled out that an increasing number of such cars will soon be used in London to help the air pollution reduction.

Due to its shape, it forms a transition between wing motifs and bird figures with the falcon emblem that appears on the Trailhawk-equipped models of the Jeep brand shown in Figure 4.a. Also known for its excellent eyesight, the silhouette of a raptor circling in the sky tells the user that he can safely start on any terrain, because he will find the right path, on which the brand's model with the best off-road capabilities currently available will surely succeed.

So it can be seen that instead of only depicting wings, the image of the entire bird can also appear on the emblems. The message is similar to the previous ones, but such badges already convey the aerodynamic beauty and functionality embodied by the birds. The eagle is common as a symbol. This predator, considered the king of birds and the air and sky, carries a message of courage, determination, strength

and greatness. In the same way, the wandering falcon is also a popular choice among supercar manufacturers, which has a reason. When falling under control while hunting, it can reach a top speed of over 400 km/h, making it the fastest animal on Earth.

The old logo of New Zealand's Saker Sports Cars company depicted the falcon still in falling flight, which was more of an expression of speed, but the current dynamically lined hawkhead (Figure 4.b) is also distinctly streamlined effect. The image of a hunting falcon hitting a prey on the American Rossion and the British Arash supersport cars sends a message of the aggressive appearance conveyed in the design of their vehicles (Figure 4.c-d). The logo of the custom-built sports cars of the German company Isdera (Ingenieurbüro für Styling, Design und Racing) shows an eagle in a light blue field, similarly while hunting (Figure 4.e).



Figure 4 Bird depictions on car emblems

Chrysler sold passenger cars under the Eagle brand name with an eagle head emblem (Figure 4.f), but these cars ceased to be marketed. Similarly, in 2007, production of Toyota MR2 mid-engined sports car, which bore the unique emblem in Figure 4.g, was completed. According to a statement from Toyota, it's a 'bird that represents the aerodynamic beauty created through evolution', but the owners ironically just label the motif as a 'screaming chicken'. In the line of old badges, it is also worth mentioning the logo of Dacia, well-known in our country until 1978, which depicts the traditional emblem and coat of arms of Romania, that is an eagle with outstretched wings. The acronym UAP at the top of the shield stands for 'Uzina de Autoturisme Pitesti', that means Pitesti Automobile Factory.

2. 3. Horses

Also often used automotive emblem is the horse. The possessions embodied in these royal animals evoke positive feelings in most of us and are also closely linked to the early and present mobilization of humanity. Wild horses are associated with a sense of freedom, and strength, speed and dynamism can also come to

mind about them. Draught breeds are best known for their endurance, but the hallmark of each horse is also a strong character. All these are the features that the buyer expects from a car, so from a marketing point of view it is a good choice to promise them even with the logo.

In Figure 3.k, we have already seen the horse as a symbol, but another Chinese manufacturer, Baojun, which belongs to the GM group, also uses a stylized image of this animal on his cars (Figure 5.a). The horse's head, integrated into a diamond shape introduced in 2019, was originally featured on a shield with a much more realistic representation, similar to the current emblem of an Iranian manufacturer called IKCO (Figure 5.b). With a shield known from the era of knights, the nobility of the animal is even more pronounced.

The white horse head on a red background is the emblem of the Eicher motorcycle and truck factory in India (Figure 5.c), which with its graphic elements evokes a flagging horse's mane. A more emphatic reference to speed is one of the most well-known horse-drawn car emblems found on Ford Motor Company's muscle cars called Mustang. The name was already borrowed from the small, strong-bodied horse breed, considered the wild offspring of Spanish horses imported into North America, which is also known by the well-remembered galloping horse shape illustrates (Figure 5.d). A similarly running horse is also displayed in the logo of one of the world's most prominent manufacturers of heavy trucks. With a horse running in the field on the Kamaz products (Figure 5.e), they want to emphasize the strength and agility of their cars. The manufacturer, recognized in the international market and successful in the challenges of the Dakar rally, for example, is the largest automotive company in Russia.

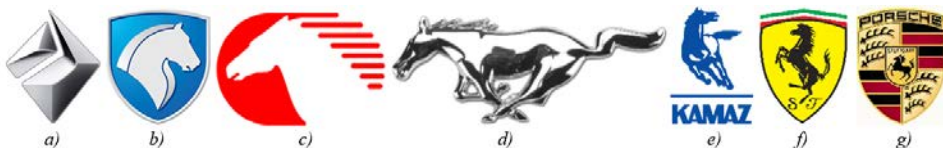


Figure 5 Displaying horses on car emblems

Even more, strength and dynamism dominate in the sight of a prancing horse. It is therefore no coincidence that Ferrari's shield, decorated with the Italian national colours and bearing the yellow colour of Enzo Ferrari's hometown, Modena, also features a confident animal (Figure 5.f). All this evokes the memory of Baracca, an Italian pilot from the First World War, who always painted a black horse on the side of his aircraft (Heptinstall, 2018). The "good luck" symbol is quite similar to the prancing horse figure that adorns the centre of the emblem of Porsche sports cars and is originally featured in the coat of arms of the manufacturer's

headquarters, the city of Stuttgart, with its posture expressing forward kicking (Figure 5.g). The stylized deer antlers on the shield refer to the heraldic animals of the historical province of Baden-Württemberg, as are the red and black bands of this province (Heptinstall, 2018). Overall, it can be concluded that horses have become important symbols of automakers not only because of the message they carry in themselves, but also because of their historical significance in ancient coats of arms.

2. 4. Predators

Unlike horses, predatory animals in most cases are not specifically our cooperative partners. However, because of their effective hunting skills and intelligence, big cats or even wolves, which are dangerous to humans, have always been respected. Predators are characterized by a skill of control, even a violent acquisition of domination. The example of their confident stance can also evoke ancient, wild instincts in man. If anyone in history could control them, their observers assumed an almost unearthly power. Because of this, they have become symbols of confidence and power. The lions also have a prominent role, as their growls and howls containing low-frequency infrasound ranges command authority. In addition, the silhouette of males with rich manes is also an old royal symbol.

Perhaps the most well-known lion car badge is found on Peugeot's products (Figure 6.a). Previously, we could see the two-legged lion facing left, known from heraldry. This emblem has also changed several times since its appearance in 1850 (most recently in 2021), but its meaning has remained the same. With its traditional appearance derived from the provincial coat of arms of the company's first seat, it expresses quality, reliability and longevity. Similar to this is the roaring lion holding the wheel in the emblem of the Australian Holden brand of General Motors (Figure 6.b). According to an ancient fabula, the idea of the wheel as an invention came from observing lions as they rolled rocks with their paws. In the case of the cooling mask decoration of MAN (M.A.N.: Maschinenfabrik Augsburg-Nuremberg) vehicles, the message is already much clearer: 'Strong as a lion' (Figure 6.c). The stylized Braunschweig lion, originally the coat of arms of Prince Henry of Saxony, was first used on its trucks in 1913 by the Büssing company, which was absorbed in the early 70's.



Figure 6 Predators

Known for its sportily elegant cars, Jaguar inspires the customer with a more aggressive message, as the very meaning of the word from the indigenous peoples of South and Central America is ‘that puts you down with a leap’. The symbol depicting the attacking jaguar clearly carries this feeling even without words (Figure 6.d). Sticking with the big cats, Figures 6.e-f-g have three very similar emblems following each other. Malaysia's Proton cars feature a roaring Malay tiger, the main motif of the South Korean Spirra supersports car emblem is simply identified as a big cat's head roaring in a triangle, while the 9ff a German tuning company specializing in rebuilding Porsche sports cars, uses a golden cat on a black shield on its rebuilt cars. In the case of the companies involved, there is no need to think about consciously copying each other. Rather, it is because of the character traits that most of us know well from domestic cats that several companies use such symbols. Chrysler, Dodge and Jeep cars are boosted by the Street & Racing Technology division of the Fiat Chrysler Automobiles group. In addition to the SRT mark, the unique logo in Figure 6.h indicates if a “Hellcat” engine has been installed in the vehicle.

Staying within predators, but moving from the big cats to canines, the list is much narrower. This is surprising, if only because the most common trait associated with dogs is loyalty, which can also be a positive value for a car. The most well-known wild dog species, the wolf, on the other hand, carries all the qualities represented by predators, but in addition, the concepts of team spirit, discipline and orderliness can also be associated with to them. They also played a role in ancient legends, as Romulus and Remus, who later founded Rome, were fed by a female wolf. This wolf was chosen as its symbol by the Italian car-building workshop Cizeta, based in Modena, which makes custom cars (Kuah, 2022). However, in the logo of Lobini, a Brazilian manufacturer of sports cars with Audi engines and fiberglass bodies, the wolf's head is much more recognizable, with sharp lines that provoke aggression they reflect, and its narrow eye opening evokes the mysteries surrounding wolves.

The motive of a real, tamed dog is even rarer. As an attempt, we can mention the leaping greyhound that briefly appeared on Lincoln cars in 1927, which evoked speed, endurance and beauty, but had no effect on the brand's later emblems. The most well-known canine car logo that still exists today is the symbol of American Mack trucks with a bulldog depicted in a ready-to-act posture waiting for the command of its owner (Figure 6.k). Just as a curiosity, Figure 6.l shows the abbreviated logo of Caterpillar implements, which is why it is referred to in construction as 'cat'. However, the namesake is a very different animal because the founder of the company, Benjamin Holt, was the inventor of the 'track shoe' tractor, so this is where the name 'caterpillar' comes from, since the word in English. Bobcat, on the other hand, depicts an American lynx both in terms of the original meaning of the brand name and in terms of the main motif of the logo (Figure 6.m).

2. 5. Mythological creatures

Creatures in legends, myths and fairy tales always combine the physique of one or more animals with the aim of amplifying or combining some property of real living beings. Such is the griffin, which was considered the lord of all creatures, a symbol of divine power. Armed with the lion's body of the king of animals and the head and wings of the eagle said to be the lord of the air, he becomes the soaring lion that embodies the ascended power. It is believed that the griffin is a kind of dragon hybrid among mythological creatures because it is zoomorphic, because it has animal body.

The dominating effect is further enhanced by the crowned griffin head on the Swedish Saab and Scania logos (Figure 7a-b). The former is the passenger car, and the latter is the name of the truck business, but the main motif of the emblem is absolutely the same. Since the 90's, right-hand drive versions of Opel have been sold under the same model names but under a different brand name, contrary to common automotive practice, due to the owner's GM unique business policy into circulation (Figure 7.c). The formerly independent manufacturer Vauxhall branded a griffin holding a flag with the letter 'V', suggesting that the company's products are treasures like those of these mystical creatures have always guarded. The badge of the German-founded supercar manufacturer Gumpert shows a griffin bird standing on its hind legs in an even more dynamic form, while kicking off for take-off. In their reading, in addition to uniqueness, their cars evoke the unstoppable and power of this mythical creature. According to legends, few people in power and agility can compete with a griffin.



Figure 7 Griffins and dragons

Humanity has a similar attitude towards dragons, which have a huge cult in the Far East. Most of the time, dragon is a positive being with great creative power, which represents both wisdom and protection. It includes all the primal elements, and even, according to some approaches, the dragon is nature itself. It is not surprising that it also appears in the logo of South Korea's oldest car manufacturer, Ssangyong. The brand name itself means twin dragons, and the emblem is a stylized representation of two intertwined dragons rising into the sky (Figure 7.e). A clearer dragon motif can be found on the first two generations of sports cars. Although, according to some car owners, a Viking ship with a dragon mast is modelled on the badge (Figure 7.f). This is contradicted by the fact that we do not know of Viking connections in the history of the Japanese people, but dragons occupy a prominent place in their culture. Figure 7.g shows an emblem with different interpretations, but still more traceable in terms of history. The green creature of the Italian Alfa Romeo badge is a snake in places, a dragon in others, but perhaps the crowned, dragon-headed snake is closest to reality. The misunderstanding is explained by the historical theme on which it was based, since the dragon itself is derived from the coat of arms of the Visconti family, which ruled the city in the 14th century, which has undergone several reinterpretations over time. Perhaps that's why less informed consumers mostly see a monster squirting tongues of flame on the emblem, even though it symbolizes a new man escaping from a dragon's mouth. The manufacturer's connection to Milan is also shown by the symbol of its headquarters, the red cross.

2. 6. Ruminants

Naming this subcategory may seem strange, but that's because the group itself is. We have already met herbivores in the case of horses, where attachment to man, freedom and speed were the main symbols of emblems. For the group of ruminants, this can no longer be said. The animals included here are closer to predators in this approach since they are equally the embodiment of wildness and unbridled strength.



Figure 8 Ruminants, kings of the paths

Figure 8.a shows the emblem previously seen on Dodge cars. Today, RAM products, which became an independent brand with the reorganization of the Chrysler Group in 2010, receive exclusively this ram head symbol. The phrase is expressive for these robust pick-ups. After all, what comes to mind when the king of paths, a ram, comes across? It is to ‘dodge’. Even without words, this is conveyed by the 3D ram head placed on the shield, demanding respect. The same strong dominance is represented by the bulls. The most well-known such car emblem is the enraged golden bull on Lamborghini sports cars, which also seems to be a good choice, since it is precisely this feeling that is expected in the buyers also from an expensive, high-performance vehicle (Figure 8.b). The Italian company originally produced tractors, so from its customers engaged in agriculture, the founder Ferruccio Lamborghini was well aware of the general nature of bulls. The branding, on the other hand, has an image of a specific animal, Murciélago, as this legendary bull survived 24 sword stabbings in a battle in 1879, and thus it became a defining symbol of strength. The motif of the Intermeccanica, which was also founded in Italy but has ties to several nations in terms of history, is currently being used by Meccanica, a Canadian manufacturer of electric mini cars owned and used by a successor company (Figure 8.c). In their marketing communications, this symbolizes pride from the company's tradition. The Spanish are the closest to bullfighting, so it is not surprising that the logo of Tauro, which builds luxury sports cars, also features a silhouette of a bull that has selected its target and is about to attack (Figure 8.d).

In contrast to wild and attacking ruminants, the horned deer symbolizes dignity, majesty and maturity. Possessing important meanings in many cultures, including Hungarian legends, the animal embodies both the periodicity of time and renewal, goodness, maturity or in some places it is masculinity itself, while in the peoples of the East it is synonymous with prosperity and longevity. In Figure 5.g of chapter 2.3, we have already mentioned deer antlers in the case of Porsche, where it is only a reference to the company's headquarters. However, in the case of the Russian automobile plant GAZ (Gorkovskiy Avtomobilny Zavod), it is already the silhouette of a proudly standing deer that gives the main motif of the logo (Figure 8.e). Again, the company applies the power radiating from the animal's enclosure to their Ford's license-based products. Interestingly, the brand name of his

commercial vehicles is GAZelle, which is also the name of an even-toed ungulate animal. But this is not the only species of antelope that has inspired manufacturers. The Chevrolet Impala, with its choice of name and unique emblem shown in Figure 8.f, also suggests the gracefulness, dynamism, and acceleration characteristic of the movement of African impalas.

2. 7. Creepers

The last large group includes all animals that did not fit into any of the previous ones. Most of the time, these creatures are not among people's favourites, but due to some of their properties, they create a feeling of admiration, fear, or curiosity in the observer. It is also worth mentioning here that, for example, an entire category of cars was named after order of spiders that can be classified as arthropods. The name Spider or Spyder, used by manufacturer and sometimes even with different phonetics, is used as the type of designation for lightweight, two-seater, open sports cars. But open-top versions of traditional closed-body sports cars are also often highlighted with this name. The basic idea may come from the fact that the roofs of these vehicles, which come up in bad weather, make these roadsters look like spiders in the eyes of some.

Staying with the official factory emblems, the snake can be mentioned as a recurring motif that appears several times, even though the snake is mostly a negative figure. For example, it symbolizes seduction in the world-wide Christian culture. In connection with this, it became the embodiment of destiny, while in some places snake is the messenger of eternal truth. However, due to the role of snake venom in healing, snakes are also internationally known symbols of wisdom and science.

Figure 9.a provides the first concrete example. The emblem of the Dodge Viper shows the namesake of the sports car, the image of a viper. The family of vipers is a group containing quite a lot of species, with many poisonous versions that are also dangerous to humans. For this reason, the name is known worldwide, so it can be an excellent "advertisement" for a tuned sports car that can also be used on racetracks. Figure 9.b already shows the cobra emblem on the high-performance sports cars of the production cars refurbished by Shelby American. The first job of the company, which is mainly engaged in the production of Ford Motor Company, was AC Cobra. The success of this roadster is shown by the emblem of a cobra with spread neck lobes, which is the most unusual snake in the animal kingdom.

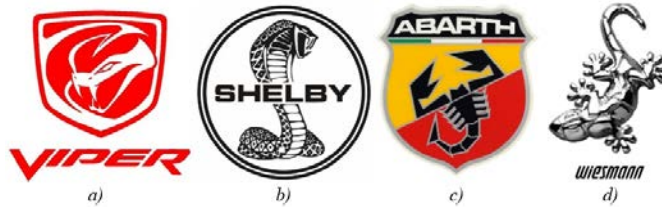


Figure 9 Reptiles and arthropods on car emblems

In addition to snakes, arthropods are also represented on car emblems. Once again, an animal with poison provides the basis for the shield-shaped logo of the company Abarth, which is engaged in Fiat tuning. In addition to the yellow and red colours, the black scorpion, depicted in recognizable detail, also serves to attract even more pronounced attention. A scorpion with a special physique is synonymous with uniqueness and danger. It sends the message that all its body parts are made for fight. The emblem is come from the birth zodiac sign of Karl (later Carlo) Abarth, but the clear marketing interpretation is also not far behind. Abarth cars should be well handled, strong and powerful, but above all they should be small and ‘bad’, like a scorpion.

Finally, a four-legged animal is also represented in this category. The German custom sports car manufacturer Wiesmann consciously chose the gecko as its own symbol. The movement of this family, which can be classified as a suborder of lizards, is well known for its unique adhesion and good manoeuvrability. The manufacturer promises just that. Their commitment is that their cars are able to move extremely fast on any surface, since ‘Wiesmann's cars stick to the road’, so they can be controlled well even at high speeds.

3. SUMMARY

The most important task of brand signs is to convey value. Overall, it can be said that the collective knowledge associated with the figures can be recalled from nature. In most cases, such motifs seem familiar, suggest timelessness, and thus create a sense of reliability. These qualities will always be important aspects in the eyes of customers, so evoking nature is also useful from a marketing point of view, as it helps convey the desired message and improves the memorability of the emblem.

REFERENCES

Automárkák mindent az autókról. (2022, October 15). Retrieved from automarkak.theboard: <http://automarkak.theboard.hu/auto-emblemak/>

-
- Budermann, K., Kim, Y., & Wozniak, C. (2010). *Brand Identity Essentials: 100 Principles for Designing Logos and Building Brands*. Rockport Publishers.
- Dömötör, C., & Péter, J. (2012). Natural principles in analogy-based design. *GÉP*, 63(12), 29-32.
- Heptinstall, S. (2018). *Car Marques: A Graphic Guide to Automotive Logos and Emblems*, Motorbooks. Motorbooks.
- Kuah, I. (2022, October 15). *Official Cizetta USA Website*. Retrieved from cizettaautomobile.com: <https://cizettaautomobile.com/supercar/>
- ListCarBrands*. (2022, October 15). Retrieved from <https://listcarbrands.com/>
- MTI. (2015. október 15). Itt vannak a Komondorok, az új magyar harcjárművek, HVG Publishing House, 2015. October. 14th, EPA-00332. *HVG*. Forrás: https://hvg.hu/itthon/20151014_Itt_a_Komondor_az_uj_magyar_harcjarmu_f
- Négyesi, P. (2011). *Cars Made in Hungary 1945-1990*,. magyarjarmu.hu.
- Orgoványi, G. (2010). *Design és tipográfiai alapok - Tervezőgrafika II*. Centroszet Szakképzés-szervezési Nonprofit Kft. Retrieved from http://centroszet.hu/tananyag/tervgrafika2/tervgraf_2_kotet.pdf
- Wheeler, A. (2009). *Designing Brand Identity*. John Wiley & Sons, Inc.

THE ROLE OF ARTIFICIAL INTELLIGENCE IN THE DEVELOPMENT OF RAILWAY TRANSPORTATION

PÉTER FICZERE

*Budapest University of Technology and Economics
Department of Railway Vehicles and Vehicle Systems Analysis
H-1111 Budapest Műegyetem rkp.3.
ficzere.peter@kjk.bme.hu
<https://orcid.org/0000-0003-3207-5501>*

Abstract: Artificial intelligence (AI) has been a revolutionary force in modern transportation systems. In recent years, AI has played an important role in the development of railway transportation. This paper explores the role of AI in railway transportation and the potential impact it may have on the industry. The paper begins by discussing the different types of AI technologies that are being used in railway transportation. It then examines the advantages of AI in railway transportation, including improved safety, increased efficiency, and reduced costs. Finally, the paper discusses the challenges associated with implementing AI in railway transportation and concludes with a discussion of future developments in this area.

Keywords: *Artificial Intelligence, AI, railway transportation, railway industries, Digital Automatic Coupling (DAC)*

1. INTRODUCTION

Railway transportation is one of the oldest and most important modes of transportation in the world. Over the years, it has played a vital role in the transportation of people and goods, and it continues to be an important part of the transportation system. However, the railway industry is facing many challenges, including increasing competition from other modes of transportation, aging infrastructure, and safety concerns. To address these challenges, the railway industry is turning to artificial intelligence (AI) technologies to improve its operations and provide better service to its customers. AI has the potential to revolutionize railway transportation, and this paper will explore the role of AI in the development of railway transportation.

2. METHODOLOGY

Types of AI technologies used in railway transportation:

There are several types of AI technologies that are being used in railway transportation. One of the most important is machine learning. Machine learning is a type of AI that allows machines to learn from data without being explicitly programmed (Borsodi & Takács, 2022). Machine learning is being used in railway transportation to develop predictive maintenance models, which can help prevent breakdowns and reduce downtime. Another important type of AI technology is computer vision. Computer vision is a type of AI that allows machines to recognize and interpret visual data, such as images and video (Fedorko, 2021). Computer vision is being used in railway transportation to develop intelligent video surveillance systems, which can help improve safety and security (Ulewicz, et al., 2019).

3. RESULTS

3. 1. Advantages of AI in railway transportation

There are several advantages to using AI in railway transportation. One of the most important is improved safety. AI technologies, such as predictive maintenance models and intelligent video surveillance systems, can help identify potential safety hazards and prevent accidents before they occur. Another advantage is increased efficiency. AI technologies can help optimize railway operations, reducing delays and improving service to customers. Additionally, AI can help reduce costs by reducing the need for manual labour and optimizing resource allocation.

AI can support research and development in the railway industry in several ways, including:

- Predictive modelling and simulation: AI can help researchers develop predictive models and simulations that can simulate different scenarios and outcomes. For example, machine learning algorithms can be used to analyse data from railway systems, such as train schedules, traffic patterns, and weather conditions, to predict potential issues and improve the efficiency of railway operations.
- Data analysis and decision-making: AI can help researchers and engineers analyse large amounts of data to make informed decisions. Machine learning algorithms can be used to identify patterns and correlations in the data,

allowing researchers to make predictions and recommendations based on the data.

- Autonomous systems: AI can be used to develop and optimize autonomous systems for railway operations. For example, AI can be used to develop algorithms that allow trains to operate autonomously, reducing the need for human intervention.
- Optimization of resources: AI can be used to optimize the use of resources in railway operations. Machine learning algorithms can be used to analyse data on train schedules, maintenance schedules, and other operational data to identify areas where resources can be optimized, such as reducing downtime or increasing efficiency.
- Risk management: AI can help researchers and engineers identify potential risks in railway operations and develop strategies to mitigate them. For example, machine learning algorithms can be used to analyse data on train accidents and incidents to identify patterns and potential risks.

Overall, AI can be a valuable tool for supporting research and development in the railway industry, helping to improve efficiency, safety, and reliability in railway operations.

3. 2. Digital Automatic Coupling (DAC)

It is important to note, however, that one of the most important steps to properly exploit the new opportunities is digital transformation. An essential element of this is the implementation of digital automatic coupling devices on wagons.

Digital Automatic Coupling (DAC) technology can improve the efficiency of railway transportation in several ways:

- Faster and more efficient coupling: DAC technology allows for faster and more efficient coupling and decoupling of train cars. This can reduce the time required for loading and unloading cargo and improve the overall efficiency of railway operations.
- Improved safety: DAC technology can improve safety by providing more accurate and up-to-date information about train car positions and movements. This can help reduce the risk of collisions and other accidents (Takács, 2023), (Mekonnen, et al., 2023).
- Real-time monitoring: DAC technology can allow for real-time monitoring of train car positions and movements, allowing control centres to make more informed decisions about train schedules, routes, and other operational details. This can help reduce delays and improve the overall efficiency of railway operations.

-
- Increased capacity: DAC technology can increase the capacity of train cars by allowing for more precise coupling and decoupling. This can help reduce the number of train cars required to transport a given amount of cargo, improving efficiency, and reducing costs.
 - Improved maintenance: DAC technology can improve maintenance operations by providing real-time information about train car components and performance. This can help maintenance teams identify potential issues and make repairs more quickly, reducing downtime and improving efficiency.

Overall, DAC technology can help improve the efficiency, safety, and reliability of railway transportation by providing faster and more efficient coupling, real-time monitoring, and more accurate information about train car positions and movements.

However, while there are clear benefits to be gained from the uptake of DAC, it may not be widely adopted in the near future. The cause is that rail transport is fragmented. Separate departments are responsible for traction, passenger transport, the carriage of goods and infrastructure management. As these outsourced companies are economically independent, there is no collective interest. Passenger and cargo wagons would have to be installed with DAC equipment, so the costs would logically be assigned to these divisions. But the profit is expected to be made by the infrastructure provider. It is reasonable that the companies that operate and service the wagons do not want to spend around 20.000 EUR per wagon, as they will never make a profit for them. At the same time, the company that maintains and handles the infrastructure does not want to spend on upgrading wagons owned by another company.

Another difficulty is that the profitability of old cargo wagons is very uncertain. To solve the problem, companies in each area need to work together, but none of them are interested in doing it separately. But its social utility is unquestionable, so top-down legislation can provide the solution.

It is important to note that this investment makes no sense in small increments, and the benefits can only be realised if everyone switches to the new systems at approximately the same time. Of course, this is most important in terms of international traffic.

It is also important that a standardized coupling device is introduced.

In the same way as the economic benefits (Evans, 2013), we can also see that this is the only way to maximise the potential of artificial intelligence.

The resulting increase in capacity could also significantly reduce the volume of passenger and cargo traffic on the roads, which would also lead to a reduction in emissions (Török & Sipos, 2022).

While digitalization has the potential to bring many benefits to railway transportation, there are also some potential threats that need to be addressed. Here are some of the key threats of digitalization in rail transport (Török, 2023):

- Cybersecurity risks: As railway systems become more interconnected and reliant on digital technology, they may become more vulnerable to cyber-attacks. This could include attacks on the railway's IT systems, control systems, or even the trains themselves. Cybersecurity threats could disrupt railway operations, compromise passenger safety, and cause significant financial losses.
- Reliance on technology: While digitalization can improve the efficiency and reliability of railway services, it also means that railway operators become more reliant on technology. This means that if there is a technology failure, there could be significant disruptions to railway operations.
- Job displacement: The use of digital technology could lead to job displacement in the railway industry, as automation and AI take over some roles that were previously done by humans. This could have a significant impact on workers and their communities.
- Data privacy concerns: As digitalization generates large amounts of data about railway passengers and operations, there are concerns about how this data is collected, stored, and used. There is a risk that this data could be misused or hacked, leading to privacy violations and other negative consequences.
- Infrastructure challenges: Digitalization requires significant investments in IT infrastructure and communication networks, which can be expensive and time-consuming to implement. Railway operators may need to upgrade their infrastructure to support digitalization, which could lead to disruptions during the implementation phase.

It is therefore important to recognize the potential threats of digitalization in rail transport and take steps to mitigate them. This includes investing in cybersecurity, ensuring appropriate training and support for workers, addressing privacy concerns, and carefully managing the implementation of new digital technologies.

3. 3. Challenges associated with implementing AI in railway transportation

Despite the many advantages of AI in railway transportation, there are also several challenges associated with its implementation. One of the biggest challenges is the cost of implementing AI technologies. Implementing AI requires significant investment in hardware, software, and personnel. Another challenge is the lack of standardization in the industry. There is a need for standardized data formats and communication protocols to enable the integration of different AI systems.

Finally, there are also concerns around privacy and security. Intelligent video surveillance systems, for example, raise concerns about the use of personal data and the potential for abuse.

4. CONCLUSION

In conclusion, AI is playing an increasingly important role in the development of railway transportation. The advantages of AI, including improved safety, increased efficiency, and reduced costs, make it a promising technology.

4. 1. Future developments in AI in railway transportation

Despite the challenges, the future of AI in railway transportation is promising. AI technologies are expected to continue to play an important role in the development of railway transportation, with new technologies and applications emerging over time. One area of particular interest is the use of AI in autonomous trains. Autonomous trains have the potential to revolutionize railway transportation, improving safety and efficiency while reducing costs. Another area of interest is the use of AI in customer service, with chatbots and virtual assistants being developed to improve the customer experience.

5. SUMMARY

Railway transportation has been a vital mode of transportation for both people and goods for many years, but it faces numerous challenges such as competition from other modes of transportation, aging infrastructure, and safety concerns. Artificial intelligence (AI) technologies have the potential to revolutionize railway transportation by improving efficiency, reducing costs, and increasing safety. Machine learning and computer vision are some of the AI technologies used in railway transportation. AI can support research and development in the railway industry in several ways, including developing predictive models and simulations, analysing data, developing autonomous systems, optimizing resources, and risk management. Digital automatic coupling (DAC) technology can further improve the efficiency of railway transportation by providing faster and more efficient coupling, improved safety, real-time monitoring, and increased capacity. However, the fragmentation of the railway industry may limit the adoption of DAC technology in the near future.

REFERENCES

- Borsodi, E. & Takács, Á., 2022. Generative Design: An Overview and Its Relation-ship to Artificial Intelligence. *Design of Machines and Structures*, 12(2), pp. 54-60.
- Evans, A. W., 2013. The economics of railway safety. *Research in Transportation Economics*, 43(1), pp. 137-147.
- Fedorko, G., 2021. Application possibilities of virtual reality in failure analysis of conveyor belts. *Engineering Failure Analysis*, Volume 128, p. 105615.
- Mekonnen, A. A., Sipos, T. & Szabó, Z., 2023. Generalized Linear Modeling of Crashes on Urban Road Links. *Periodica Polytechnica Transportation Engineering*, 51(2), pp. 140-146.
- Takács, Á., 2023. *Safe In and Out of the Car*. s.l., Springer Cham..
- Török, Á., 2023. Do Automated Vehicles Reduce the Risk of Crashes—Dream or Reality?. *IEEE Transactions on Intelligent Transportation Systems*, 24(1), pp. 718-727.
- Török, Á. & Sipos, T., 2022. Can the Marginal Cost Be Extended to Life Cycle Cost? A Theoretical Case Study for Transport. *International Journal for Traffic and Transport Engineering*, 12(2), pp. 170-175.
- Ulewicz, R., Nový, F., Novák, P. & Palček, P., 2019. The investigation of the fatigue failure of passenger carriage draw-hook. *Engineering Failure Analysis*, Volume 104, pp. 609-616.

PREDICTION OF STRAIN DISTRIBUTION DURING THE PLANE STRAIN TENSILE TEST BASED ON ARTIFICIAL NEURAL NETWORKS

RAID FEKHREDDINE MEKNASSI¹, GÁBOR BÉRES², ZSOLT LUKÁCS³

¹*University of Miskolc, Department of Mechanical Technologies,
3515, Miskolc-Egyetemváros,
metraid@uni-miskolc.hu*

²*John von Neumann University, GAMF Faculty of Engineering and Computer Science, 6000,
Kecskemét, Izsáki út 10,
beres.gabor@gamf.uni-neumann.hu*

³*University of Miskolc, Department of Mechanical Technologies,
3515 Miskolc, Miskolc-Egyetemváros,
zsolt.lukacs@uni-miskolc.hu*

²<https://orcid.org/0000-0002-1496-5618>, ³<https://orcid.org/0000-0002-6517-8382>

Abstract: In this study, finite element method was used to study the effects of various notch geometries on the strain field distributions during the plane strain tensile test for cold-rolled steel (DC01). The artificial neural network approach (ANN) and the response surface methodology (RSM) were adopted to develop the mathematical prediction models applied in the optimization procedure. The strain state was expressed by self-defined metrics, namely, the Plane Strain State Index (PSSI) and the Homogeneity Index (HI) were predicted by changing the notch angle (X degree), notch width (d mm), and notch length (c mm). The Quadratic mathematical models obtained by the RSM, and ANN presented the evolution of PSSI, and HI based on (X , d , and c). The results show that the ANN method provides more precise results compared to those of the RSM approach.

Keywords: *FEM, ANN, RSM, Tensile test, Plan strain*

1. INTRODUCTION

Predicting the formability and safety limit of material in sheet metal forming operations depends on accurate knowledge of forming behaviour under various strain states. The forming limit diagram (FLD) developed by Keeler (Keeler & Backofen, 1964) and Goodwin (Goodwin & Gorton, 1968) is a beneficial graphical tool for predicting the plastic behaviour of sheet metal, used in FEM analysis

and quality optimization during production. Usually, the FLD can be determined by the Nakajima and Marciniak stretch-forming test according to the ISO 12004-2:2008 standard (Marciniak & Kuczyński, 1967), (International Organization for Standardization, 2008). The strain domain must be covered from equibiaxial tension ($\epsilon_1 = \epsilon_2$) to pure shear ($\epsilon_1 = -\epsilon_2$). Also, it is necessary to deform the specimen along a linear strain path during the different loading patterns. However, the strain path is a broken line in the actual industry. Because, unlike the laboratory simulation, there are complex tool geometries and multi-stage forming operations for industrial sheet metal forming processes that require several passes, which means that the deformation patterns change from one pass to another.

A pre-strained plane specimen with tensile test could be an interesting alternative to determine and predict forming limit curves with non-linear path. Many authors intensively used plane strain tensile test specimens for various mechanical characterizations (Flores, et al., 2010), (Kuwabara, 2007), (An, Vegter, & Elliott, 2004). In our study, we intended to predict and optimize a sample geometry for the plane strain tensile test that could allow us to apply further deformation tests, which eventually leads to determining the forming limits on non-linear strain paths. Several sample geometries were investigated through simulation on ABAQUS to study and measure the different strain behaviour during the test. Firstly, we investigate the evolution of the plane strain distribution, which is characterized by the self-defined change of the plane strain state index (PSSI) and homogeneity index (HI) as a function of the specimen notch parameters: notch angle (X degree), notch width (d mm), notch length (c mm). Secondly, modelling the specimen notch parameters using the response surface methodology (RSM) and the artificial neural network (ANN) methods is carried out. Finally, the predictive capabilities of the ANN and RSM models were further compared in terms of their mean square error (RMSE), and coefficient of determination (R2).

2. MATERIAL AND SAMPLE GEOMETRY

In the present work we considered a nominal 1 mm thick, cold rolled steel (DC01). Mechanical properties parallel, perpendicular and 45° to the rolling direction are given in Table 1. The plane strain tensile tests were performed by a geometry shown in Figure 1 (Wagoner, 1980). It was considered as the basic shape, on which subsequent improvements are proposed in this paper.

Where: A_{80} is the total engineering strain, A_{80_ave} is the average total engineering strain, r is the r-value, $r = \frac{(r_0+r_{90}+2.r_{45})}{4}$ is the normal anisotropy, $\Delta r = \frac{r_0+r_{90}}{2} - r_{45}$ is the planar anisotropy, $R_{p0.2}$ is the yield strength, $R_{p0.2_ave}$ is the

average yield strength, R_m is the tensile strength and R_{m_avr} is the average tensile strength.

Table 1
Data for the yield and strength parameters of DC01 material

Orientation angle	0°	45°	90°
A80 (%)	40.0	36.0	39.0
A80_ave (%)	38.0		
r	2.35	1.55	2.52
\bar{r}	1.99		
Δr	0.88		
Rp0,2 (N/mm ²)	199	206	198
Rp0,2_ave (N/mm ²)	201		
Rm (N/mm ²)	306	322	298
Rm_ave (N/mm ²)	309		

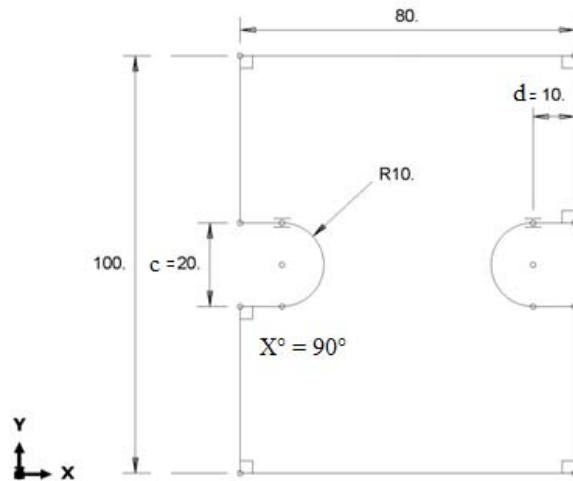


Figure 1 Sample geometry, used in the plane strain tensile test simulation (units in mm)

3. FINITE ELEMENT MODELLING

The code used for simulation is Abaqus 2021, with Hill yield criterion developed by Hill in 1948 ((1), written in terms of the Lankford coefficients (r)). In order to calculate the plastic stress-strain behaviour of the investigated materials, the Swift

non-linear isotropic hardening model, shown in equation (2), was used with our measured data shown in Table 2.

All specimens have a 30 mm gripping area length on both sides and 0.8 mm mesh size of a three-dimensional eight-node brick element with six integration points is used. The boundary and loading conditions are applied in a manner that is as similar to the real tensile test experiment as possible. The lower grip of the specimen was kept fixed in all directions but free in the direction of the applied load. The sliding between grips and specimen is neglected. The maximum major and minor strain values are extracted in the strain hardening region before the local cross-sectional area becomes significantly smaller than the average (necking region). The data gathered from nine points in the middle area of all samples were, as shown in Figure 2.

$$\Phi(\sigma) = \frac{r_{TD}(r_{RD} + 1)\sigma_{11}^2 + r_{RD}(r_{TD} + 1)\sigma_{22}^2 - 2r_{RD}r_{TD}\sigma_{11}\sigma_{22} + (r_{RD} + r_{TD})(2r_{45^\circ} + 1)\sigma_{11}^2}{r_{TD}(r_{RD} + 1)} - \bar{\sigma} \quad (1)$$

$$= 0$$

$$\bar{\sigma} = K(\varphi_0 + \bar{\varphi})^n \quad (2)$$

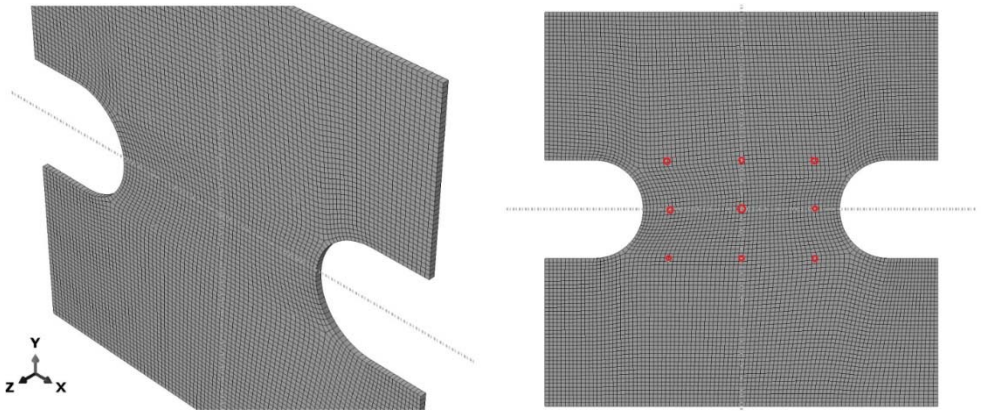


Figure 2 Mesh and data points of the standard geometry

Table 2
Swift equation data for the used materials

Material	Swift equation		
	K [MPa]	φ_0 [-]	n [-]
DC01	578	0.0173	0.22

In (1) and (2), $\bar{\sigma}$, $\bar{\varphi}$, are respectively the current yield stress and anisotropic equivalent plastic strain, TD refers to the transverse and RD to the rolling direction. Hardening is defined by the material parameters K , n and φ_0 and those are nominated in Table 2.

4. TESTING METHODS

To study the effect of various notch geometries (X , d , C) on the strain field distributions, the L27 (313) Taguchi standard orthogonal array is adopted as the testing method. The factors and their levels in the present study are presented in Table 3.

Table 3
Orthogonal array for responses and their levels

X (degree)	d (mm)	c (mm)	PSSI min	HI min
90	2.5	15	-0.1203	0.4168
		20	-0.0974	0.3175
		25	-0.0959	0.2898
	5	15	-0.0914	0.3811
		20	-0.0847	0.2304
		25	-0.0838	0.2057
	10	15	-0.0929	0.3350
		20	-0.0719	0.2168
		25	-0.0435	0.1602
95	2.5	15	-0.1329	0.7350
		20	-0.1018	0.3715
		25	-0.0996	0.2930
	5	15	-0.1133	0.4453
		20	-0.1018	0.3715
		25	-0.0999	0.2630
	10	15	-0.0936	0.3570
		20	-0.0899	0.2476
		25	-0.0633	0.1914
100	2.5	15	-0.2435	0.9350
		20	-0.2235	0.7239
		25	-0.1986	0.4930
	5	15	-0.2345	0.7435
		20	-0.2105	0.4684
		25	-0.1850	0.3326
	10	15	-0.1532	0.5138
		20	-0.1403	0.5021
		25	-0.0995	0.2923

For characterizing the strain state, we used the following equations:

Plane strain state index (PSSI): the closer the average minor strain (ϵ_2) to zero, the better it is.

$$PSSI = A_{\epsilon_2} = \frac{\sum_{i=1}^n \epsilon_2}{n} \quad (n = 1 \dots 9) \quad (3)$$

Homogeneity index (HI) (equivalent with standard deviation): the smaller the HI, the better is the result.

$$HI = \sqrt{\frac{\sum_{i=1}^n (\epsilon_1^n - A_{\epsilon_1})^2}{n}} \quad (n = 1 \dots 9) \quad (4)$$

5. MODELLING BY RESPONSE SURFACE METHODOLOGY

The relationship between the factors and the output parameters was modelled by quadratic regression. The regression equations obtained are given below by (5), and (6) with coefficients of determination R² of 96.34%, and 94.38%, respectively. These regression models help predict the response parameters with respect to the input control parameters.

$$PSSI \text{ min} = -11.95 + 0.27 X - 0.0187 C + 0.000814 X d + 0.000222 X C + 0.000177 d C - 0.001507 X^2 + 0.000414 d^2 - 0.000002 C^2 \quad (5)$$

$$HI \text{ min} = 14.45 - 0.346 X + 0.0792 d + 0.1089 C - 0.002150 X d - 0.001991 X C + 0.001908 d C + 0.002238 X^2 + 0.00487 d^2 + 0.001076 C^2 \quad (6)$$

6. MODELLING BY ARTIFICIAL NEURAL NETWORK

The purpose of applying this artificial intelligent (AI)-based method is because of their ability to model the highly nonlinear processes. A neural network consists of a directed weighted graph whose nodes symbolize neurons; these neurons have an activation function to influence other network neurons (Chabbi, et al., 2017). We used JMP Pro predictive analytics software, it provides advanced algorithms for building, assessing and managing predictive models.

The test design consists of 27 tests; among them, 18 tests are used for learning the network and 9 are arbitrarily chosen for validating the network. The neural network learning is made by backpropagation algorithm, which is based on the gradient-descent method.

Several network structures were tested for both PSSI and HI. According to the correlation coefficient R² and the root-mean-square error (RMSE) for both learning and validation sets, the adopted structures are shown in Table 4.

Table 4
ANN structures of PSSI and HI

Response	Nodes number Input-hidden-output	Learning		Validation	
		R2	RMSE	R2	RMSE
PSSI	3-4-1	0.9964	0.0029	0.9805	0.0087
HI	3-6-1	0.9824	0.0026	0.9723	0.0048

The comparison between RSM and ANN showed that, the values of R2 of the ANN models are better. That's proves the robustness and the reliability of the ANN method. The ANN models are expressed as follows:

$$\text{PSSI min} = -0.1525 - 0.0002 H1 + 0.0231 H2 + 0.0578 H3 + 0.0253 H4 \quad (7)$$

where

$$\begin{aligned} H1 &= \tanh (5 (0.577 X - 0.4556 d - 0.3363 C - 44.7319)); \\ H2 &= \tanh (5 (-0.06 X - 0.4034 d + 0.5728 C - 3.3808)); \\ H3 &= \tanh (5 (-1.4098 X - 0.438 d + 0.1278 C + 134.5717)); \\ H4 &= \tanh (5 (-0.2553 X + 0.9046 d - 0.2511 C + 23.7027)); \end{aligned}$$

$$\text{HI min} = 1.6204 - 2.8529 H1 + 2.7680 H2 + 2.0635 H3 - 0.3214 H4 - 0.5363 H5 - 0.7615 H6 \quad (8)$$

where

$$\begin{aligned} H1 &= \tanh (5 (-0.1081 X + 0.0981 d + 0.0387 C + 9.3979)); \\ H2 &= \tanh (5 (-0.0633 X + 0.2012 d + 0.0607 C + 3.4180)); \\ H3 &= \tanh (5 (-0.0638 X - 0.1956 d - 0.0110 C + 7.1946)); \\ H4 &= \tanh (5 (0.0135 X + 0.0541 d + 0.0015 C - 1.6519)); \\ H5 &= \tanh (5 (-0.011 X - 0.0291 d + 0.0097 C + 1.1673)); \\ H6 &= \tanh (5 (-0.0662 X - 0.0761 d + 0.1098 C + 4.7903)); \end{aligned}$$

where HI are the terms represent the output of the hidden layer.

The previous models can predict plane strain state index (PSSI) and homogeneity index (HI) in the range of selected sample geometries. Figures 3 illustrate the differences between the modelled and predicted responses of HI and PSSI. These figures indicate that the models can represent the system under the given studied domain.

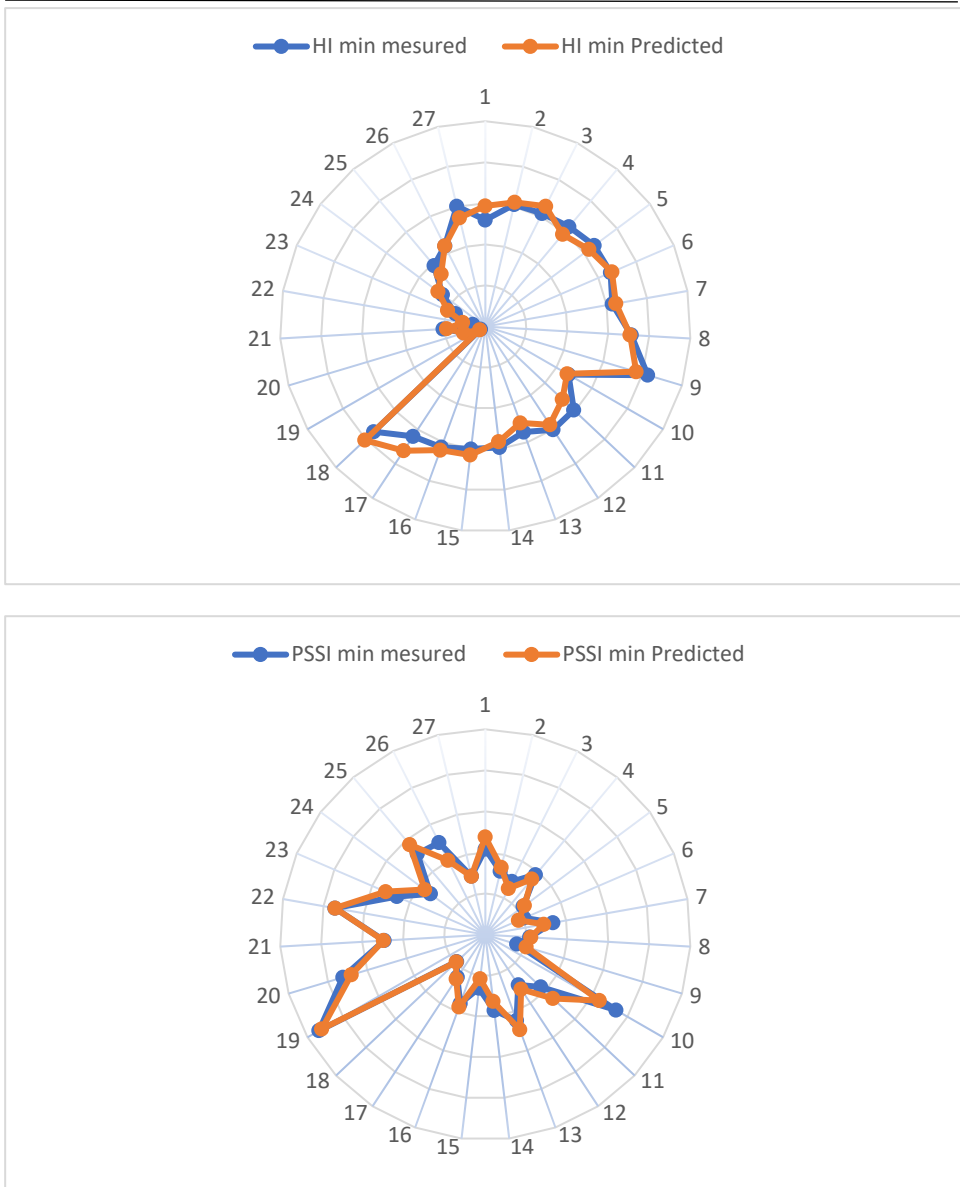


Figure 3 Comparison of the modelled and predicted ANN method values for PSSI and HI

7. SUMMARY

In our study, the prediction of strain distribution during the plane strain tensile test using the response surface methodology (RSM) and the artificial neural network (ANN) methods is carried out. The comparison between the two modelling methods showed that ANN is better with the values of R². The comparison of the measured and predicted ANN method values for PSSI and HI figures indicates that the models can represent the system under the given studied domain.

REFERENCES

- An, Y. G., Vegter, H., & Elliott, L. (2004). A novel and simple method for the measurement of plane strain work hardening. *Journal of Materials Processing Technology*, 155-156, 1616-1622. doi:<https://doi.org/10.1016/j.jmatprotec.2004.04.344>
- Chabbi, A., Yallese, M. A., Nouioua, M., Meddour, I., Mabrouki, T., & Girardin, F. (2017). Modeling and optimization of turning process parameters during the cutting of polymer (POM C) based on RSM, ANN, and DF methods. *The International Journal of Advanced Manufacturing Technology*, 91, 2267-2290. doi:<https://doi.org/10.1007/s00170-016-9858-8>
- Flores, P., Tuninetti, V., Gilles, G., Gonry, P., Duchêne, L., & Habraken, A. M. (2010). Accurate stress computation in plane strain tensile tests for sheet metal using experimental data. *Journal of Materials Processing Technology*, 210(13), 1772-1779. doi:<https://doi.org/10.1016/j.jmatprotec.2010.06.008>
- Goodwin, G., & Gorton, M. (1968). Application of strain analysis to sheet metal form-ing problems in the press shop. *SAE Technical Paper*.
- International Organization for Standardization. (2008). ISO/DIS 12004-2: 2008. Metallic Materials–Sheet and Strip. *Determination of Forming Limit Curves–Part 2: Deformation of Forming limit Curves in the Laboratory*. International Organization for Standardization.
- Keeler, S., & Backofen, W. (1964). Plastic instability in sheet stretched over rigid punches. *ASM Transactions Quarterly*, 11, 25-48.
- Kuwabara, T. (2007). Advances in experiments on metal sheets and tubes in support of constitutive modeling and forming simulations. *International Journal of Plasticity*, 23(3), 385-419. doi:<https://doi.org/10.1016/j.ijplas.2006.06.003>

Marciniak, Z., & Kuczyński, K. (1967). Limit strains in the processes of stretch-forming sheet metal. *International journal of mechanical sciences* 9.9. *International Journal of Mechanical Sciences*, 9(9), 609-620. doi:[https://doi.org/10.1016/0020-7403\(67\)90066-5](https://doi.org/10.1016/0020-7403(67)90066-5)

Wagoner, R. H. (1980). Measurement and analysis of plane-strain work hardening. *Metallurgical Transactions A*, 11(1), 165-175. doi:<https://doi.org/10.1007/BF02700453>

Design of Machines and Structures, Vol. 13, No. 1 (2023), pp. 84–102.
<https://doi.org/10.32972/dms.2023.007>

DESIGN AND DEVELOPMENT OF A TABLE MOUNTED MANUAL
SEED CRACKING MACHINE FOR A HARD SEED
(DEOCLA REFLEXA HOOK F)

OLAKUNLE OLUKAYODE¹- WASIU ADEDEJI²- KEHINDE OYEWOLE³-
MUSIBA DEEN IDRIS⁴

^{1,2,4}*Osun State University, Department of Mechanical Engineering,
PMB 4494, Osogbo, Nigeria*

¹*olakunle.kayode@uniosun.edu.ng, ²wasiu.adedeji@uniosun.edu.ng,*

⁴*musibadeen.idris@uniosun.edu.ng*

³*Osun State University, Department of Chemical Engineering,
PMB 4494, Osogbo, Nigeria*

³*kehinde.fayemiwo@uniosun.edu.ng,*

<https://orcid.org/0000-0002-9182-3621> (Olukayode O)

Abstract: *Dioclea reflexa* seed is a non-conventional seed widely used in the south-eastern Nigeria for culinary and herbal purposes. In using it for these purposes, cracking of the seed to expose the cotyledon is a necessity. However, the seed is seen as one of the hard seeds difficult to crack manually. This work hereby presents the conceptual solution and the fabricated prototype of the manually operated machine to efficiently and safely crack the seed. The design concept involved pushing the seed into a converging passage-way with the attendant reaction of the narrowing space-seed interface developing a force that will eventually crack the seed. The machine developed, which also serves as a proof of the concept was fabricated from mild steel using established methods of metal fabrication. The machine prototype was evaluated for seed cracking efficiency as well as the perceived ease of use by operators. Results shows that the machine achieved 96% cracking efficiency and the average response of the test subjects invited to operate the machine was that it is easy to operate.

Keywords: *Dioclea reflexa seed, seed cracking machine, Agbaarin, Ukpo, cracking force, seed deformation rupture*

1. INTRODUCTION

Dioclea reflexa seed is known by several vernacular names across the globe. Some of them are Marble vine, Sea purse, Agbaarin (Yoruba language), Ufor or Ukpo (Igbo), and Bonkele (Lingala) (Olukayode, Alade, & Oyelami, 2022), (Ajatta, et al., 2019), (Ajayi, 2014). Its full botanical name is *Dioclea reflexa* Hook F. The seed's natural habitat is the tropical region of the Caribbean, South America, and the West Africa. Researches related to the seed had demonstrated its pharmaceutical, industrial, and dietary usefulness (Ajatta, et al., 2019), (Ajayi, 2014), (Mbah, et al., 2022). The seeds are widely used in the southeast of Nigeria for culinary purposes as food thickener and as a raw material for traditional herbal medicine (Ajatta, et al., 2019), (Ajayi, 2014), (Mbah, et al., 2022). It is regarded as a hard seed to crack. Processing the seeds for domestic use usually involved the need to crack the seed in order to access the cotyledon. The common method of doing this is to manually crush the seed in between two stones. This is tiring and dangerous, hence the need to have a seed cracking machine purposely design for cracking the seed in a safe and less tasking manner.

2. ENGINEERING PROPERTIES OF DIOCLEA REFLEXA SEED

Designing the seed cracking machine involved the determination of some physical and mechanical properties of the seed. The physical properties of interest for the seed in this design are seed linear dimensions (length, width, and thickness), sphericity value ϕ , and geometric mean diameter D_g . The required mechanical properties are seed cracking force, deformation of seed up to cracking point, as well as the coefficient of friction between the seed and the machine processing surfaces. The linear dimensions of the seed are as depicted in Figure 1. Mean values of L, W, T, D_g , and ϕ had been reported by (Olukayode, Alade, & Oyelami, 2022) and are as reproduced in Table 1.

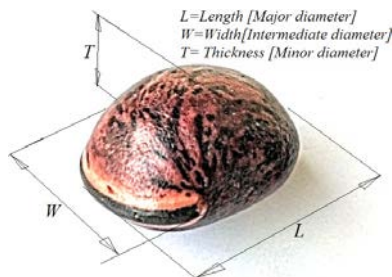


Figure 1. *Dioclea reflexa* seed and its linear dimensions

Table 1
Physical properties of Dioclea reflexa seeds†
(Olukayode, Alade, & Oyelami, 2022)

Physical properties	Moisture content (% wet bases) γ			
	4.8	7.2	9.5	12.1
Length, mm	31.01 (1.45)*	31.45 (1.34)	31.77 (1.54)	32.11 (2.17)
Width, mm	26.64 (1.24)	26.85 (0.83)	27.68 (1.36)	27.74(1.93)
Thickness, mm	21.75 (0.89)	21.7 (1.07)	21.395 (1.13)	21.21 (1.30)
Geometric mean diameter, mm	26.18(0.88)	26.36(0.80)	26.58(1.01)	26.62(1.45)
Sphericity, %	84.41(2.10)	83.93(2.69)	84.01 (3.14)	83.11(2.13)

† Measurement was made with 20 replicates. *Numbers in parenthesis are standard deviations. γ Representing the percentage by weight of water content of the seed.

Table 2
Value of cracking forces and deformation to rupture for the three orientations on the universal testing machine

Seed No.	1	2	3	4	5	6	7	8	9	10	Mean
Axis along L											
Cracking force (kN)	1.25	1.50	1.45	1.60	1.55	1.26	1.55	1.60	1.15	1.15	1.41
Deformation (mm)	2.4	2.6	3.2	3.1	3.5	3.0	3.1	3.0	2.8	3.5	3.0
Length L, (mm)	31.0	30.2	31.1	29.1	31.4	30.0	33.2	33.8	29.1	29.4	30.8
Axis along W											
Cracking force (kN)	1.35	0.85	1.33	0.70	0.80	1.24	1.15	0.90	0.55	0.95	0.98
Deformation (mm)	1.5	1.5	1.5	0.7	1	1.5	3.5	0.8	0.7	2	1.5
Width W (mm)	26.1	26.7	26.8	26.6	29.5	27.1	25.6	29.0	25.5	24.2	26.7
Axis along T											
Cracking force (kN)	0.80	1.00	1.40	1.20	0.95	0.80	0.90	0.45	1.20	0.70	0.94
Deformation (mm)	0.7	0.7	1.0	0.8	0.8	0.9	1.1	1.1	1.3	0.8	0.9
Thickness T (mm)	19.5	19.4	22.3	22.6	19.9	20.4	19.3	20.3	18.4	19.2	20.1

Though (Olukayode, Alade, & Oyelami, 2022) also investigated the rupture (cracking) force of the seed under various moisture contents, seed deformation up to rupture point was not reported. Also, there is no information on the coefficient of friction between the seed and metal surfaces of interest in their work or elsewhere in literature. Hence, there is a need to find the values for these parameters. The material chosen for the fabrication of the manual seed cracking machine was mild steel. Coefficient of friction (μ) between *Dioclea reflexa* seed and mild steel surface was determined using method described by (Fayed, El-Shal M.S., & Omar, 2020). The experiment was repeated five times and the mean value of μ was found to be 0.360. To determine the cracking force and deformation up to seed rupture, the method described by (Olukayode, Alade, & Oyelami, 2022) was used for 10 seeds at 5.6% moisture content (wet basis) for each axis of compression along the length (L), width (T), and thickness (T) axes. Before compression, the seed linear dimension in the orientation of interest was measured using a digital vernier calliper and recorded. The results obtained are detailed in Table 2.

3. DESIGN CONCEPT

The seed cracking machine was designed using the general procedure for machine design as outlined by (Kayode, Adeleke, & Alade, 2020). The cracker was conceived as consisting of a solid smaller cylinder (A) with centre a and radius R_a rotating inside a hollow bigger cylinder (B) with centre b and radius R_b . The centres are non-centric (Figure 2 a) and are referenced to a fixed outside point O. The solid smaller cylinder has a vane parallel to its axis. The seed, modelled as a sphere (C) with diameter d, is first put in the bigger space between the cylinders and then nudged towards the narrower space between the two cylinders by the vane when cylinder A is rotated in the anti-clockwise direction. The two cylinders are assumed to be non-deformable (rigid) and only the seed is deformable. The space separating the two cylinders constituted the machine's cracking chamber.

As the seed is pushed deeper by the vane into the narrowing space under force (P_n) due to torque (T), forces of reaction between the seed and the two adjacent cylindrical surfaces continue to build up until it reaches the cracking force value for the seed. At this point, the seed will no longer be able to sustain deformity in order to conform to the narrowing space and cracking of its shell will ensue. Necessity required that there must be an exit point for the seed to leave the chamber once it is cracked, and there must be an entry point to allow fresh seed to enter the chamber.

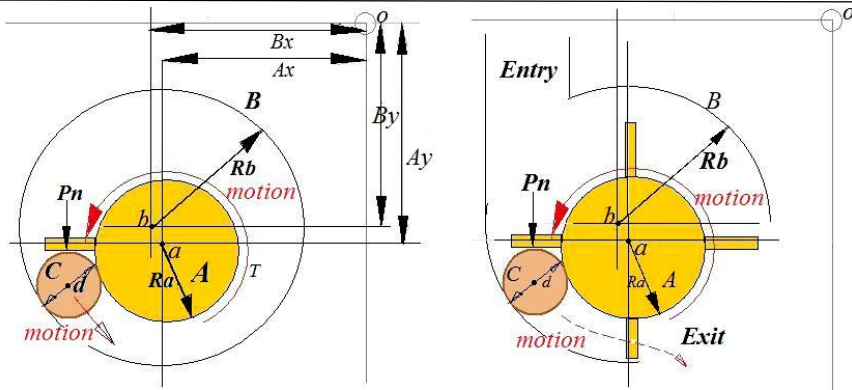


Figure 2 a. Initial design concept **Figure 2 b.** Final design concept

Moreover, a single vane will not be efficient to continuously feed in fresh seeds and expel the cracked ones; hence multiple vanes are to be incorporated to the smaller cylinder. The vanes are spaced in such a way that each space between a vane and the next will only accommodate a single seed. The final conceptual configuration for the seed cracking machine is as depicted in (Figure 2 b). Modelling the seed as a sphere is justified due to the high degree of sphericity of *Dioclea reflexa* seeds at average value of 84% (0.84) (Table 1). Sphericity is the measure of the degree of roundness of the seed. The shape with the maximum value of sphericity is the sphere with a sphericity value of 1.

4. DESIGN ANALYSIS

Referring to Figure 3, the forces acting on the seed are as depicted. The geometry of the cylinders and vane arrangements are such that at the beginning of cracking process, the seed will have three points of contact among the two cylinders surfaces and the vane, with the vane in horizontal position at the beginning of the cracking process. From the diagram (Figure 3), line /ns1/ and /ms1/ are tangential lines through points of contacts between the sphere (the seed), the inner cylinder (A) and the outer cylinder (B) curved surfaces respectively. Resolving forces parallel and normal to bisecting line /S1S2/ of angle (2y) formed by the two tangential lines, P_n is the normal force exerted by the vane (D) on the sphere C, F_c is the force of the outer cylinder on the sphere and F_e is the force of the inner cylinder on the sphere. f_{uc} and f_{ue} are frictional forces between the sphere and the cylinders.

For parallel resolution of forces with reference to line /S1S2/:

$$Pn \cos B - F_c \cos a - F_E \cos a - f_{uc} \cos y - f_{ue} \cos y = 0 \quad (1)$$

(Equilibrium condition)

But $f_{uc} = \mu F_c$ and $f_{ue} = \mu F_E$, μ is the coefficient of friction.

$$Pn \cos B - \cos a(F_c + F_E) - \mu \cos y(F_c + F_E) = 0 \quad (2)$$

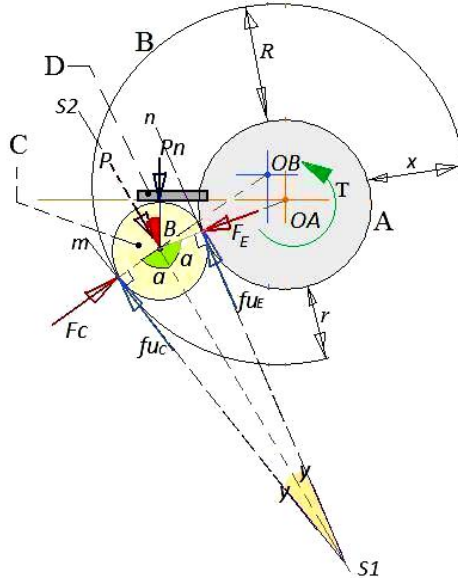


Figure 3 Force Diagram

$$Pn \cos B = (F_c + F_E)(\cos a + \mu \cos y) \quad (3)$$

Note that $Pn \cos B = P$, the component force of Pn forcing the sphere further into the narrowing space.

For normal resolution of forces with reference to line /S1-S2/:

$$Pn \sin B + F_E \sin a - F_c \sin a + f_{uc} \sin y - f_{ue} \sin y = 0 \quad (4)$$

(Equilibrium condition)

$$Pn \sin B - \sin a (F_c - F_E) + \mu \sin y (F_c - F_E) = 0 \quad (5)$$

$$Pn \sin B = (F_c - F_E)(\sin a - \mu \sin y) \quad (6)$$

Divide (6) by (3):

$$\left(\frac{F_c + F_E}{F_c - F_E} \right) = \left(\frac{(\sin a - \mu \sin y)}{(\cos a + \mu \cos y)} \right) \left(\frac{1}{\tan B} \right) \quad (7)$$

Referring to Figure 3 again, R (the widest distance between the two cylinders) is defined by the expression:

$$L < R < 2T \quad (8)$$

where L and T are the seed's length and thickness respectively as previously defined. This will allow the cracking chamber to accommodate the seed along its longest dimension, while also preventing two seeds from lying side-by-side in order not to choke the chamber. x is to be greater than d (the diameter of the sphere). This ensure the seed exited the chamber uncracked when the vanes are turned in the opposite direction of the recommended motion for cracking (i.e., anti-clockwise). r is defined by the expression:

$$r = T - \delta \quad (9)$$

where T is the seed's minimum thickness (18.4 mm from Table 2) and δ is the seed's maximum deformation up to cracking point (3.5 mm from Table 2). Finally, still referencing Figure 3, OA and OB are the centres of the smaller (A) and bigger (B) cylinders respectively.

Constructing Figure 3 to scale and using pre-determined dimensions of 37 mm for diameter of cylinder A, 76 mm for cylinder B, 26 mm for sphere C (from geometric mean diameter on Table 1) and (50 mm, 50 mm) for coordinate of centre OA and (56 mm, 46 mm) for coordinates of centre OB with reference to O (see Figure 2 a), the values of angles α , β , and γ was measured as 82° , 25° , and 7° respectively. Also taking F_c as 2.0 kN (design value for cracking force greater than the maximum of 1.6 kN as displayed in Table 2), F_E and P_n were calculated as 1.21 kN and 1.76 kN respectively using Equations 6 and 7.

It should be noted that the spherical shape of the seed is only valid at the onset of cracking process, as the seed squeezed further into the narrowing space, it starts to deform to oblate form till it eventually cracked. Moreover, taking F_c as equal to cracking force at the beginning of the push by the vane of the seed is necessary to estimate the torque that must be supply via the machine crank arm by the operator in order to crush the seed. In reality, compression force progresses from zero until it reaches a maximum value at the point where the seed cracked and the seed can no longer be assumed to be spherical. However, for sake of simplicity in estimating the torque required, the above analysis gives a reasonable approximation. The torque T required is given by:

$$T = (P_n) \cdot (\gamma) \quad (10)$$

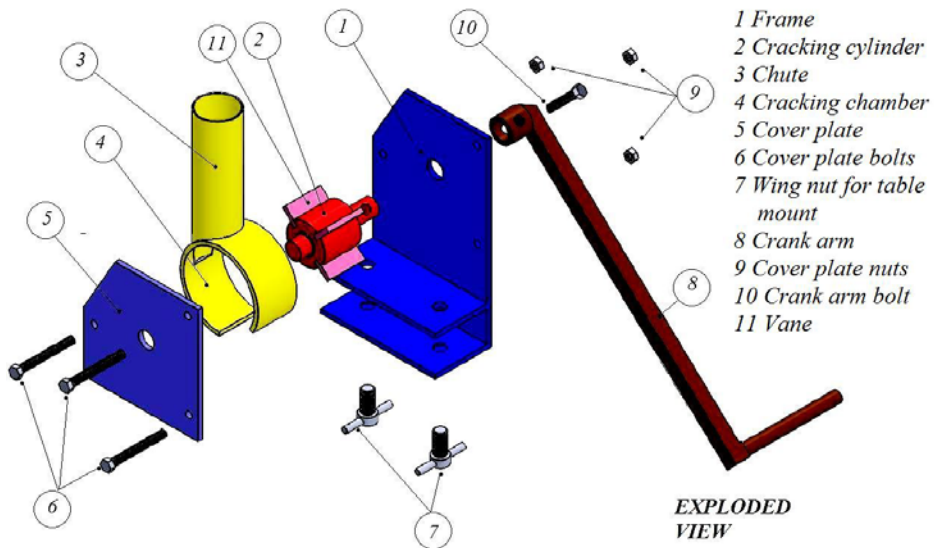
where γ is the perpendicular distance from centre OA of the smaller cylinder (A) to the point of action of force P_n in Figure 3. From the accurate geometric construction of Figure 3 using aforementioned values, γ was 24 mm thus the minimum torque required to fracture the seed via cranking was 42.24 kNmm.

5. DESIGN AND DESCRIPTION OF THE SEED CRACKING MACHINE COMPONENTS

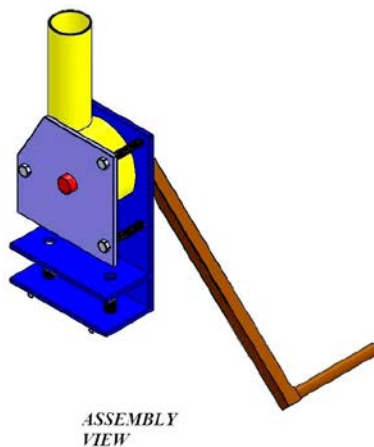
The SolidWorks rendering as well as picture of the seed cracker developed based on the previous discussion are as presented in Figure 4. The manual seed cracking machine components are:

- *The Chute*, made from mild steel, is a hollow cylinder of internal diameter 35 mm, thickness 1 mm and length 154 mm positioned to supply seeds to the chamber at a tangent. The seeds are stacked one above the other in the chute and fed into the cracking chamber under gravity. The chute length allowed for up to a maximum of 10 seeds to be loaded at a time for continuous cracking. Internal diameter 35 mm was chosen to exceed the maximum seed dimension (Tables 1 and 2) and to allow for free movement of seeds, but not big enough to hold two seeds side-by-side which may lead to chocking of the chute.
- *Cracking chamber* is formed by a hollow cylinder of internal diameter 76 mm with cylinder thickness 3.5 mm and width 37 mm. A portion of the cylinder curve was removed to provide exit for the cracked seed while the chute interface with it at a tangent as depicted in Figure 4 a. One end of the cylinder was welded at the rim to the frame in order to close it while the other end was sealed by a cover plate. Cracking chamber is equivalent to circle B in Figures 2 and 3.
- *The Frame* is as depicted in Figure 4 a. It is fabricated from mild steel plate of thickness 4 mm. It was provisioned with hole of diameter 15 mm to carry one end of the cracking cylinder shaft. It also provided surface for attaching cracking chamber by welding and has holes for securing cover plate to cracking chamber via 3 pairs of bolts and nuts. Finally, it has provision for attaching the seed cracking machine to the table.
- *Cover Plate* seals the other open end of the cracking chamber cylinder. Hole of diameter 15 mm was drilled through it. The hole serves as the support for the other end of the cracking cylinder shaft. Additionally, three holes were drilled into it at specific positions to accommodate M8 bolts and nuts which secured it to the frame. The cover plate was made from a 4 mm thick mild steel plate.
- *Cracking Cylinder* is equivalent to circle A in Figures 2 and 3. It is to be produced from mild steel and it was designed to carry four vanes on its peripheral inserted into grooves parallel to the cylinder axis. The cracking cylinder, being the active part of the machine can be failed by the shearing of the shaft from the cylinder body due to twisting (Figure 5 b) or by the shearing of the shaft from the cylinder body due to bending force induced

by the seed reaction force on the cylinder and the attendant reactions at the shaft supports (Figure 5 c).



(a)



(b)



(c)

Figure 4 SolidWorks rendering of (a) the exploded view showing the components, (b) when assembled and (c) pictorial view of the completed machine

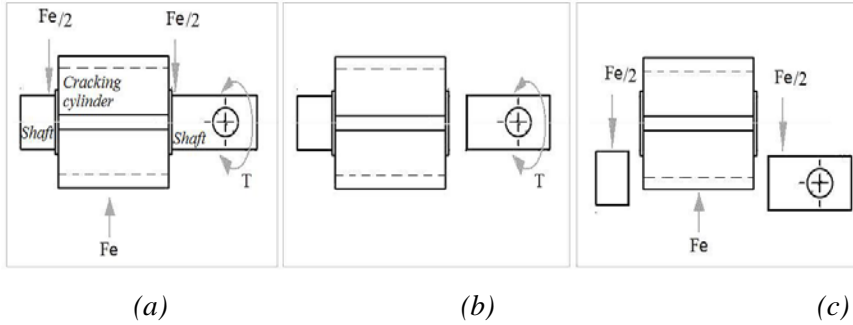


Figure 5 Modes of failure of Cracking cylinder (a) Forces and torque acting on Cracking cylinder, (b) Shearing of shaft due to twisting, (c) Shearing of shaft due to bending

(i.) Shearing of shaft due to twisting: the shear stress (τ) on the shaft due to twisting is given by the expression (Khurmi & Gupta, 2005);

$$\tau_t = \frac{16T}{\pi d_s^3} \quad (11)$$

the diameter (d_s) of the shaft had been pre-determined to be 15 mm, and torque T expected from the crank is 45.76 kNm, hence the value of τ_t is 0.064 kN/mm² (64 MPa) This is a very small value compared to the maximum shear strength for mild still of value 345-525 MPa (Designing Buildings, 2023). Thus, with the assumed value of shaft diameter, failure due to twisting forces had been eliminated.

(ii.) Shearing of shaft due to bending; considering Figure 5 c, the maximum shear force on the shaft cylinder interface is $Fe/2$ (Fe is equivalent to F_E in Figure 3) which equals the reaction at the support. The shaft is in double shear. The shear stress induced is given by the expression (Khurmi & Gupta, 2005):

$$\tau_n = \frac{2Fe}{\pi d_s^2} \quad (12)$$

where d_s is the shaft diameter. Substituting the values of 1.21 kN for Fe and 15 mm for d_s , shear force due to bending is 0.0034 kN/mm² (3.4 MPa) this value is small compared to the maximum shear strength for mild still with value 345-525 MPa (Designing Buildings, 2023). Thus, with the assumed value of shaft diameter, failure due to bending forces had been eliminated.

- *The Vane* is a mild steel rectangular prism inserted, by employing interference fit, into the slots on the Cracking cylinder. The vane dimensions as fixed by the designers due to space constraint in the chamber are as shown in Figure 6. The failure mode for vane is by bending force induced on it by the resistance of the seed to being push into narrowing space of the cracking chamber. Referring to Figure 6, the bending stress on the vane due to force F_n is given by (13) (Khurmi & Gupta, 2005).

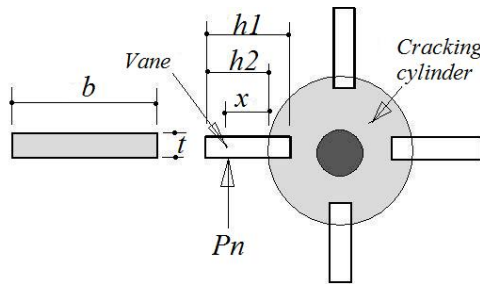


Figure 6 Force acting on the vane

$$\sigma = \frac{My}{I} \tag{13}$$

where M is the bending moment, y is the distance to the neutral axis equal to $t/2$, and I is the area moment of inertia given by (14) (Khurmi & Gupta, 2005).

$$I = \frac{bt^3}{12} \tag{14}$$

where b is the breadth (fixed at 34 mm), h_1 (fixed at 18 mm) is the overall width and, h_2 (fixed at 14 mm) is the width of the vane jutting out of the cracking cylinder curved surface and t is the thickness of the vane (fixed at 4 mm). The bending moment was calculated thus:

$$M = P_n \cdot x \tag{15}$$

x was taken as 5 mm, thus substituting the values into Equations 13-15, σ is 0.095 kN/mm^2 (95 MPa). This value is lower than the allowable normal stress for mild steel which is 155-165 MPa in bending (Bengtsson & Whitaker, 1986).

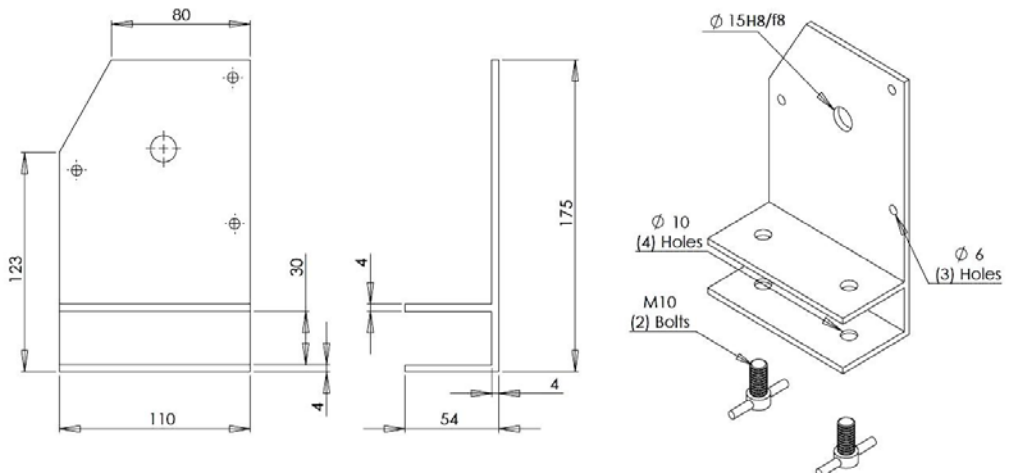


Figure 8. The Frame

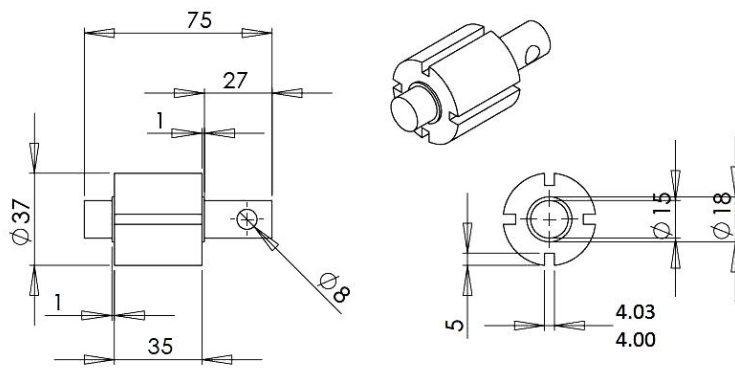


Figure 9. Cracking cylinder

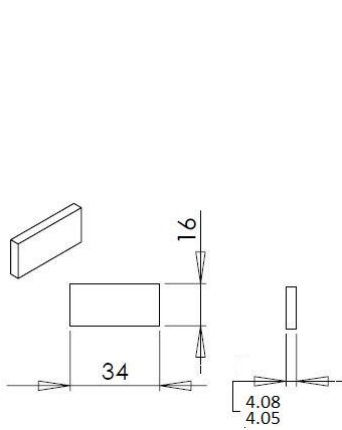


Figure 10. The Vane

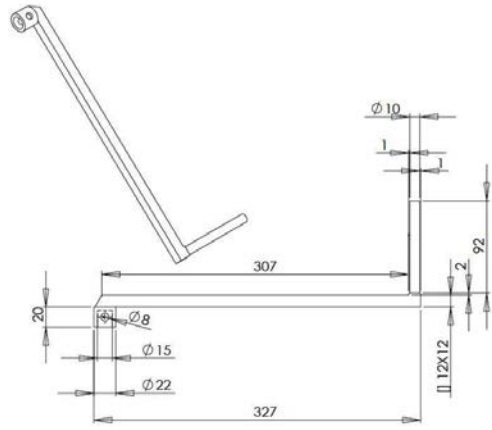
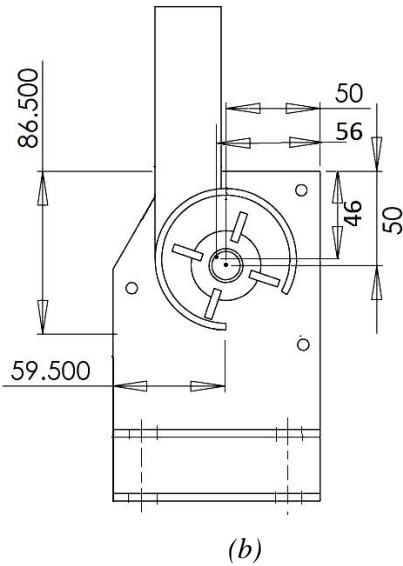
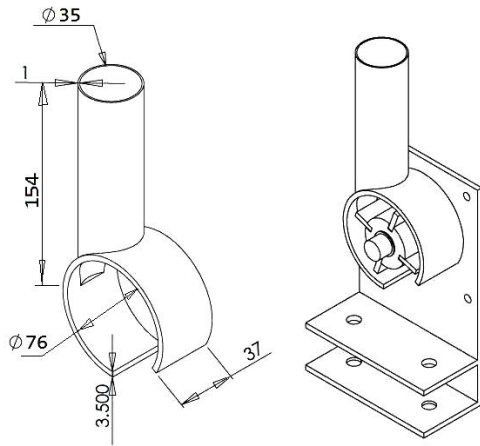


Figure 11. The Crank



(b)



(c)

Figure 12. Positioning of Cracking cylinder, Cracking chamber on Frame (a), isometric view of Chute and Cracking chamber as a single piece (b), and isometric view of (a)

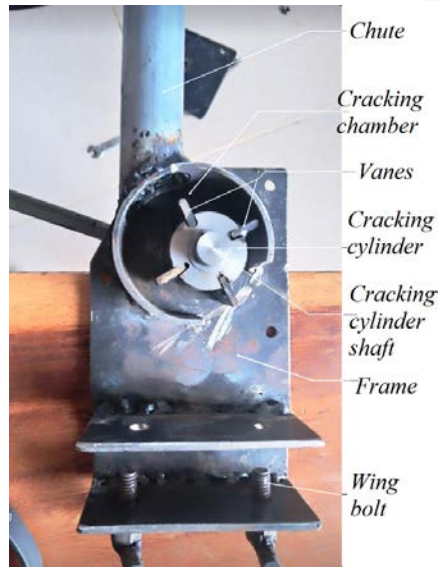


Figure 13. Pictorial views of the fabricated seed cracking machine with Cover plate removed to show the Cracking chamber and Cracking cylinder

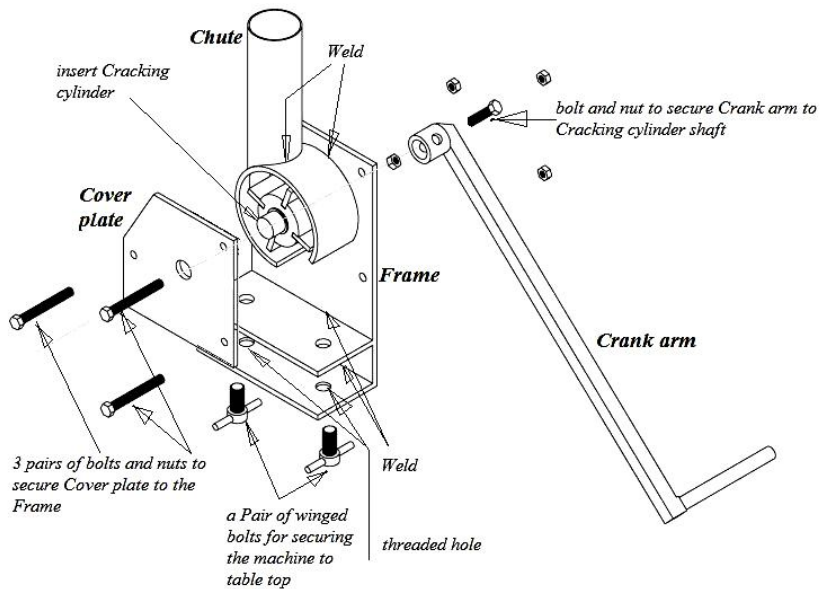


Figure 14 Isometric view showing how the components are to be assembled

Table 3
The Bill of materials

SN	Component	Quantity	Material
1	Chute	1	Galvanised Steel pipe
2	Cracking chamber Barrel	1	Mild steel
3	Cracking Cylinder	1	Mild steel
4	Vanes	4	Mild steel
5	Cover plate	1	Mild steel
6	Crank arm	1	Mild steel
7	Bolts and nuts	3 (pairs)	Hex head. M8 Grade 8.8 (ISO 4014)
8	Bolt and nut	1 (pair)	Hex head. M10 Grade 8.8 (ISO 4014)
9	Wing bolt	2	M10 Grade 8.8 (ISO 4014)

7. EVALUATION OF THE PROTOTYPE

The machine was evaluated based on (i) its seed cracking efficiency, and (ii) perceived ease of use by the user. The seed cracking efficiency (η_c) was defined as:

$$\eta_c = \frac{\text{Number of cracked seeds outputed from the machine}}{\text{Number of whole seed fed into the machine}} \quad (17)$$

Ten seeds were fed to the chute at the beginning of each test run, the machine was then cranked. After the cracking process for the whole batch is completed, the output was visually inspected to identify the uncracked ones. Equation (17) was used to calculate the cracking efficiency for the trial run. The process was repeated for five separate seed batches. Average cracking efficiency for the five test runs was found to be 96%. Of the total of 50 seeds cracked, two exited the chamber uncracked. Checking their linear dimensions revealed that their thickness were 14.8 and 14.8 mm respectively. This is below the minimum of 15 mm which was the base value used for r (Figure 3) in the design. This explains the reason why they escaped cracking. Figure 15 shows a seed sample before cracking and after cracking.

For the perceived ease of use, ten adults with age range 18 to 45 years, not familiar with where the machine was fabricated or who the designers are, were invited to operate the machine. Each was allowed three trial runs with three seed batches containing ten mature seeds each. At the end of the operations each participant was asked to judge the ease of operation of the machine based on Very Difficult to use (1 point), Difficult to use (2 points), Easy to use (3 points) and Very Easy to use (4 points). This method was based on 4-point Likert Scale. The even number Likert scale was deliberately employed to encourage the participants to make a decision after actually using the machine and to discourage indifference. Since

the machine fabricated is the prototype, critical appraisal of its performance will be crucial for future improvement. From the analysis of the participants' responses, the average of their point-based choices was found to be 3.1. This indicated that averagely, the participants find the machine Easy to use.

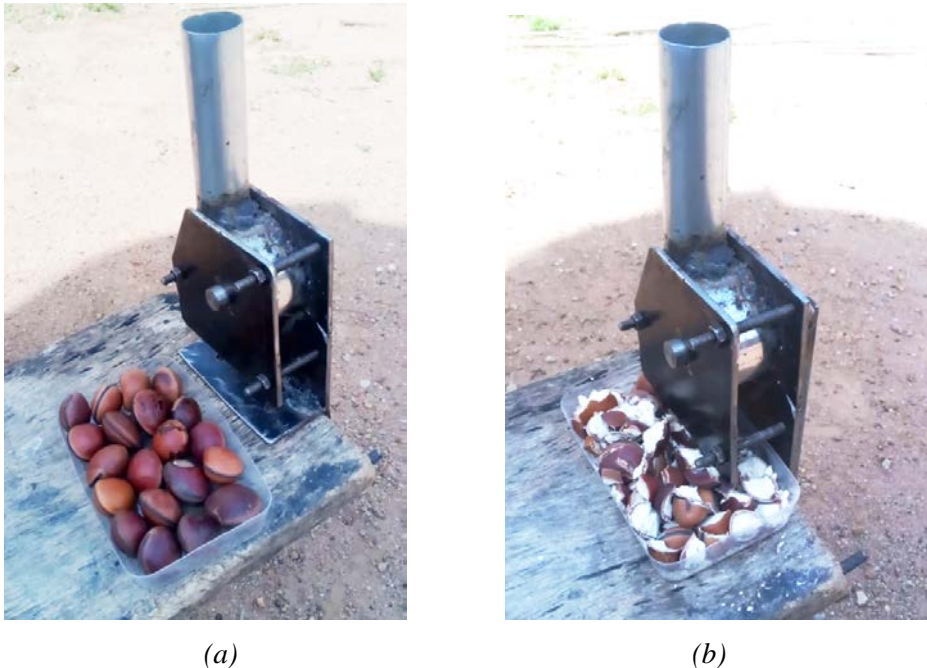


Figure 15. Machine with whole *Deocla reflexa* seed sample (a)
Machine with the cracked product derived from the sample(b).

8. SUMMARY

A hard seed (*Dioclea reflexa* Hook f.) cracking machine was conceived and developed based on the concept of forcing the seed through a narrowing rigid passageway until sufficient reactive force at the passage-seed interface cracks the seed. The concept was both graphically and mathematically analysed taking into consideration the seed's engineering properties. From the results of the analysis, a prototype of the machine was fabricated as a proof of concept and was evaluated for seed cracking efficiency and perceived ease of use by the users. Results indicated that the machine developed achieved 96% cracking efficiency and test

subjects invited to operate the machine reported on the average that the machine was easy to use.

ACKNOWLEDGEMENT

The authors wish to acknowledge the contributions of Toyeeb Saberedowo an undergraduate student at the Department of Mechanical Engineering, Osun State University Osogbo Nigeria, in the aspect involving the rendering of the technical sketches of the machine components into working drawings using SolidWorks, as well as Kayode Babatola a technologist in the department for the technical skill offered in the fabrication of the machine prototype.

REFERENCES

Ajatta, M. A., Akinola, S. A., Otolowo, D. T., Awolu, O. O., Omoba, O. S., & Osundahunsi, O. F. (2019). Effect of Roasting on the Phytochemical Properties of Three Varieties of Marble Vine (*Dioclea reflexa*) Using Response Surface Methodology. *Preventive Nutrition and Food Science*, 24(4), 468-477. doi:<https://doi.org/10.3746/pnf.2019.24.4.468>

Ajayi, I. A. (2014). Oil Content and Fatty Acid Composition of *Dioclea reflexa* Seeds. *IOSR Journal of Applied Chemistry*, 7(7), 68-73.

Bengtsson, L. P., & Whitaker, J. H. (1986, March 30). *Farm Structures in Tropical Climates: A Textbook for Structural Engineering and Design*. Rome: Food and Agriculture Organization of the United Nations. Retrieved from www.fao.org/3/S1250E/S1250E1i.htm

Designing Buildings. (2023, March 30). Retrieved from The construction wiki: https://www.google.com/url?q=https://www.designingbuildings.co.uk/wiki/Shear_strength&sa=U&ved=2ahUKEwiVq_TI7MD_AhWLi1wKHaAaDh0QFnoECAEQAw&usg=AOvVaw18lIRW9w9b3Oy-ymzWWJ1I

Engineering Toolbox. (2023, March 30). Retrieved from www.engineeringtoolbox.com/human-force-power-d_2086.html

Fayed, M. I., El-Shal M.S., M. S., & Omar, O. A. (2020). Determination of some apricot seed and kernel physical and mechanical properties. 22(4), 229-237.

Kayode, O., Adeleke, K., & Alade, E. (2020). Design of a Single Mast, Retractable Carport Canopy. *Machine Design*, 12(1), 15-20.

Khurmi, R. S., & Gupta, J. K. (2005). *Textbook of Machine Design* (14th Revised Edition ed.). New Delhi, India: S. Chand & Co.

Mbah, C., Samali, A., Aboh, M. I., Ogbonna, J. I., Builders, P. F., Attama, A. A., & Ofoefule, S. I. (2022). Preliminary investigation of Dioclea reflexa seed gum as a food and potential pharmaceutical excipient. *German Journal of Pharmaceuticals and Biomaterials*, 1(4), 27-37.
doi:<https://doi.org/10.5530/gjpb.2022.4.17>

Olukayode, O., Alade, E. I., & Oyelami, S. (2022). Effect of moisture contents and compression axes on some physical and mechanical properties of Dioclea reflexa seed. *Journal of Applied Life Sciences and Environment*, 55(2), 189-200.
doi:<https://doi.org/10.46909/alse-552057>

INVESTIGATION OF THE INVOLUTE SPUR GEARS WITH DIFFERENT PRESSURE ANGLES

ÁDÁM SÁNDOR PINTÉR¹- FERENC SARKA²

¹*University of Miskolc, Machine Tools and Mechatronics,
H-3515 Miskolc-Egyetemváros
pinter.adam.1998@gmail.com*

²*University of Miskolc, Institute of Machine and Product Design,
H-3515 Miskolc-Egyetemváros,
ferenc.sarka@uni-miskolc.hu*

¹<https://orcid.org/0000-0002-6555-3664>, ²<https://orcid.org/0000-0003-3136-4248>

Abstract: This article deals with an investigation of the choice of the profile shift coefficient for gears when the standard pressure angles of the gears are different. The basic idea for the study arose from a real-life problem where a gear in a piece of equipment needed to be replaced. In this article, a method is presented to determine, by approximation, the value of the profile shift coefficient that we have to use on a gear having 20° pressure angle to get similar tooth profile of a gear without profile shift and 21° of pressure angle. In addition, theoretical investigations are also carried out on the topic of gear meshing, using the profile shift coefficient.

Keywords: *gear CAD model, profile shift coefficient, gear meshing*

1. INTRODUCTION

Gear drives cover a very large area of conventional engineering. It is therefore not surprising that their study is still a very important part of research today. For us, such a topic arose during a real industrial task. In this article, we therefore focus on the study of gear meshing and the choice of the profile shift coefficient. The question is given, whether gears with different pressure angles can be coupled, and if so, with what amount of error. The task was to realize a gear connection with a pressure angle of 21° and a gear connection with a pressure angle of 20°. Therefore, the theoretical gear meshing investigation will be one of the important points. In addition, the use of profile shifting will be used to create gears with different pressure angles but nearly identical tooth profiles. It is also a task in the

article to determine what profile shift coefficient should be applied to change the tooth profile of a gear with a pressure angle of 20° to match as closely as possible the tooth profile of a gear without profile shift with a pressure angle of 21° . Finally, it is also investigated whether two gears with different pressure angles can be interchanged without changing the module.

2. MATING GEARS WITH DIFFERENT PRESSURE ANGLES AND MODULES

The question may arise whether it is even possible to design gears with different pressure angles. So, the question is, can a gear with a pressure angle α_1 be replaced by a gear with a pressure angle α_2 ? The meshing of two gears can be achieved if the meshing points run along the common inner tangent of the base circles of the two gears. Figure 1 is attached for reference. From the figure, we can say that for spur gears, the contact is along the line of action. The line of action itself is a tangent line drawn to the base circle.

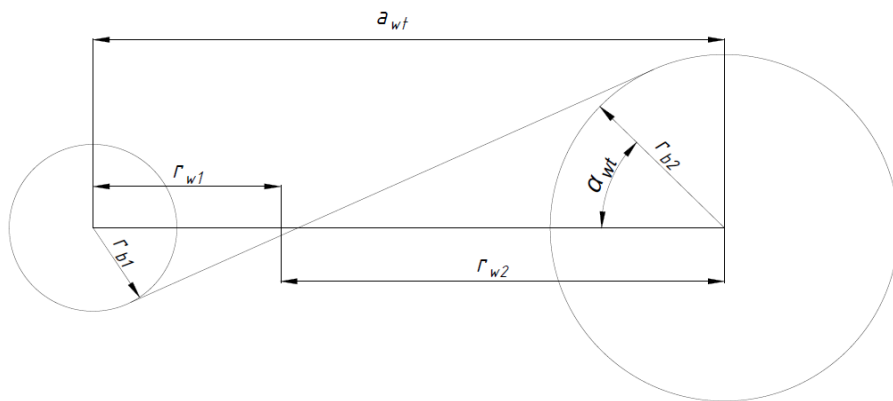


Figure 1. Interpreting the line of action of spur gears

Using the basic assumption that identical involute curves can only be derived from the same base circle (d_b), we can express the diameter of the base circle, which is given by (1):

$$d_b = z \cdot m \cdot \cos \alpha, \quad (1)$$

where z is the number of teeth, m is the modulus and α is the pressure angle. Based on the distinction between the two gears, let number 1 denote the original gear and number 2 the substitute gear. Since the number of teeth cannot vary, the following relationship must be satisfied for the two base diameters to be equal:

$$d_b = z \cdot m_1 \cdot \cos \alpha_1 = z \cdot m_2 \cdot \cos \alpha_2. \quad (2)$$

Rearranging (2) and expressing one of the modules, we obtain the relationship between them:

$$m_2 = m_1 \cdot \frac{\cos \alpha_1}{\cos \alpha_2}. \quad (3)$$

If we start from a different direction, namely from the assumption that the two gears must have the same base pitch (p_b) for a continuous connection, the following relationship is obtained:

$$p_b = m_1 \cdot \pi \cdot \cos \alpha_1 = m_2 \cdot \pi \cdot \cos \alpha_2, \quad (4)$$

which gives the relation (3). As commercially available gear cutting tools are made with a standard set of modules, condition (3) can only be achieved for chipped gears at a significant extra cost. However, if we turn towards additive manufacturing, or consider injection moulded plastic gears, then for these gears the constraints on the module are not present, so condition (3) can be fulfilled without difficulty.

3. MATING GEARS WITH DIFFERENT PRESSURE ANGLES

So, in this study, we are looking for the answer to the question, what kind of mesh is shown between two gears with different pressure angles if the module is unchanged. The starting point is that if the module is the same, the base circle diameters will be different:

$$d_{b1} = z \cdot m_1 \cdot \cos \alpha_1, \quad (5)$$

$$d_{b2} = z \cdot m_1 \cdot \cos \alpha_2. \quad (6)$$

In the case where (5) and (6) hold, the involute curves will also be different because of the difference in the base circles. This divergence is illustrated in Figure 2.

Since the centre distance cannot change, the centre of the base circles coincides. If you sweep a straight line on each of the two base circles, you get intersecting involute curves. Figure 2 shows the tangents of the two base circles and the base circles at the intersection point M. The n_1 and n_2 will be the normal of the involute profiles at point M. By varying the position of point M, i.e., the radius r_y , an infinite number of intersections are possible, whose locations are determined by the profile shift coefficient of the two gears.

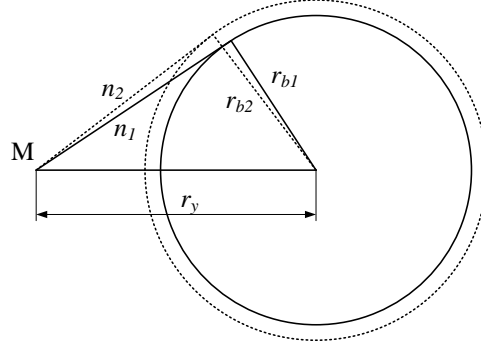


Figure 2 The different base circles and their corresponding tangent lines

Hence, we investigate under what conditions the tooth thickness of the two gears is the same at the radius r_y . To do this, we write down the relationship of the tooth thickness at an arbitrary radius:

$$s_y = 2 \cdot r_y \left[\frac{1}{z} \cdot \left(\frac{\pi}{2} + 2 \cdot x \cdot \tan \alpha \right) + \text{inv} \alpha - \text{inv} \alpha_y \right]. \quad (7)$$

We apply this relationship to the case of the two gears:

$$s_{y1} = 2 \cdot r_y \left[\frac{1}{z} \cdot \left(\frac{\pi}{2} + 2 \cdot x_1 \cdot \tan \alpha_1 \right) + \text{inv} \alpha_1 - \text{inv} \alpha_{y1} \right], \quad (8)$$

$$s_{y2} = 2 \cdot r_y \left[\frac{1}{z} \cdot \left(\frac{\pi}{2} + 2 \cdot x_2 \cdot \tan \alpha_2 \right) + \text{inv} \alpha_2 - \text{inv} \alpha_{y2} \right]. \quad (9)$$

In order to meet the requirement that the two tooth profiles are identical, the tooth thicknesses must be made equal. Thus, the equality between the two tooth thicknesses is given by:

$$\begin{aligned} 2 \cdot x_1 \cdot \tan \alpha_1 + z \cdot (\text{inv} \alpha_1 - \text{inv} \alpha_{y1}) &= \\ &= 2 \cdot x_2 \cdot \tan \alpha_2 + z \cdot (\text{inv} \alpha_2 - \text{inv} \alpha_{y2}). \end{aligned} \quad (10)$$

From this relationship we can express one of the profile shift coefficients:

$$x_2 = \frac{2 \cdot x_1 \cdot \tan \alpha_1 + z \cdot (\text{inv} \alpha_1 - \text{inv} \alpha_2 - \text{inv} \alpha_{y1} + \text{inv} \alpha_{y2})}{2 \cdot \tan \alpha_2}. \quad (11)$$

Since in our study we only apply a profile shift coefficient to one of the gears, the relationship for $x_1 = 0$ is as follows:

$$x_2 = \frac{z \cdot (\text{inv}\alpha_1 - \text{inv}\alpha_2 - \text{inv}\alpha_{y1} + \text{inv}\alpha_{y2})}{2 \cdot \tan \alpha_2}, \quad (12)$$

(11), at a given radius r_y , the tooth thicknesses are identical, but at smaller and larger radii the thicknesses of the two gears differ, so that at smaller radii one tooth is thicker and at larger radii the other tooth is thicker. However, if the value of x_2 is chosen carefully, the difference can be minimised within a given r_y range. In this way we can create a very similar gear. However, a further problem arises, namely that the base pitch of the two gears is not the same, which follows:

$$p_{b1} = m_1 \cdot \pi \cdot \cos \alpha_1, \quad (13)$$

$$p_{b2} = m_1 \cdot \pi \cdot \cos \alpha_2. \quad (14)$$

However, the consequence of the relation (13) and (14) will be that smooth operation is not ensured. Even if we ensure that one tooth is in alignment, the next tooth will come into contact too soon, or too late. The tooth clearance of the replacement wheel may be too wide or too narrow for the tooth of the corresponding gear.

In summary, it is not theoretically possible to mesh gears with different pressure angles but the same module. In practice, with a clever choice of profile shift coefficient and clearance, it is conceivable, but a very poor-quality pair of gears will result. The consequences can be uneven running, high noise levels and heavy wear.

4. DETERMINATION OF THE PROFILE SHIFT COEFFICIENT

In the previous point, we examined gears that had the same module (standard) and had different pressure angles. If we waive the requirement that the module have to be standard and identical on both wheels (this is possible in the case of additive manufacturing or injection moulding), the question arises as to whether we can better approximate the two profiles.

To create completely identical profiles, it is necessary that the base circle diameter of the two gears, with different pressure angles, be the same.

Then we look for the profile shift coefficient that gives the same base circle for a 20° pressure angle as in the case of a 21° pressure angle non-profile shifted gear. We are looking for equivalence with the help of an example. The base gear, with a pressure angle of $\alpha_1=21^\circ$, tooth number $z=17$, module $m_1=3$ mm, profile shift coefficient $x=0$, (indicate the base gear with index 1).

The radius of the pitch circle:

$$r_1 = \frac{z}{2} m_1 = 25.5 \text{ mm} \quad (15)$$

Radius of the base circle:

$$r_{b1} = r_1 \cdot \cos(\alpha_1) = 23.806 \text{ mm} \quad (16)$$

Radius of the addendum circle:

$$r_{a1} = \left(\frac{z}{2} + 1 + x_1 \right) \cdot m_1 = 28.5 \text{ mm} \quad (17)$$

Tooth thicknesses (s_{y1i}) can be calculated by arbitrarily dividing the distance between the base circle and the addendum circle. Knowing the radii, the corresponding profile angle can be determined, and then the tooth thicknesses can be determined. Dividing the range between the base circle and the head circle into $i=5$ equal parts, we get the values in the following table (Table 1). The relations used for the calculation are (18)-(21).

The pitch between the radiuses:

$$\Delta r = \frac{r_{a1} - r_{b1}}{5} \quad (18)$$

Radius:

$$r_{yi} = r_{b1} + i \cdot \Delta r \quad (19)$$

Profile angle:

$$\alpha_{y1} = \cos^{-1} \left(\frac{r_{b1}}{r_y} \right) \quad (20)$$

Tooth thickness:

$$s_{y1i} = \left(\frac{s_1}{2r_1} + \tan \alpha_1 - \alpha_1 - \tan \alpha_{y1i} + \alpha_{y1i} \right) \cdot 2r_{yi} \quad (21)$$

Table 1.
Tooth thickness values for an arbitrary radius

Radius r_{yi} [mm]	Tooth thickness s_{y1} [mm]
23.806	5.225
24.745	5.072
25.685	4.601
26.623	3.902
27.561	3.003
28.5	1.919

Once we know the tooth thicknesses and base diameter of the base gear, we can find out what kind of replacement gear we can create. We are looking for the module and profile shift factor of the new wheel, and we know the pressure angle $\alpha_2=20^\circ$, tooth number $z=17$.

The module of the new gear will differ from the module of the base gear, based on equation (13) and (14):

$$m_2 = m_1 \cdot \frac{\cos \alpha_1}{\cos \alpha_2} = 2.98 \text{ mm} \quad (22)$$

This ensures that the base pitch of the two wheels will be the same. The pitch radius of the new gear (23):

$$r_2 = \frac{z}{2} m_2 = 25.334 \text{ mm} \quad (23)$$

The base circle radius of the new gear is the same as the base circle radius of the base gear.

$$r_{b2} = r_2 \cdot \cos(\alpha_2) = 23.806 \text{ mm} \quad (24)$$

Since the two base radii are the same, the involute of the two gear profiles is also the same. By changing the profile shift coefficient, the involute profile is moved to a new position, from the point of view of the gear, this means a thicker or thinner tooth. We can find a profile shift coefficient at which the two tooth profiles overlap, the tooth thickness of the two gears will be the same.

Using (12) and realizing that the profile angles will be the same at a given radius for the base and replacement gear, (12) can be simplified.

Equality of profile angles:

$$\alpha_{y1} = \cos^{-1} \left(\frac{r_{b1}}{r_y} \right); \alpha_{y2} = \cos^{-1} \left(\frac{r_{b2}}{r_y} \right), \quad (25)$$

but $r_{b1}=r_{b2}$, so $\alpha_{y1}=\alpha_{y2}$, therefore their involutes are also equal. Knowing all this, the profile shift coefficient of the replacement gear is as follows:

$$x_2 = \frac{z}{2 \cdot \tan \alpha_2} \cdot (\tan \alpha_1 - \alpha_1 - \tan \alpha_2 + \alpha_2) = 0,057 \quad (26)$$

If the tooth thicknesses are calculated for the replacement gear, we get the same values as calculated for the base gear. In other words, the profile of the two gears is the same, their module is different, and their pressure angle is different.

5. FURTHER RESEARCH DIRECTIONS

A direction to take this research further could be to investigate the relationship between the mesh of an elementary and a profile shifted gear compared to the mesh of two elementary gears.

The aim is to create assembly models for this purpose, as has been done previously (Pintér & Sarka, 2021), (Pintér & Sarka, 2022), and in these situations to compare, by means of FEM analysis studies, how the values measured at each contact, such as stress distribution, deformation, surface pressure, magnitude of slip, relate to each other. This would also allow us to infer how our gear contact, currently constructed using a profile shift coefficient, with the elemental gear, and resembles the element-element gear coupling.

6. SUMMARY

In the field of mechanical engineering, gear drives are still very common today. Gear drives can be found in many places and are still in widespread use. For this reason, this article has been written about gear meshing. The study looked at the meshing of gears with different pressure angles, whether they can be mesh without failure, and what the conditions are for this mesh. On the topic of profile shift coefficient, we investigated, based on a real industrial problem, how to find a profile shift coefficient that gives a similar tooth profile when the pressure angle is different. We also investigated the theoretical background of this question, how a gear can be substituted when the pressure angle is different if the module is also unchanged. In addition, we have identified the errors and problems that may arise in this case.

ACKNOWLEDGEMENT

The Authors would also like to say thank Dr. József Szente, Titular Professor, for his help in researching the topic.

Supported by the ÚNKP-22-2. New National Excellence Program of the Ministry for Culture and Innovation from the source of the National Research, Development and Innovation Fund.”



REFERENCES

Bodzás, S. (2019). Designing and analysis of special gear pairs by GearTeq and SolidWorks softwares., *7th International Scientific Conference on Advances in Mechanical Engineering Conference Proceedings*, pp. 21-22. Debrecen.

ISO. (2006). ISO 6336-3. *Calculation of load capacity of spur and helical gears Part 1: Basic principles, introduction and general influence factors*.

Park, S.-J., & Yoo, W.-S. (2003). Profile Shift Coefficient of Gear System Considering Teeth Deflection. *Transactions of the Korean Society of Mechanical Engineers A*, 27(5), 758-763. doi:<https://doi.org/10.3795/ksme-a.2003.27.5.758>

Pintér, Á. S., & Sarka, F. (2021). CAD rendszerek által generált fogazott elemek alakeltéréseinek vizsgálata. *GÉP*, 72(3-4), 85-88.

Pintér, Á. S., & Sarka, F. (2022). Contact pattern investigation of gear drives using finite element method. *Design of Machines and Structures*, 12(1), 63-74. doi:<https://doi.org/10.32972/dms.2022.006>

Pintér, Á. S., & Sarka, F. (2023). Fogaskerék profilpontok létrehozása profileltolás tényező alkalmazása esetén. *Multidiszciplináris tudományok*, 13(1), 12-20. doi:<https://doi.org/10.35925/j.multi.2023.1.2>

Sarka, F. (2019). Gördülőfelületek hordképvizsgálata. *Multidiszciplináris tudományok*, 9(1), 172-177. doi:<https://doi.org/10.35925/j.multi.2019.1.22>

MODELLING POSSIBILITIES OF BOLT CONNECTIONS WITH FINITE ELEMENT METHOD

FERENC SARKA

*University of Miskolc, Institute of Machine and Product Design,
H-3515 Miskolc-Egyetemváros,
ferenc.sarka@uni-miskolc.hu
<https://orcid.org/0000-0003-3136-4248>*

Abstract: In the article, the possibilities of simulating bolted joints in the Ansys finite element program are presented. The purpose of the publication is to draw attention to the various simulating options. In the article, different simulation options are used for the same model. The versions to be used are 1) bolt connection without preload 2) bolt-tool, 3) beam-tool, 4) real screw thread modelling. In the article, I rely on previous publications, so some stages are presented in less detail than others. During the simulations, I compare the number of elements used, number of nodes, running time, stress and deformation results. The model used is a closed space loaded with internal pressure, which is divided into two halves. A gasket is installed between the two halves, the two halves are fastened to each other by a row of screws. In order to manage the running times, I only examine the part of the entire model corresponding to one screw. The screw joint is loaded with pretension, and the connecting elements with a constant pressure. Where possible in the software, the tightening torque is also taken into account. The results are presented in tabular form for easier comparison.

Keywords: *Ansys, Bolt-tool, Bolt pretension, Beam, simulation of bolt connection*

1. INTRODUCTION

In technical life, we come across many machine elements that basis appeared as far back as ancient times, screws are among them. The creation/description of the helix is linked to the name of the ancient Greek scientist Archimedes. As early as III century BC. he created the mathematical description of the helix, on the basis of that several inventions were born (for example, the water-lifting screw). With the help of a flat cross section guided along a screw line, a screw thread –used since ancient times– can be created and the screw joint created by its application. Today, screw connections have become the most frequently used fasteners, and

have even become the most common machine components. They are widely used in the machinery industry due to their simplicity, relatively low prices and easy installation and removal, as well as the possibility of repeating the installation almost any number of times. Unfortunately, the compulsion to cut costs and reduce assembly times results in screw joints being pushed out of more and more places, which is contrary to the aspirations of a sustainable economy that is gaining more and more voice nowadays and puts less strain on natural resources. Unfortunately, money is always the lord, which is why we constantly destroy our environment (respect to the few exceptions).

The exchangeability and reparability of defective elements and thus the extension of the life of products (even vehicles) is more easily achieved by using screw connections. Based on the aspects described above, it is important to have as much detailed knowledge as possible of the ‘functioning’ and simulation of bolted joints.

The finite element simulation of bolted joints was investigated by many researchers (both homeland and foreign) previously, based on many different aspects. It is impossible to summarize the results of all of them in this article, so I do not attempt to complete the literature review. This research work is a continuation of an already started study, but it is also a preliminary study, a research on the optimisation of the layout, tightening torque and tightening sequence. (Lovas, 2018), (Lovas, 2020), (Sarka, 2022), (Bocko, Lengvarský, & Huňady, 2020), (Alfattani, 2020).

2. THE USED CAD MODEL

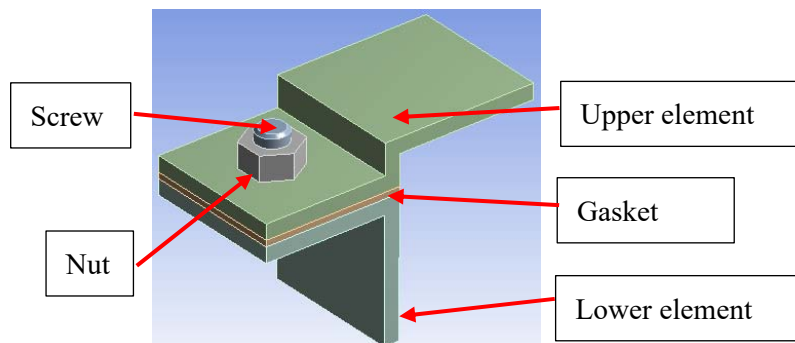


Figure 1 The used CAD model is displayed in the finite element program

In the publication, I examine the part of a container loaded with internal pressure that falls on one screw. The model can be seen in Figure 1. I leave out the

chamfers, fillets, rounds and the washer from the screw connection, for easier handling. The fasteners are M10 size.

The model consists of a lower and an upper element, which are connected by a screw connection, with a gasket between them. The screw connection is made up of two elements, one is the nut, the other is the screw, neither of them contains a thread. The material of the gasket is silicone, the other elements are structural steel. When creating a finite element model, it is very important to set the contact properties between the elements. By default, the Ansys program sets all contacts to 'bonded', which actually behaves as if the two surfaces are glued/welded together. Unfortunately, we have to modify this. The contacts on both sides of the gasket, between the screw head and the plate and between the nut and the plate must be set to 'rough', which allows the separation of the elements i.e., only compressive force can be transmitted through the surfaces. To achieve the exact solution, enable the option of large deformations on the 'analysis settings' tab. If we don't want to create a tight connection, that is, if we put the nut on the screw without tightening it, we are ready. The boundary conditions can be seen in Figure 2. The value of the internal pressure was set to 0.2 MPa, and the lateral surfaces were fixed.

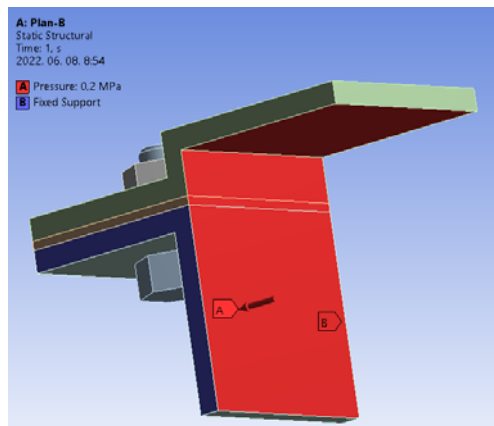


Figure 2 The boundary conditions

This is the simplest model of a screw joint. I did a trial run to see how the conditions were developing. The displacements and stress distribution can be seen in Figure 3.

We can retrieve the gasket conditions from the system using the 'Contact Tool'. With this, we can even check whether the gasket really insulate in place, or whether a leak may occur as a result of a given internal pressure (Figure 4). The

running time was 180 seconds (main parameters of the computer used: Intel core i5, 5th gen, 16Gb RAM). Of course, in technical practice we rarely use bolted joints without pretension, so in the next simulations we will switch to simulating pretensioned bolted joints.

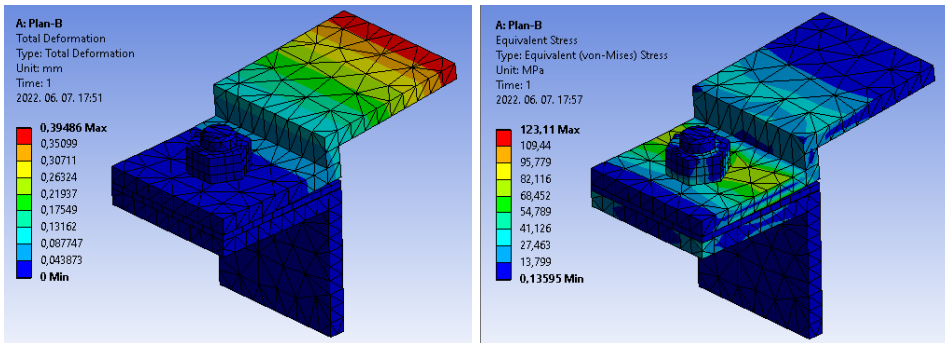


Figure 3 Finite element model of bolted connection, displacements, and stresses

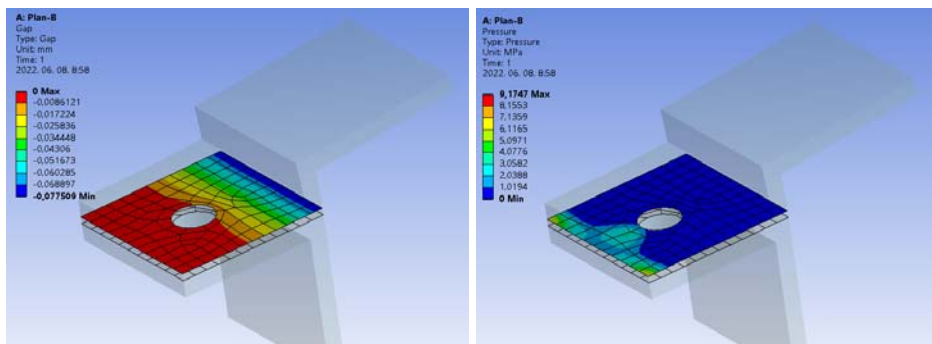


Figure 3 Contact Tool results

3. USING ‘BOLT PRETENSION’ AND ‘BOLT-TOOL’

In the Ansys finite element program, the ‘Bolt pretension’ and ‘Bolt-tool’ options were developed to model the clamping force created by bolted joints. In this case too, it is sufficient to model the screw without thread. The ‘bolt pretension’ is found among the loads, we have to apply it to the cylinder symbolizing the screw shank and enter the value of the pretension force in N. In a real installation case, the screw is tightened/pre-tensioned first, the loads resulting from the operation of the given structure only appear afterwards. We can specify this in the finite element program as well. It can be specified in the ‘Analysis setting’ section,

where the number of time steps must be set from 1 to a larger. For the present study, I chose 3. In the first-time step, the screw is pre-tensioned, which pre-tension must remain until the end of the simulation (Figure 5, circled in red).

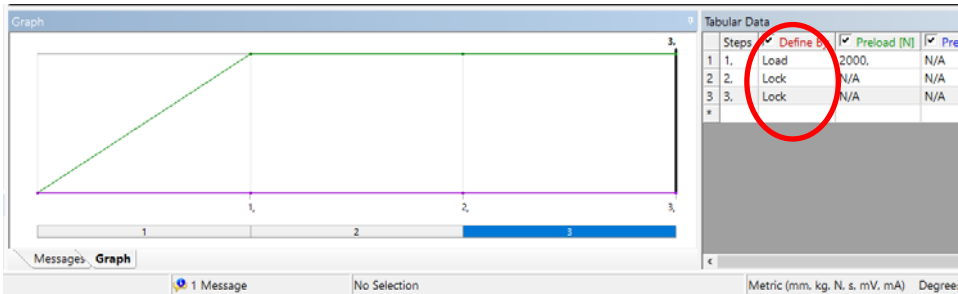


Figure 4 Adjustment of the time course of the screw preload

In the third time step, the internal pressure appears as a load. The value of the load was set to 0.2 MPa, as it was in the previous case. Figure 6 shows how the value of the internal pressure changes as a function of time.

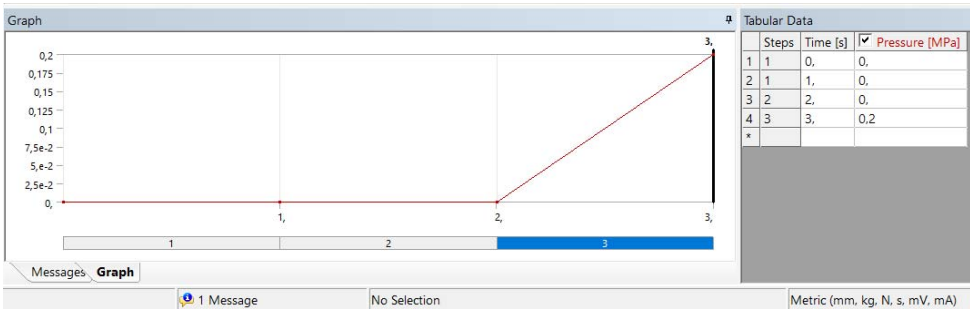


Figure 6 The build-up of internal pressure over time

The results of the simulation can be seen in Figure 7. The value of the deformation decreased slightly, and the value of the stress increased. The changes are not significant, 0.04 mm and 7 MPa.

The simulation ran in 240 seconds, which is already a significant increase (33%) compared to the previous test, but it characterizes the real situation much better. The visible change in the results of the ‘contact-tool’ is presented in Figure 8, which is already significant compared to the results of Figure 4.

Observing the gap result, it can be seen that the completely closed surface part has become larger than it was before, it completely surrounds the screw hole. And the

pressure on the seal increased from 9 MPa to 11 MPa, which is an increase of 22.5%. The increase in contact pressure is caused by the deflection of the screw shank.

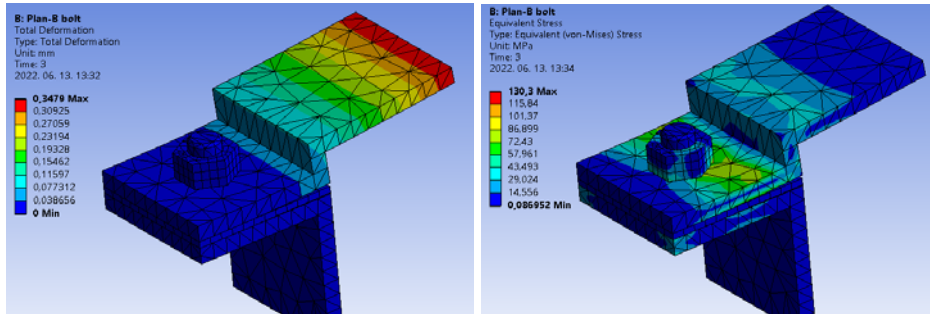


Figure 7 A pretensioned bolt connection simulated using 'Bolt pretension'. Displacements and stresses

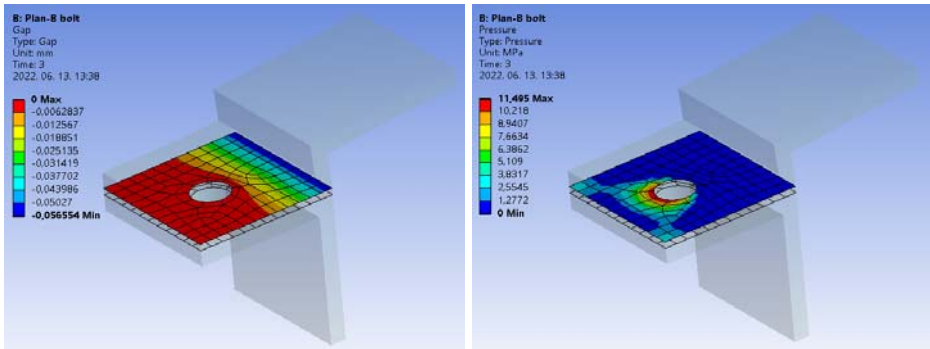


Figure 5 Results of 'Contact Tool' using 'Bolt pretension'

4. THE USE OF THE 'BEAM TOOL'

The ANSYS program gives the opportunity to incorporate various elements into a model already created in a CAD program, such as (spot welding, spring, joint, bearing, or beam). During the simulation I will use the 'Beam' command among the many options. The existing bolt model is removed with the 'Supress' command and a bar is placed in its place with the 'Beam' command. The 'Beam' command can be invoked between contacts with an 'insert' command. We need to specify the shape of the cross section of the bar, which will be circular. Modelling the shank of the M10 screw, we need to specify the radius of the cross section,

which is 5 mm. After that, we have to specify which geometries define the newly inserted bar. The first geometry is the element that does not move, the second is the element that moves relative to it. Figure 9 shows the inserted bar (red arrow). The centre line of the bar will be determined by the centre of the two selected surfaces. The elements simulating the screw head and nut will be the selected surfaces (green arrows).

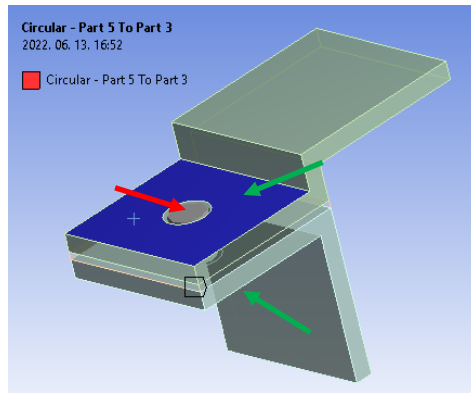


Figure 6 The inserted bar element

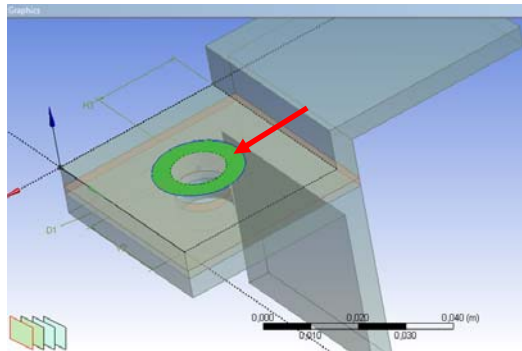


Figure 7 Modelling the bearing surface of the screw head and the nut

The settings described above involve larger surfaces in the analysis than the contact surfaces of the nut and screw head used in the previous case. In order to eliminate this, a surface part must be marked on the previously marked surfaces, which is approximately the same as the contact surfaces of the screw head and the nut. During the simulation, a circle with a diameter of 17 mm is created. This can be done by returning to the CAD system or in the ‘Design Modeler’ module of the

finite element program itself. Figure 10 shows the model of the contact surface of the screw head marked in green. Of course, this surface must also be created on the bottom plate. During the settings, you have to modify the behaviour of the contacting surfaces. The behaviour must be set to ‘deformable’ so that the overly stiff surfaces do not affect the results!

After installing the beam as a screw shank, we can see the resulting model in Figure 11. All other boundary conditions in the model remained unchanged.

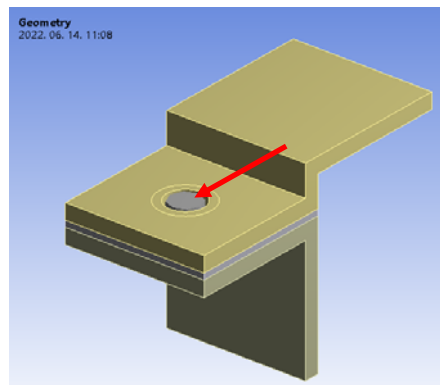


Figure 8 The model used for the 'Beam' tool

In order for the pretension to be applied to the ‘Beam’ model in our model, we need to drag the created ‘Beam’ element between the loads, then the ‘Bolt pretension’ will appear between the loads (Figure 12).

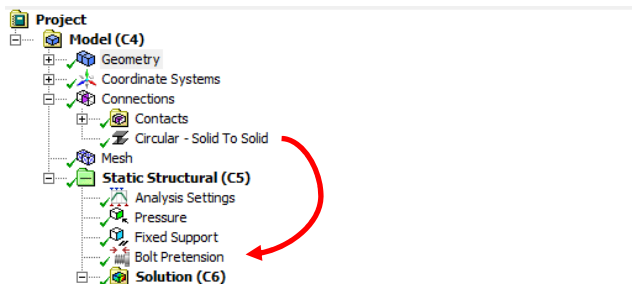


Figure 9 Creating a bolt preload when using the 'Beam' tool

The simulation showed the following result after a few seconds of runtime. We encounter an increase in both displacement (5%) and tension (20%). The increase in maximum stress can be said to be significant, but luckily it is limited to

the edge of the hole. The rest of the model falls within the same stress range as the previous simulation. The results of the ‘Contact-tool’ are shown in Figure 14.

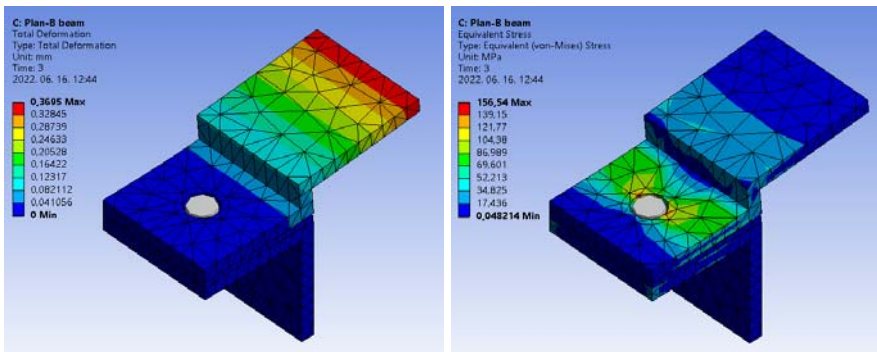


Figure 10 Bolt joint in tension simulated using 'Beam'. Displacements and stresses

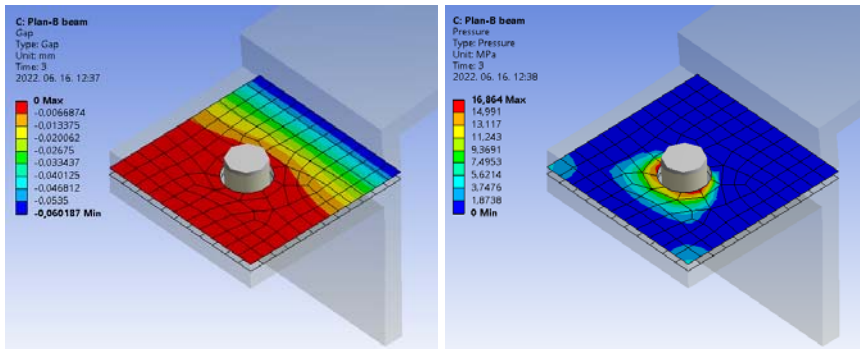


Figure 11 Results of "Contact-tool" using "Beam", gap and surface pressure values

Both the gap (8%) and the surface pressure (48%) increase. The increase in surface pressure is significant. The running time is a few seconds long, which is insignificant compared to the 240 second time of the option presented in Chapter 3.

5. REAL MODELLING OF SCREWS

The closest to reality modelling of screw joints is described in detail in the literature (Sarka, 2022). The results of the simulation based on what was described there are presented below. In the following figure, we can see the applied model

and the applied boundary conditions (Figure 15.). A new load appears for the boundary conditions, and this is the tightening torque of the screw connection. We also meet a new support, which is located on the head of the screw. This support simulates a wrench used when tightening.

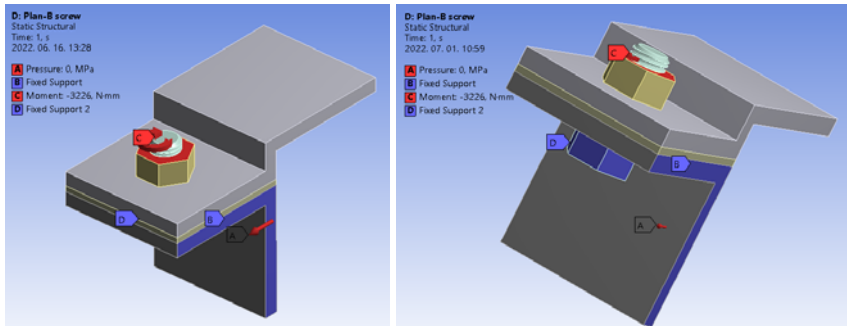


Figure 12 The model, with the boundary conditions

The applied tightening torque was determined based on the literature (Zsáry, 1999), so that the force generated in the screw shaft is the same as the preload applied in previous cases. When setting the contacts, we followed the instructions in (Sarka, 2022). The simulation results are shown in Figure 16.

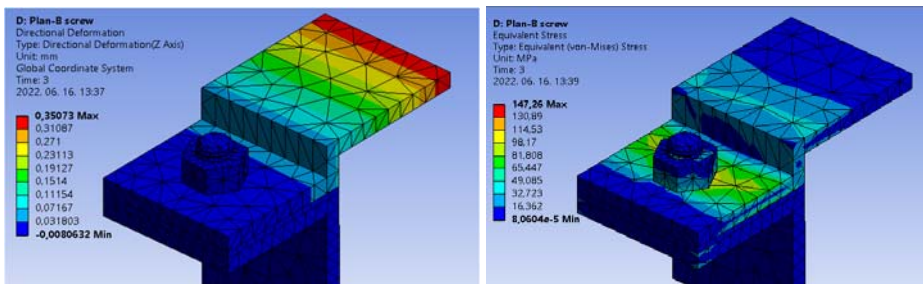


Figure 13 A tension bolt connection simulated using the real bolt geometry. Displacements and stresses

The results obtained from the simulation are close to the results of previous versions. The running time, on the other hand, has increased drastically to a duration of 631 seconds. Figure 17 shows the gasket conditions in relation to the gap and the contact pressure.

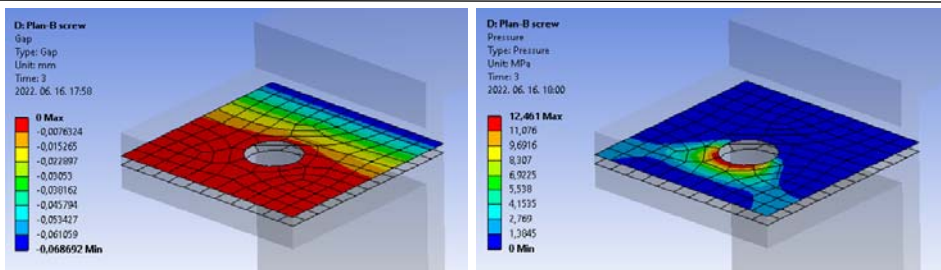


Figure 14 The results of the ‘Contact-tool’ for a screw made with a real thread

In terms of contact, similar values are obtained as with the application of "Bolt-pretension".

6. SUMMARY

The results of the four different cases are presented in tabular form so that they can be better compared with each other. From the four simulations carried out, it can be concluded that there are significant differences between the results of the individual models. If we want to carry out preliminary simulations to help planning, ‘Beam’ is used due to its suitable and very fast running, although the results are not very accurate, but fortunately the deviation points in the direction of safety.

Table 1
Summary of run results. The highest value is bold marked

	Def. [mm]	Stress [MPa]	Gap [mm]	pcont [MPa]	Time [sec]	Elements [pcs]	Nods [pcs]
Without pretension	0,41	130,24	-0,08	8,89	4	1638	4935
With pretension	0,35	130,30	-0,06	11,50	240	1638	4935
Beam tool + pretension	0,36	156,54	-0,06	16,86	4	1239	3547
Real screw model	0,36	147,26	-0,07	12,46	631	10010	19108

If we want to get a more accurate picture of the bolt connection, then either the ‘Bolt-pretension’ or the real bolt model must be used. Of these, the ‘bolt tool’ should be used if we do not want/need to take into account the screw torque from the tightening torque. In all other cases, ‘real bolt model’ is the right choice.

We plan to compare the revealed results with real experiments and publish them in the future, so that the settings of the finite element method can be even closer to reality.

ACKNOWLEDGEMENT

In this way, I would like to thank Attila Potyka departmental engineer and Zsolt Tóbis master's teacher for the help with preparing the article. They took my work forward with their constructive criticism.

REFERENCES

Alfattani, R. (2020). Modeling and Simulating the Static Structural Response and Lift Off of a Preloaded Bolted Joint on a Flange Vol63,. *Proceedings of The 14th International Conference on Interdisciplinarity in Engineering*. Târgu Mureş, Romania: MDPI. doi:<https://doi.org/10.3390/proceedings2020063010>

Bocko, J., Lengvarský, P., & Huňady, R. (2020). Possibilities of modelling the bolts in program ANSYS. *IOP Conf. Series: Materials Science and Engineering*. IOP Publishing. doi:<https://doi.org/10.1088/1757-899X/776/1/012021>

Lovas, L. (2018). Csavarkötés modellezésének kérdései. *GÉP*, 69(4), 59-62.

Lovas, L. (2020). Haszonjármű kerékcsavar lazulásának kérdései. *GÉP*, 71(7-8), 43-46.

Sarka, F. (2022). Examination of Bolt Connection with Finite Element Method. In K. Jármái, & Á. Cservenák (Ed.), *Springer Cham., Vehicle and Automotive Engineering 4*, pp. 212-222. doi:https://doi.org/10.1007/978-3-031-15211-5_19

Zsáry, Á. (1999). *Gépelemek* (Vol. 1). Budapest: Nemzeti Tankönyvkiadó.

POSSIBILITY OF USE OF ARTIFICIAL INTELLIGENCE IN THE WHOLE CLAIM SETTLEMENT PROCESS ON INSURANCE COMPANIES' VEHICLE CLAIMS

VIKTOR SESZTAKOV

*Budapest University of Technology and Economics,
Department of Automotive Technologies
1111 Budapest, Stoczek str. 6. J. building V. floor
viktor.sesztakov@gmail.com*

Abstract: The paper introduces the possibility of use of Artificial Intelligence in the whole claim settlement process on insurance companies' vehicle claims. A fully automated vehicle claim settlement needs to develop the automatic liability check of the accident, which is now only made by human experts. The main points of this article are the main directions of the possible future development, such as to recognize the traffic situation, and to make a proper accident reconstruction.

Keywords: *Artificial Intelligence, AI, methodology, vehicle claims, insurtech*

1. INTRODUCTION

It is possible to use artificial intelligence to handle the whole claim settlement process on insurance companies' vehicle claims. The claim settlement is made up of three main steps:

1. check if the insurance is covered by fee at the date of the accident.
2. calculate the real cost of the vehicle claim.
3. check if the insured person is liable for the accident.

The fee coverage check has been automatism for decades. The vehicle damage recognition can now be made automatically also with the use of artificial intelligence, based on photographs, and the result of the whole process is the real value of the claim cost. We can see a very good solution from Solera, called Qapter Intelligent Estimating, or Visual Intelligence. This is done by image processing and deep-learning algorithms. The image classification uses a multi-model approach, where a machine learning model is trained to identify most of the vehicle's

outer parts and identify and classify different types of damages in photos taken of vehicles. This kind of technology is now publicly available, and a large dataset has been used to train the model to a high accuracy. The vehicle claim cost is not an estimation, but a real value, because it is calculated in the Audatex/Qapter program, which uses car manufacturers' data. Furthermore, Qapter Intelligent Triage is an early warning system in the claim settlement process, in the event that the damage causes total loss of the vehicle.

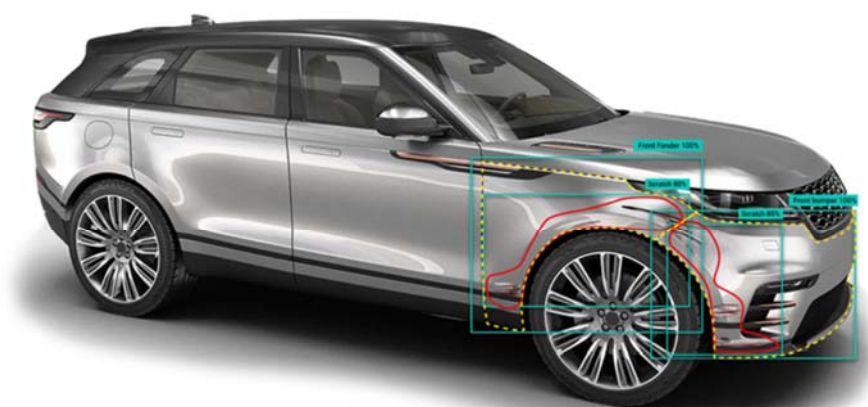


Figure 1 AI identified parts and damages

The next step to a fully automated vehicle claim settlement could be to develop the automatic liability check of the accident, which is now only made by human experts, but can also be done with the use of Artificial Intelligence.

A further aim of the computer-based analysis and evaluation of the accidents could also lead to improved road safety (Takacs, 2023).

Artificial Intelligence (AI) is a branch of computer science that aims to create machines and systems that can perform tasks that would typically require human intelligence, such as recognizing speech, making decisions, and solving problems. The theoretical background of AI is based on several fields of study, including:

- Cognitive psychology: This field studies human mental processes such as perception, memory, and problem-solving. AI researchers use principles from cognitive psychology to design intelligent systems that can mimic human thought processes (Matijošius, 2022).
- Logic: AI systems often use logic to represent and reason about knowledge. Researchers in the field of logic, specifically in the area of

automated reasoning, have developed techniques for representing and manipulating knowledge using formal languages such as first-order logic.

- Computer science: The field of AI heavily relies on computer science to develop efficient algorithms and architectures for implementing intelligent systems. Techniques from areas such as machine learning, natural language processing, and computer vision are used to create AI systems that can learn from data, understand human language, and perceive the world.
- Philosophy: The field of AI raises many philosophical questions about the nature of intelligence, consciousness, and the relationship between machines and humans. The study of philosophy of mind and metaphysics is important for understanding the goals and limitations of AI research.
- Neuroscience: AI researchers also draw inspiration from neuroscience to understand the neural mechanisms underlying human intelligence. The study of neural networks and the brain's structure and function can inform the design of AI systems that can adapt and learn like humans.

All these fields work together to create the theoretical background of AI, which allows the development of intelligent systems that can perform tasks that would typically require human intelligence.

Nowadays, artificial intelligence is increasingly used to evaluate images. One of the most well-known areas is medical imaging. CT scans can be evaluated by both human radiologists and artificial intelligence (AI) systems. Human radiologists have the advantage of being able to use their experience and intuition when interpreting CT scans, while AI systems can quickly analyse large amounts of data and can be programmed to recognize specific patterns or abnormalities. Both human radiologists and AI systems can make mistakes, but research has shown that the combination of human and AI evaluations can lead to more accurate and efficient diagnoses. These methods are used for the implant design also (Györi & Ficzere, 2016), (Ficzere, 2018), (Ficzere, 2022).

2. METHODOLOGY

Determination of accident liability for road vehicles based on photographs using artificial intelligence, a few steps need to be followed:

1. Data collection:

A large dataset of images of vehicles with different types of

- damages such as dents, scratches, and broken parts need to be collected.

- accidents. The dataset should also include information about the accident type, such as frontal accident, overtaking, hitting a pedestrian, crossroad accident, ...
- This dataset of images of vehicles should also contain a so-called ‘EES catalogue’. EES means Energy Equivalent Speed, which is the speed of a car hitting a rigid wall. This type of catalogue has a large dataset of crash tests made under controlled conditions, and each car in the photo has specific deformation energy. So, the later calculations will have exact comparative data.



Figure 2 Crash test made by Euro NCAP

- The weather conditions by places and by timeline (web solutions available).
- The environmental conditions (e.g., adhesion coefficient) by the type of each weather condition for each road type (e.g., concrete, asphalt...).
- Images of sketches or drawings of the accident. The person involved in the accident (drivers, and witnesses also) draw the traffic situation of the accident, for the request of the insurance company.
- A large dataset of written reports of the parties involved in the accident.
- The severity of the injury of the person involved in the accident.
- Dataset of the accident sites with GPS coordinates, maps, and if available, with photos of the place, such as satellite- or aerial photos, and photos or videos from the viewpoints of the parties involved. The onboard videos can be good data as well.

The place of the accident and the type of accident can be gathered from a great post-accident cloud-based mobile app, called 'e-Kárbejelentő', which is a great solution to the first notice of loss. This solution was made by the Association of Hungarian Insurance Companies.



Figure 3 Post-accident cloud-based mobile app, called 'e-Kárbejelentő'

Thanks to the use of this app, we now have a map of the most dangerous places in Hungary, which can be used by authorities also to avoid further accidents.

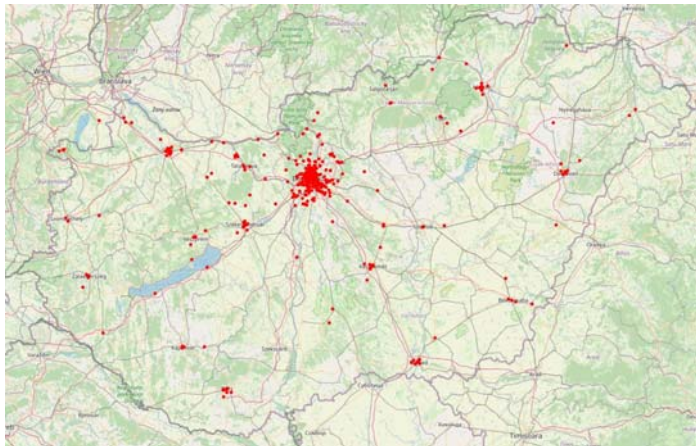


Figure 4 The most dangerous transport places in Hungary

2. Image classification: A machine learning model, such as a convolutional neural network (CNN), is trained on the dataset to identify and classify different types of accidents.
3. Image segmentation: The CNN model can be further fine-tuned for image segmentation to prepare a detailed accident analysis to calculate the different pre-accident vehicle speeds, and to calculate the pre-accident reaction points.

3. SUMMARY

In summary, the use of artificial intelligence (AI) to calculate the claim cost of road vehicles based on photographs is already a public application of AI. The liability check and accident reconstruction could be also automated with the use of AI. This can be done using techniques such as image classification and image segmentation, which are powered by machine learning models such as convolutional neural networks (CNNs). However, this technology is still in its early stages and requires a large dataset to train the model accurately. The theoretical background of AI is based on several fields of study, including cognitive psychology, logic, computer science, philosophy, and neuroscience. These fields work together to create intelligent systems that can perform tasks that would typically require human intelligence.

REFERENCES

- Ficzere, P. (2018). Design Questions of the Individual Medical Implants., *Proceedings of the 4th International Interdisciplinary 3D Conference Engineering*, pp. 57-67. Pécs.
- Ficzere, P. (2022). Research on and Practice of Additive Manufacturing Technologies. *Hungarian Journal of Industry and Chemistry*, 49(2), 59-64. doi:<https://doi.org/10.33927/hjic-2021-23>
- Györi, M., & Ficzere, P. (2016). Increasing Role of Sections Caused by 3D Modelling. *Periodica Polytechnica Transportation Engineering*, 44(3), 164-171. doi:<https://doi.org/10.3311/PPtr.9053>
- Matijošius, J. (2022). Cognitive evolution of transport spatiality. *Cognitive Sustainability*, 1(3). doi:<https://doi.org/10.55343/cogsust.32>

Seregi, B. L., & Ficzer, P. (2022). Weight Reduction of a Drone Using Generative Design. *Hungarian Journal of Industry and Chemistry*, 49(2), 19-22. doi:<https://doi.org/10.33927/hjic-2021-16>

Takacs, A. (2023). Safe In and Out of the Car. *Vehicle and Automotive Engineering 4 Lecture Notes in Mechanical Engineering*. Miskolc: Springer, Cham. doi:https://doi.org/10.1007/978-3-031-15211-5_6

SOURCE OF FIGURES

[F1] <https://www.qapter.com/technology/> (last open: 29. April 2023)

[F2] <https://www.euroncap.com/en/results/vw/touran/47768> (last open: 29. April 2023)

[F3] <https://mabisz.hu/> (last open: 29. April 2023)

[F4] <https://mabisz.hu/> (last open: 29. April 2023)

DETERMINATION OF TOOTH SURFACE POINTS ON BEVEL GEARS FOR CHECKING ON A COORDINATE MEASURING MACHINE

MIKLÓS VÁRKULI¹ - GABRIELLA BOGNÁR² - JÓZSEF SZENTE

University of Miskolc, Institute of Machine and Product Design,

H-3515 Miskolc-Egyetemváros,

¹miklos.varkuli@uni-miskolc.hu, ²v.bognar.gabriella@uni-miskolc.hu

¹<https://orcid.org/0000-0003-4435-7629>, ²<https://orcid.org/0000-0002-4070-1376>

Abstract: The use of coordinate measuring machines is an integral part of gear design. In order to this tool to be truly effective, it is necessary to know the surfaces to be measured and to provide comparative values. In the study, the mathematical modelling of the bevel gear tooth surfaces and the exact description of the production are used to produce the theoretical surfaces on which points can be added in any desired arrangement and number. These points form the basis for the evaluation of the measurement by comparison with the measured values.

Keywords: *coordinate measuring machine, bevel gear, mathematical modelling, grid points*

1. INTRODUCTION

Measurements on coordinate measuring machines (CMM), which can be used to check the accuracy of tooth surfaces, are essential tools for the development of gear drive pairs.

In order to evaluate the measurement results, reference values are needed, as an ideal solution, knowledge of the theoretically accurate tooth surfaces. We can produce these by mathematical modelling of production processes. As a result of the mathematical modelling, we have the position vector and the normal vector of the tooth surface in a coordinate system defined by us. During CMM measurements, the tooth surface is checked as a set of points. For this, the theoretical tooth surface is specified with a finite number of point sets. The points form a surface mesh (grid). The question may arise, how many points do we need? In practice, 45 points are used for CMM measurement of gears. At the same time, with the

method presented here, knowing the theoretical tooth surfaces, the points used for inspection can be produced in any desired number and arrangement.

In the study, we focus on bevel gears with curved teeth, but the procedure presented for mathematical modelling can be applied to any gear, or with proper interpretation, it applies to any component.

2. LOCATION OF THE GRID POINTS ON TOOTH SURFACE

The ANSI/AGMA 2009-B01 standard (American Gear Manufacturers Association, 2009) recommends the solution shown in Figure 1 for the placement of the point grid used for CMM measurement of bevel gears.

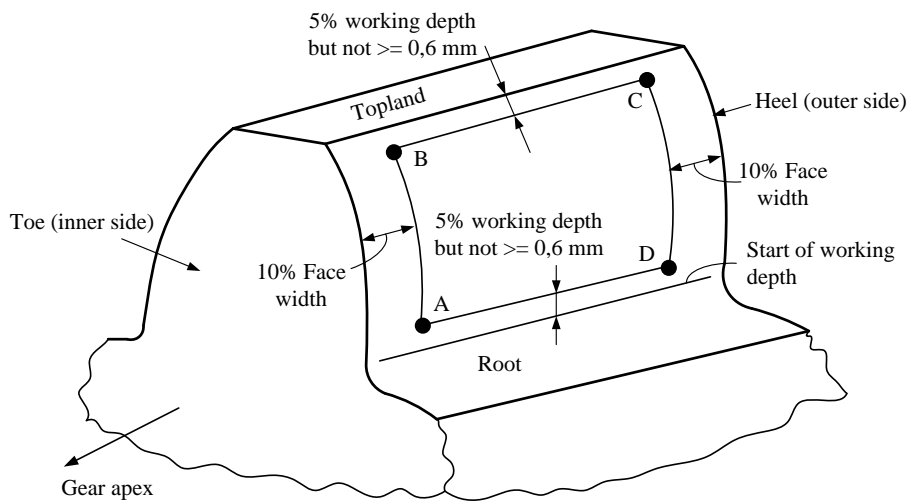


Figure 1 Placement of mesh points on the tooth surface

Within the marked area, the points form a ‘matrix’ consisting of 5 rows and 9 columns according to Figure 2. If we want to describe the complete tooth surface, e.g., for finite element analysis, then the points will be recorded on the tooth ends and face cones.

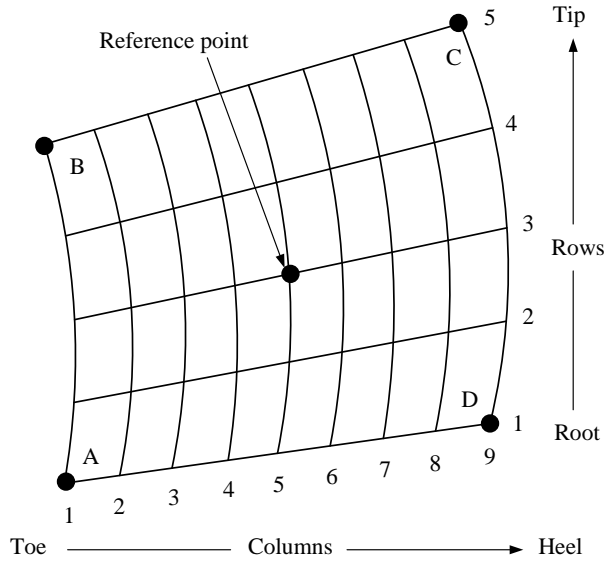


Figure 2 Arrangement of grid points into rows and columns

3. DEFINING THE COORDINATES OF THE GRID POINTS

During the present calculations, the point mesh is extended to the useful tooth surface, according to Figure 3.

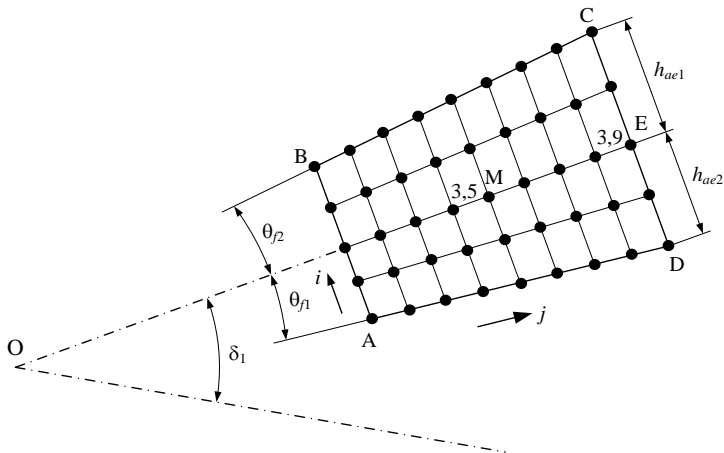


Figure 3 Placement of grid points on the tooth surface of the smaller bevel gear

The points forming the surface mesh will be entered in a polar coordinate system. The origin of the coordinate system is the vertex O of the pitch cone of the bevel wheel. Reference point M (3,5) is the point on the pitch cone, belonging to the mean cone distance, whose radial coordinate is $R_{3,5} = R_m \sin \delta_1$, and its axial coordinate is $L_{3,5} = R_m \cos \delta_1$. The distance OE is the outer cone distance R_e . In Figure 3, h_{ae1} and h_{ae2} are the addendums of the gear pair, θ_{f1} and θ_{f2} are the dedendum angles, δ_1 is the pitch angle of the bevel gear.

The coordinates of the boundary points are as follows:

$$\begin{aligned} R_C &= R_e \sin \delta_1 + h_{ae1} \cos \delta_1, \\ L_C &= R_e \cos \delta_1 - h_{ae1} \sin \delta_1. \end{aligned} \quad (1)$$

$$\begin{aligned} R_D &= R_e \sin \delta_1 - h_{ae2} \cos \delta_1, \\ L_D &= R_e \cos \delta_1 + h_{ae2} \sin \delta_1. \end{aligned} \quad (2)$$

$$\begin{aligned} R_A &= R_D + b(\tan \theta_{f1} \cos \delta_1 - \sin \delta_1), \\ L_A &= L_D - b(\tan \theta_{f1} \sin \delta_1 + \cos \delta_1). \end{aligned} \quad (3)$$

$$\begin{aligned} R_B &= R_C - b(\tan \theta_{f2} \cos \delta_1 + \sin \delta_1), \\ L_B &= L_C + b(\tan \theta_{f2} \sin \delta_1 - \cos \delta_1). \end{aligned} \quad (4)$$

The coordinates of the grid points can be calculated as follows:

$$R_{i,j} = R_A + (i-1)\Delta r_i + \frac{j-1}{8} [R_D - R_A + (i-1)(\Delta r_e - \Delta r_i)] \quad (5)$$

$$L_{i,j} = L_A - (i-1)\Delta l_i + \frac{j-1}{8} [L_D - L_A - (i-1)(\Delta l_e - \Delta l_i)] \quad (6)$$

here

$$\Delta r_i = \frac{R_B - R_A}{4}, \quad \Delta r_e = \frac{R_C - R_D}{4}, \quad (7)$$

furthermore

$$\Delta l_i = \frac{L_A - L_B}{4}, \quad \Delta l_e = \frac{L_D - L_C}{4}. \quad (8)$$

To identify the points, $i = 1 \dots 5$, $j = 1 \dots 9$.

4. MATHEMATICAL MODEL OF TOOTH SURFACE

The mathematical modelling of gear tooth surfaces was based on the works of Litvin (Litvin, 1989), (Litvin, 1994), (Litvin & Fuentes, 2004). For the mathematical modelling of the tooth surfaces of the bevel gear, the following data or preliminary calculations are required:

- geometrical data of the bevel gear.
- cutter dimensions: cutter radius, blade angle, the relative position of the blades working on the two tooth sides.
- machine setting data: the relative position of the tool and the workpiece on the machine tool.
- movement conditions: the coordinated movement of the tool and the workpiece during production.

When manufacturing Gleason-type spiral bevel gears, chipping results from the rotating movement of the cutter head. This movement is independent of other motions that determine the shape of the tooth surface. During rotation, the cutting edges of the tool produce a surface of rotation, which is called generating surface. The position vector of the generating surface can be described with two parameters:

$$\mathbf{r}_c(s, \theta) \quad (9)$$

The generating surface results in a family of surfaces in the relative movement. Which has the following form in the coordinate system fixed to the workpiece, with its origin located at the apex of the pitch cone:

$$\mathbf{r}(s, \theta, \psi) = \mathbf{M}(\psi)\mathbf{r}_c(s, \theta) \quad (10)$$

Here, \mathbf{M} is the matrix of the transformation, ψ is the motion parameter.

To produce the tooth surface, we need to find a relationship between the 3 parameters of the family of surfaces. One possible way to do this is to obtain partial derivatives and solve the following equation:

$$\left(\frac{\partial \mathbf{r}}{\partial s} \times \frac{\partial \mathbf{r}}{\partial \theta} \right) \cdot \frac{\partial \mathbf{r}}{\partial \psi} = f(s, \theta, \psi) = 0 \quad (11)$$

Here, the first term in brackets on the left side is the normal at the instantaneous point of contact, the second term is the quantity proportional to the relative velocity at the same point. (11) is the equation of meshing.

Using the parameter relation generated from the solution of equation (11), the equation of the tooth surface of bevel gear is available in the following form:

$$\mathbf{r}(\theta, \psi) = \mathbf{r}(s(\theta, \psi), \theta, \psi) \quad (12)$$

5. COORDINATES OF THE TOOTH SURFACE IN THE GRID POINTS

(12) position vector given with the coordinates is the following:

$$\mathbf{r}(\theta, \psi) = \begin{bmatrix} x(\theta, \psi) \\ y(\theta, \psi) \\ z(\theta, \psi) \end{bmatrix} \quad (13)$$

The location of any point on the tooth surface can be determined by solving the following system of non-linear equations.

$$\begin{aligned} [x(\theta, \psi)]^2 + [y(\theta, \psi)]^2 &= R^2, \\ z(\theta, \psi) &= L. \end{aligned} \quad (14)$$

Here, R is the distance of the point from the axis, and L is the distance of the point from the origin, along the axis.

The parameters θ and ψ are available as a solution to equation system (14), so the coordinates of the point on the tooth surface can be determined.

Now substitute the coordinates of the grid points according to (5) and (6) into equations (14).

$$\begin{aligned} [x(\theta, \psi)]^2 + [y(\theta, \psi)]^2 &= R_{i,j}^2, \\ z(\theta, \psi) &= L_{i,j}. \end{aligned} \quad (15)$$

Applying equations (15) to all grid points, as a result of $i = 1 \dots 5$, $j = 1 \dots 9$, we have to solve 45 system of equations, which results in 45 θ and 45 ψ values. By substituting $\theta_{i,j}$ and $\psi_{i,j}$, the coordinates of the grid points on the tooth surface are as follows:

$$x_{i,j}(\theta_{i,j}, \psi_{i,j}), \quad y_{i,j}(\theta_{i,j}, \psi_{i,j}), \quad z_{i,j}(\theta_{i,j}, \psi_{i,j}) = L_{i,j}. \quad (16)$$

6. APPLICATION EXAMPLE

For the practical application of the presented method, we worked out a numerical example. The investigated gear is a spiral bevel gear having circular arc profile along tooth length, whose geometrical data is given in Table 1.

Table 1
Dimensions of investigated bevel gear

Designation	Notation	Data
Number of teeth	N	30
Outer transverse module, mm	m_{te}	4,791
Face width, mm	b	40
Pressure angle, °	α_n	20
Mean spiral angle, °	β_m	30
Outer cone distance, mm	R_e	235,01
Mean cone distance, mm	R_m	215,01
Pitch diameter, mm	d_{ae}	143,73
Outer addendum, mm	h_{ae}	3,69
Outer dedendum, mm	h_{fe}	5,16
Cutter radius, mm	r_c	114,3
Cutter point width, mm	P_w	2,286
Pitch angle, °	δ	17,8
Face angle, °	δ_a	17,9667
Root angle, °	δ_r	17,6333
Dedendum angle, °	θ_f	0,1667
Hand of spiral		left

Additional data not included in the table, but necessary for the calculations, were determined based on (American Gear Manufacturers Association, 2006). Table 2 and Table 3 summarize the coordinates of the grid points determined by the method presented in Chapter 3.

Table 2
Radial coordinates of grid points

R	1	2	3	4	5	6	7	8	9
1	55.897	57.412	58.926	60.441	61.955	63.47	64.985	66.499	68.014
2	57.677	59.198	60.720	62.241	63.763	65.284	66.806	68.328	69.849
3	59.457	60.985	62.513	64.042	65.570	67.099	68.627	70.156	71.684
4	61.236	62.772	64.307	65.843	67.378	68.913	70.449	71.984	73.520
5	63.016	64.559	66.101	67.643	69.186	70.728	72.270	73.812	75.355

To solve the system of equations (15), we created a program based on mathematical software. Table 4 and Table 5 contain the x and y coordinates of the mesh points on the tooth surface. The z coordinate is the same as the L coordinate of the grid points.

Table 3
Axial coordinates of grid points

L	1	2	3	4	5	6	7	8	9
1	186.868	191.633	196.398	201.163	205.928	210.694	215.459	220.224	224.989
2	186.297	191.06	195.822	200.585	205.348	210.111	214.874	219.637	224.4
3	185.725	190.486	195.246	200.007	204.768	209.528	214.289	219.05	223.81
4	185.154	189.912	194.671	199.429	204.187	208.946	213.704	218.463	223.221
5	184.582	189.339	194.095	198.851	203.607	208.363	213.12	217.876	222.632

Table 4
x coordinates of surface grid points

x	1	2	3	4	5	6	7	8	9
1	54.90	56.73	58.53	60.27	61.92	63.46	64.86	66.08	67.07
2	56.57	58.43	60.26	62.02	63.71	65.28	66.71	67.96	68.98
3	58.19	60.09	61.95	63.76	65.48	67.10	68.57	69.86	70.92
4	59.76	61.70	63.61	65.46	67.24	68.90	70.42	71.76	72.87
5	61.28	63.27	65.23	67.14	68.97	70.69	72.26	73.66	74.83

Table 5
y coordinates of surface grid points

y	1	2	3	4	5	6	7	8	9
1	10.52	8.808	6.827	4.567	2.017	-0.835	-4	-7.488	-11.31
2	11.24	9.496	7.484	5.187	2.595	-0.304	-3.522	-7.068	-10.95
3	12.21	10.43	8.375	6.031	3.386	0.4303	-2.849	-6.463	-10.42
4	13.36	11.55	9.444	7.049	4.349	1.331	-2.014	-5.699	-9.734
5	14.68	12.82	10.67	8.22	5.461	2.381	-1.034	-4.793	-8.908

7. SUMMARY

To determine the theoretical tooth surfaces of bevel gears, we created a mathematical model describing the production. Mathematical modelling of tooth surfaces is done by specifying discrete points for practice. The surface can be meshed with any number of points. In practice, the use of 45 points for checking on coordinate measuring machines is widespread. In the grid points, the known coordinates of the theoretical tooth surface can be combined with the measured values to evaluate and classify the accuracy.

For the practical application of the method, we developed a numerical example using the data of a bevel gear with curved teeth. We selected the mesh points and determined their coordinates, then produced the coordinates of the theoretical tooth surface at the given points. These coordinates will be the reference values during the measurement on the coordinate measuring machine.

REFERENCES

American Gear Manufacturers Association. (2006). ANSI/AGMA 2005-D03: Design Manual for Bevel Gears. American Gear Manufacturers Association.

American Gear Manufacturers Association. (2009). ANSI/AGMA 2009-B01. *Bevel Gear Classification, Tolerances, and Measuring Methods*. American Gear Manufacturers Association.

Litvin, F. L. (1989). *Theory of Gearing*. NASA RP 1212. NASA.

Litvin, F. L. (1994). *Gear Geometry and Applied Theory*. Prentice Hall.

Litvin, F. L., & Fuentes, A. (2004). *Gear Geometry and Applied Theory* (Second Edition ed.). Cambridge University Press.